

**THE RECONSTRUCTION OF LARGE  
THREE-DIMENSIONAL MESHES**

by

Matthew Grant Bolitho

A dissertation submitted to The Johns Hopkins University in conformity with  
the requirements for the degree of Doctor of Philosophy.

Baltimore, Maryland

March, 2010

© Matthew Grant Bolitho 2010

All rights reserved

# Abstract

Surface reconstruction is the process of creating virtual three-dimensional representations of real-world objects using data obtained from 3D scanners.

The traditional challenges of surface reconstruction arise from the uncertain nature of input data. Inaccuracies in scanning devices create noisy data. Point sampling is often non-uniform. And, accessibility constraints during the scanning process may leave some regions of the surface devoid of data. Robustly constructing a surface in the presence of these data anomalies is a difficult problem. In addition, surface reconstruction methods have recently encountered a new challenge resulting from developments in 3D scanning techniques. New scanning technologies have driven a dramatic increase in the size of datasets available for surface reconstruction, with datasets now exceeding one billion point samples. As a result, space and time efficiency have become critical in the development of effective reconstruction algorithms, and the design of streaming and parallel techniques has become indispensable.

In this dissertation we describe a new technique for surface reconstruction,

## ABSTRACT

based on the solution to a Poisson equation. Our approach is designed to meet the multiple challenges of modern datasets. The method is robust to the types of noise found in real-world data, allowing the reconstruction of high quality surfaces. Despite formulating surface reconstruction as a global problem, we also show that our method can be implemented using only local updates which allows extremely large reconstruction problems to be solved in a streaming manner. We also exploit current industry trends towards multi-core and parallel computing by presenting a parallel implementation of our method that is able to dramatically reduce the time taken to produce highly detailed reconstructions. We demonstrate the practicality of our method on several of the largest reconstruction datasets available to date.

Primary Reader: Dr. Michael Kazhdan

Secondary Readers: Dr. Randal Burns and Dr. Szymon Rusinkiewicz

# Acknowledgements

# Dedication

# Contents

<b>Abstract</b>	<b>ii</b>
<b>Acknowledgements</b>	<b>iv</b>
<b>List of Tables</b>	<b>xii</b>
<b>List of Figures</b>	<b>xiv</b>
<b>1 Introduction</b>	<b>1</b>
1.1 3D Scanning . . . . .	2
1.2 Surface Reconstruction . . . . .	5
1.3 Outline of Dissertation . . . . .	10
<b>2 Surface Reconstruction</b>	<b>11</b>
2.1 Discrete Methods . . . . .	14
2.1.1 Computational Geometry . . . . .	14
2.1.2 Alpha Shapes . . . . .	14

## CONTENTS

2.1.3	Power Crust . . . . .	15
2.1.4	Ball Pivoting . . . . .	16
2.2	Continuous Methods . . . . .	17
2.2.1	Surface Fitting . . . . .	17
2.2.1.1	Balloon Fitting . . . . .	17
2.2.1.2	Fast Level Set Method . . . . .	18
2.2.1.3	Point Set Surfaces . . . . .	18
2.2.2	Implicit Function Fitting . . . . .	19
2.2.3	Local Function Fitting . . . . .	20
2.2.3.1	Hoppe <i>et al.</i> . . . . .	20
2.2.3.2	Volumetric Range Image Processing (VRIP) . . . . .	21
2.2.3.3	Multi-level Partitions of Unity (MPU) . . . . .	22
2.2.4	Global Function Fitting . . . . .	23
2.2.4.1	Blobby Models . . . . .	23
2.2.4.2	Fast RBF . . . . .	24
2.2.4.3	Fast Fourier Transform . . . . .	26
2.2.4.4	Wavelets . . . . .	27
2.2.4.5	Our Approach . . . . .	28
<b>3</b>	<b>Poisson Surface Reconstruction</b>	<b>29</b>
3.1	The Poisson Idea . . . . .	29
3.2	Approach . . . . .	32

## CONTENTS

3.2.1	Defining the gradient field . . . . .	33
3.2.2	Approximating the gradient field . . . . .	34
3.2.3	Solving the Poisson problem . . . . .	35
3.3	Implementation . . . . .	36
3.3.1	Problem Discretization . . . . .	37
3.3.1.1	Defining the function space . . . . .	38
3.3.1.2	Selecting a base function . . . . .	39
3.3.2	Vector Field Definition . . . . .	40
3.3.3	Linear System Definition . . . . .	41
3.3.4	Iso-Surface Extraction . . . . .	43
3.3.5	Non-uniform Samples . . . . .	44
3.3.5.1	Estimating local sampling density . . . . .	45
3.3.5.2	Estimating a samples depth . . . . .	47
3.3.5.3	Computing the vector field . . . . .	47
3.3.6	Selecting an iso-value . . . . .	49
3.4	Results . . . . .	49
3.4.1	Resilience to Noise . . . . .	50
3.4.2	Comparison to Previous Work . . . . .	52
3.4.2.1	Comparison to Wavelet-based approach . . . . .	54
3.4.2.2	Comparison to the FFT-based approach . . . . .	56
3.4.2.3	Comparison to VRIP . . . . .	57



## CONTENTS

3.4.2.4	Limitation of our approach . . . . .	58
3.4.3	Performance and Scalability . . . . .	60
<b>4</b>	<b>Streaming Surface Reconstruction</b>	<b>64</b>
4.1	Related Work . . . . .	67
4.1.1	Out-of-core Surface Reconstruction . . . . .	67
4.1.2	Stream Processing . . . . .	68
4.1.3	Other Out-of-core Processing . . . . .	68
4.1.4	Out-of-core Linear Solvers . . . . .	69
4.2	Representation . . . . .	69
4.2.1	Implementation . . . . .	72
4.3	A Simple Streaming Reconstruction . . . . .	74
4.3.1	Pre-processing . . . . .	76
4.3.2	Octree Construction ( $k = 1$ ) . . . . .	77
4.3.3	Vector Field Construction ( $k = 1$ ) . . . . .	77
4.3.4	Divergence Computation ( $k = 2$ ) . . . . .	78
4.3.5	Poisson System Solution ( $k = 2$ ) . . . . .	81
4.3.6	Computing the Iso-Value ( $k = 1$ ) . . . . .	82
4.3.7	Extracting the Iso-Surface ( $k = 2$ ) . . . . .	82
4.4	An Optimized Implementation . . . . .	86
4.4.1	First Pass ( $k = 6$ ) . . . . .	87
4.4.1.1	Buffering Samples . . . . .	88

## CONTENTS

4.4.2	Second Pass ( $k = 8$ ) . . . . .	89
4.4.2.1	Index Dependencies . . . . .	90
4.4.2.2	Depth Dependencies . . . . .	90
4.5	Results . . . . .	91
4.5.1	Large Datasets . . . . .	91
4.5.2	Scalable Memory Use . . . . .	93
4.5.3	Computation Times . . . . .	98
4.5.4	Streaming Solver Accuracy . . . . .	100
4.6	Discussion . . . . .	100
<b>5</b>	<b>Parallel Surface Reconstruction</b>	<b>105</b>
5.1	Related Work . . . . .	107
5.2	Parallel Reconstruction . . . . .	108
5.3	Shared Memory . . . . .	108
5.3.1	Data Partitioning . . . . .	109
5.3.2	Work Distribution . . . . .	110
5.3.3	Data Sharing . . . . .	112
5.3.3.1	Tree Construction . . . . .	115
5.3.3.2	Solving the Laplacian . . . . .	116
5.3.4	Scalability Issues . . . . .	117
5.4	Distributed Memory . . . . .	120
5.4.1	Data Partitioning . . . . .	121

## CONTENTS

5.4.2	Load Balancing . . . . .	123
5.4.3	Replication and Merging of Shared Data . . . . .	123
5.4.4	Tree Construction . . . . .	125
5.4.5	Solving the Laplacian . . . . .	126
5.5	Results . . . . .	127
5.5.1	Correctness . . . . .	128
5.5.2	Skew . . . . .	129
5.5.3	Scalability . . . . .	131
5.5.4	David . . . . .	134
<b>6</b>	<b>Conclusion</b>	<b>137</b>
6.1	Future Work . . . . .	140
6.1.1	A GPU Implementation . . . . .	140
6.1.2	A Surface Reconstruction Benchmark . . . . .	141
	<b>Bibliography</b>	<b>144</b>
	<b>Vita</b>	<b>154</b>

# List of Tables

3.1	The running time (in seconds), the peak memory usage (in megabytes), and the number of triangles in the reconstructed model for the different depth reconstructions of the Dragon model. A kernel depth of 6 was used for density estimation. . . . .	61
3.2	The running time (in seconds), the peak memory usage (in megabytes), and the number of triangles in the reconstructed surface of the Stanford Bunny generated by the different methods. . . . .	63
4.1	Read and write operations when processing block $\mathcal{S}_i^d$ in the various multilevel streaming computations. . . . .	76
4.2	Quantitative results for multilevel streaming reconstructions, showing input points, octree height $D + 1$ , output mesh triangles, total execution time (hours), memory use (MB), and total octree stream size (MB). . . . .	92
4.3	Comparison of the data structure size (MB), peak working set (MB), and running time (hours) for the in-core and streaming reconstruction algorithms over a range of resolutions for the David Head model. Running the in-core algorithm beyond a resolution of 2048 was impossible due to its high memory requirements. . . . .	103
5.1	A summary of the the size of each output model, and the maximum and average vertex distance from the serial output of several different reconstructions of the Bunny dataset at depth 9 created with the distributed implementation. . . . .	127

## LIST OF TABLES

5.2	The running time (in minutes), aggregate disk use (in MB), and peak memory use (in MB) of the shared memory and distributed memory implementations of the Parallel Poisson Surface Reconstruction algorithms for the Lucy dataset at depth 12, with $d_{full} = 6$ and the David dataset at depth 14 with $d_{full} = 8$ , running on one through twelve processors. It was not possible to run the shared memory implementation on more than eight processors. . . . .	131
-----	---	-----

# List of Figures

1.1	Four examples of reconstructed objects from different disciplines. . . . .	3
1.2	An example of the reconstruction of the “Bunny” model. Individual scans of the real object are first aligned and combined before a <i>surface reconstruction</i> algorithm produces the final model. . . . .	5
1.3	Illustrative examples of the different types of data anomalies present in three-dimensional scan data: a) noise, b) anisotropy, c) misalignment, d) non-uniformity, and e) missing data. . . . .	6
1.4	Two examples showing how multiple types of anomalies combine in real-world data. . . . .	9
2.1	A taxonomy of surface reconstruction methods, based on the general approach to solving the reconstruction problem. . . . .	13
2.2	A categorization of surface reconstruction methods, based on the type of input data required. . . . .	13
3.1	Intuitive illustration of Poisson reconstruction in 2D. . . . .	30
3.2	Points from scans of the “Armadillo Man” model (left), our Poisson surface reconstruction (right), and a visualization of the indicator function (middle) along a plane through the 3D volume. . . . .	36
3.3	A comparison of the reconstruction of a highly non-uniform dataset using a low resolution (b), high resolution (c) and adaptive resolution sample density estimation (d). . . . .	46
3.4	Reconstructions of an 200,000 point sampling of the “Armadillo Man” model at depth 9 with varying amounts of random noise introduced to the position ( $\delta$ ) and normal ( $\theta$ ) component to the samples. $r$ is the radius of the models bounding sphere. . . . .	51
3.5	Reconstructions of the Stanford Bunny using Power Crust (a), Robust Cocone (b), Fast RBF (c), MPU (d), Hoppe <i>et al.</i> ’s reconstruction (e), Wavelet-based reconstruction (f), FFT-based reconstruction (g), VRIP (h), and our Poisson reconstruction (i). . . . .	53

## LIST OF FIGURES

3.6	Several views of the reconstruction of the Stanford Bunny model using the Wavelet technique (using the D4 basis function) and our method . . . . .	55
3.7	Reconstruction of samples from the region around the left eye of the David model (a), using the fixed-resolution FFT approach (b), and Poisson reconstruction (c). . . . .	56
3.8	Reconstructions of a fragment of the Forma Urbis Romae tablet using VRIP (left) and the Poisson solution (right). . . . .	58
3.9	Reconstructions of the “Happy Buddha” model using VRIP (left) and Poisson reconstruction (right). Although our method generates a more accurate reconstruction of the sharp features, its independence of acquisition modality makes it incapable of leveraging line-of-sight information to carve out the space between the legs. . . . .	59
3.10	Reconstructions of the Dragon model at octree depths 6 (left), 8 (middle), and 10 (right). . . . .	60
3.11	Several images of the reconstruction of the head of Michelangelo’s David, obtained running our algorithm with a maximum tree depth of 11. The ability to reconstruct the head at such a high resolution allows us to make out the fine features in the model such as the inset iris, the drill marks in the hair, the chip on the eyelid, and the creases around the nose and mouth. . . . .	62
4.1	Example of curve reconstruction in 2D as a sequence of three multilevel streaming passes over an adaptive quadtree. . . . .	65
4.2	Illustration of the multilevel stream structure (top rows) and the corresponding quadtree nodes (bottom rows) at two moments in time ( $i = 3, 4$ ). In-core blocks and nodes are highlighted. . . . .	70
4.3	Construction of the out of core octree as points $S_i$ are added to the tree. To process these points, the sub-tree that can be modified by the processing of points $S_i$ is maintained in core (highlighted in grey and diamond hatching). After the points in $S_i$ have been processed, the nodes that cannot be affected by the processing of points in $S_{i+1}$ (grey) are written out to the streams. . . . .	74
4.4	Sequence of streaming passes and flow of the out-of-core octree data, as described in the naive implementation of Section 4.3. . . . .	75
4.5	Comparing the results of the in-core algorithm (left; depth 11; 4,442 MB peak memory) and streaming algorithm (right; depth 13; 780 MB peak memory). . . . .	92
4.6	Views of our reconstruction of the head of Michelangelo’s David. Maximum tree depth was 13, with a target of 2 samples per node. . . . .	94

## LIST OF FIGURES

4.7	Views of our reconstruction of Michelangelo’s Awakening statue. The maximum tree depth was 14 with a target of 2 samples per node. . . . .	95
4.8	The peak working set in our 3 multilevel streaming passes, and in the in-core algorithm (far left), for a range of reconstructions of the head of Michelangelo’s David. . . . .	96
4.9	Memory use over time for a depth 12 reconstruction of the “Lucy” statue using two different poses of the model. . . . .	97
4.10	The cumulative distribution of geometric error for a depth 12 reconstruction of the “Lucy” statue when compared to the in-core algorithm of Chapter 3. . . . .	99
4.11	Comparison of reconstructing the indicator function of a cow silhouette from its Laplacian using a single-resolution streaming solver (a), a traditional conjugate-gradient solver (b), and a cascadic multigrid solver using multilevel streaming (c). . . . .	104
5.1	An illustration of the way data partitions are formed from the tree using the shared memory approach. Each slice of nodes at each depth in the tree is partitioned into a regular grid. Data partitions contain approximately the same amount of the curve (by length) and are shaded according to which processor they are allocated to. Each allocation forms a contiguous block in Morton (Z-curve) order.	109
5.2	The speedup of the shared memory parallel approach for the “Lucy” dataset at depth 12 running on one through eight processors. The spatial locking and lock-free methods are compared. The distributed method from section 5.4 is included for later comparison. . . . .	118
5.3	An illustration of the way data partitions are formed from the tree with $p = 4$ processors. All nodes in $\mathcal{O}^0$ , $\mathcal{O}^1$ and $\mathcal{O}^2$ are shared among all processors and form the data partition $\mathcal{O}^{full}$ . The nodes in remaining depths are split into spatial regions defined by the x-coordinates $\{x_0, x_1, x_2, x_3, x_4\}$ forming the partitions $\mathcal{O}_i^d$ . Note that the finer level partitions do not have to be equal in size, but do need to be allocated on the granularity of the width of nodes at depth $d = d_{full}$ . . . . .	122
5.4	The distribution of error across the $p = 8$ model, when compared to the serial model. The color is used to show $\delta$ values over the surface with $\delta = 0.0$ colored blue and $\delta = 1.0$ colored red. The scale is non-linear to highlight small values of $\delta$ . . . . .	128



## LIST OF FIGURES

5.5	The absolute value of the difference between the work allocated to the processor with most work and the average, expressed as a function of the height of the full resolution tree ( $d_{full}$ ) and the number of processors. . . . .	130
5.6	The speedup of the distributed implementation for the Lucy dataset at depth 12 and the David dataset at depth 14 running on one through twelve processors. The shared memory approach from Section 5.3 is included for comparative purposes. . . . .	132
5.7	A reconstruction of the David model at depth 15. . . . .	135

# Chapter 1

## Introduction

*Then this is enough to tell you what I mean by ‘shape’. For I say this of every shape: a shape is that which limits a solid; in a word, a shape is the limit of a solid. – Socrates to Meno, (Plato, Meno, 77)*

One of the most fundamental concepts within the field of computer graphics is *shape*. Any object seen in a computer-generated image, a scientific visualization, a game or a movie is a shape with a virtual representation that is created, manipulated and then rendered entirely within a computer.

Many representations of shape are used in computer graphics, ranging from implicit mathematical formulations to the *triangle mesh*. A triangle mesh is a discrete structure that represents a surface as a set of points in three-dimensional space, connected in groups of three which form the triangular facets of a surface. Although a surface represented in a discrete manner such as this cannot represent a smooth surface, sufficiently small triangles can give an approximation of a smooth

## CHAPTER 1. INTRODUCTION

surface that will be visually indistinguishable when viewed on a movie or computer screen. Triangle meshes have become the most common representation for surfaces primarily because the specialized computer hardware used to render interactive 3D scenes use this representation internally.

In the most basic setting, virtual representations of 3D models are created manually, using modeling packages in which each vertex, edge or face in the mesh is created and modified individually. Although this provides a high degree of artistic freedom and works well for small models with thousands of triangles, the ever-increasing demand for realism in computer-generated scenes has significantly increased the model complexity, and therefore the time and cost of using these techniques. New methods for generating models which can automate large parts of the modeling process and reduce the amount of human interaction required have become essential.

### **1.1 3D Scanning**

The advent of 3D scanning techniques has significantly changed the way models are created. Instead of using manual techniques to create virtual representations of objects, real world objects can be scanned, providing an automated way of generating highly detailed meshes.

In addition to improving the efficiency of 3D modelling, scanning technologies

## CHAPTER 1. INTRODUCTION

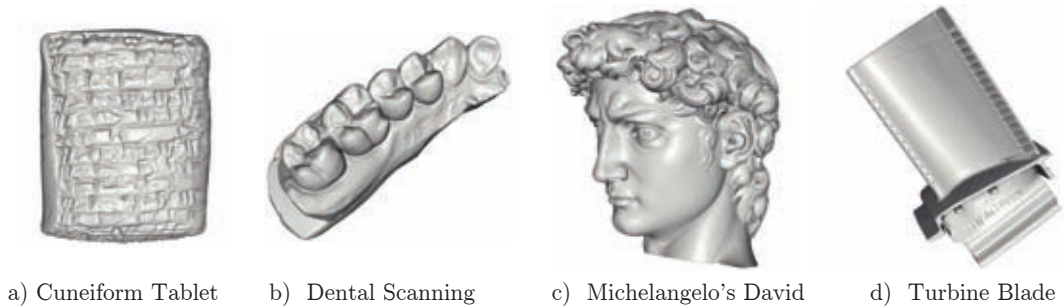


Figure 1.1: Four examples of reconstructed objects from different disciplines.

have extended the use of virtual models to a broad group of application domains. Figure 1.1 highlights four examples of objects that have been scanned for use in different disciplines. A 3D scan of a cuneiform tablet (Figure 1.1a) allows scholars to read and interpret the text inscribed in these stone tablets recovered from archaeological sites dating to the 34th century BC. Scanning a patient's teeth (Figure 1.1b) allows a more accurate fitting of dental implants. A highly detailed reconstruction of Michaelangelo's *David* statue (Figure 1.1c) allows art historians to study the techniques used to create these masterpieces. And finally, scans of mechanical parts, such as a turbine blade (Figure 1.1d), can be used for quality control in the manufacturing industry to detect defects.

One of the most widely used techniques for collecting detailed surface data is stereo triangulation based range scanning. These scanners use a registered light source and camera to triangulate points on the surface of an object. Because the relative positions and orientations of the light source and camera are precisely known, the three-dimensional location of points on the surface can be computed

## CHAPTER 1. INTRODUCTION

by combining registration information and the location of features within the camera's image plane. Because of the reliance on triangulation, the accuracy of these type of scanners decreases as the distance between the camera and the object increases. In practice, however, they are capable of producing high quality scans with sub-millimeter precision for objects within a range of several meters.

Typically, it is not possible to obtain a complete sampling of an object's surface from a single image or scan. To get complete coverage of an object many overlapping scans from different viewpoints are required. Small objects, such as the "Bunny" shown in Figure 1.2 may be constructed from only ten scans, totalling a few hundred thousand samples. Larger objects may contain thousands of individual scans and total hundreds of millions of samples.

The challenge in combining multiple scans together is that the scans must be aligned. The classical technique for aligning scans is the iterative closest point (ICP) [57] algorithm. Given an initial estimation of the alignment of two scans, the ICP algorithm iteratively reduces the misalignment producing a rigid body transformation to register the two scans. This pairwise technique can be applied to all overlapping scans to produce a consistent global alignment. Because some components of the scanning process can distort scans in non-linear ways, recent methods (e.g. Brown *et al.* [12]) further improve the alignment by applying non-linear transformations to the scans during the registration process.

Although 3D scanning and the subsequent registration of multiple scans

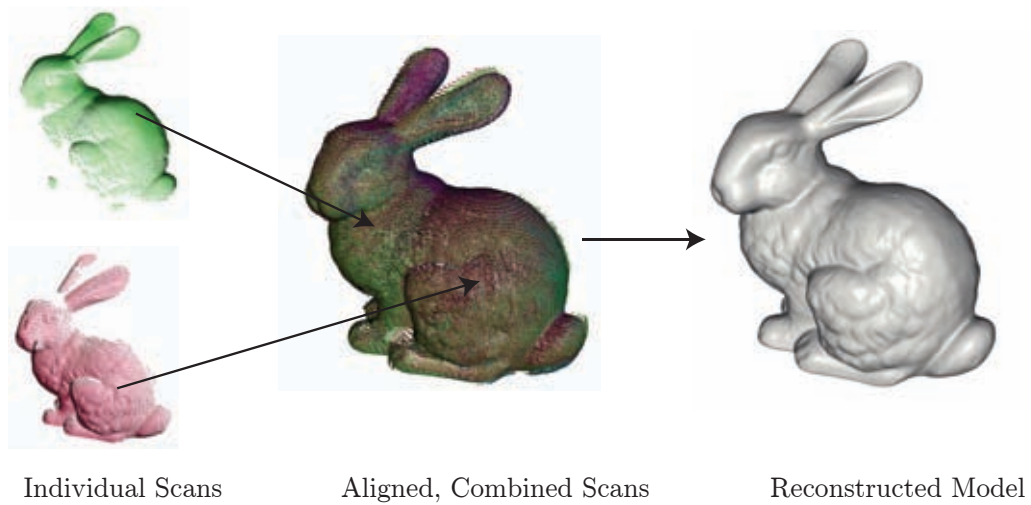


Figure 1.2: An example of the reconstruction of the “Bunny” model. Individual scans of the real object are first aligned and combined before a *surface reconstruction* algorithm produces the final model.

provides high resolution geometry, it does not provide a fully connected mesh of the surface: each scan is still represented as a separate patch of the surface. For most uses, a single surface mesh is required.

## 1.2 Surface Reconstruction

*Surface reconstruction* is the process of the automated generation of three-dimensional surfaces from a discrete sampling of the surface of a real object acquired through 3D scanning. This can be an under-constrained process since the reconstruction process must infer the shape between the samples, and there may be many plausible surfaces that can be generated from any given set of samples.

## CHAPTER 1. INTRODUCTION

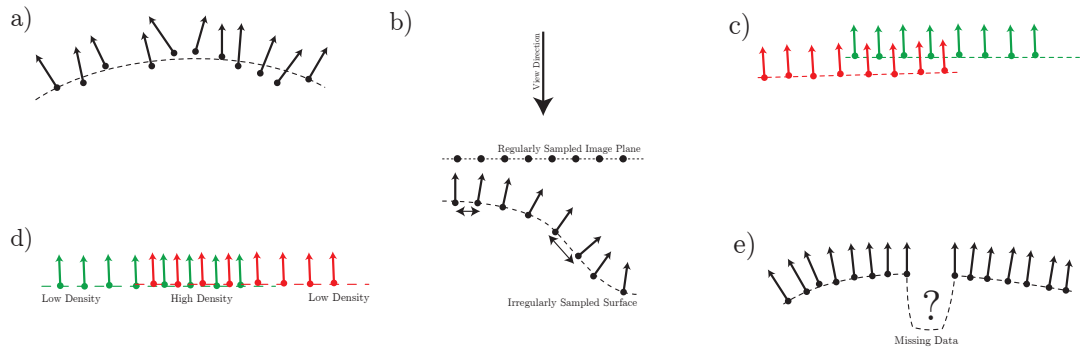


Figure 1.3: Illustrative examples of the different types of data anomalies present in three-dimensional scan data: a) noise, b) anisotropy, c) misalignment, d) non-uniformity, and e) missing data.

One of the largest challenges in reconstructing surfaces robustly and accurately is dealing with the many anomalies that are present in data that are obtained from the scanning of real-world objects. There are many aspects to the data that make the task of reconstruction particularly challenging.

- **Noise:** (Figure 1.3 a and b) The process of scanning involves capturing measurements with an imaging device which, unavoidably, introduces noise into all measurements. This noise manifests itself as uncertainty in the positions of three-dimensional points or the orientation of surface normals in the dataset. The level of noise is often variable and related to various local characteristics of the surface (for example, reflectivity, or translucency) and to the orientation of the surface in relation to the scanner (for example, parts of the surface that are more oblique tend to have higher levels of noise).
- **Misalignment:** (Figure 1.3 c) When the samples are derived from multiple

## CHAPTER 1. INTRODUCTION

scans, non-linear distortions and the lack of features in regions of scan overlap can lead to imperfect alignment of scans. The consequence of scan misalignment in the context of reconstruction is that the same patch of a surface may be represented by multiple overlapping scans which disagree. This often creates a situation where a single surface is represented in the scan data as multiple “sheets” of samples, offset from each other.

- **Non-uniformity:** (Figure 1.3 d) Although a scan may form a regular sampling of a grid in sensor space, the transformation of this data into object space may create a distorted distribution of points. As a consequence, the density of samples from a single scan may be highly anisotropic. Additionally, as scans from multiple points of view are combined into the final dataset, the sampling density becomes non-uniform. On a large scale, some parts of the object may have been intentionally scanned in more detail than other parts. On a small scale, the way in which multiple scans coincide may cause dramatic, localized variations of sampling density (for example, when an area of the surface is covered by two scans instead of one, the local sampling density will double). Highly non-uniform datasets are challenging to reconstruct because one can no longer assume that there exists a single radius representing the expected distance between neighboring samples.
- **Missing data:** (Figure 1.3 e) During the process of scanning an object, it is



## CHAPTER 1. INTRODUCTION

not always possible to capture scans of all parts of the surface, which leaves coverage holes in the resulting dataset. Such circumstances can arise when small concavities or hard-to-reach places are not visible to a scanner due to physical constraints, or merely due to an oversight during the scanning process. In many contexts, it is desirable to fill holes in the dataset with a “plausible” surface.

Figure 1.4 provides examples of how multiple anomalies combine in two of the datasets we use in this dissertation. Figure 1.4a shows a sample of data from the front feet of the “Bunny” dataset. In this example, we can see and a hole (1), multiple scans overlapping creating widely varying local sampling densities (2), and distortion of the regular structure of scans when projected onto the surface forming anisotropic sampling density (visible as samples forming rows where the distance between samples within the row is much closer than the distance between rows) (3). Figure 1.4b shows a sample of data from the left eye of the “David” dataset. In this example we can see a particularly interesting case of scan misalignment on the left hand side of the lobe protruding from the top of the pupil (4) as well as noise, illustrated by the specked appearance of the shading (5).

In addition to difficulties arising due to noise in the acquisition, the sheer size of recently acquired datasets creates a new set of challenges. New scanning and acquisition technologies are driving a dramatic increase in the size of datasets

## CHAPTER 1. INTRODUCTION

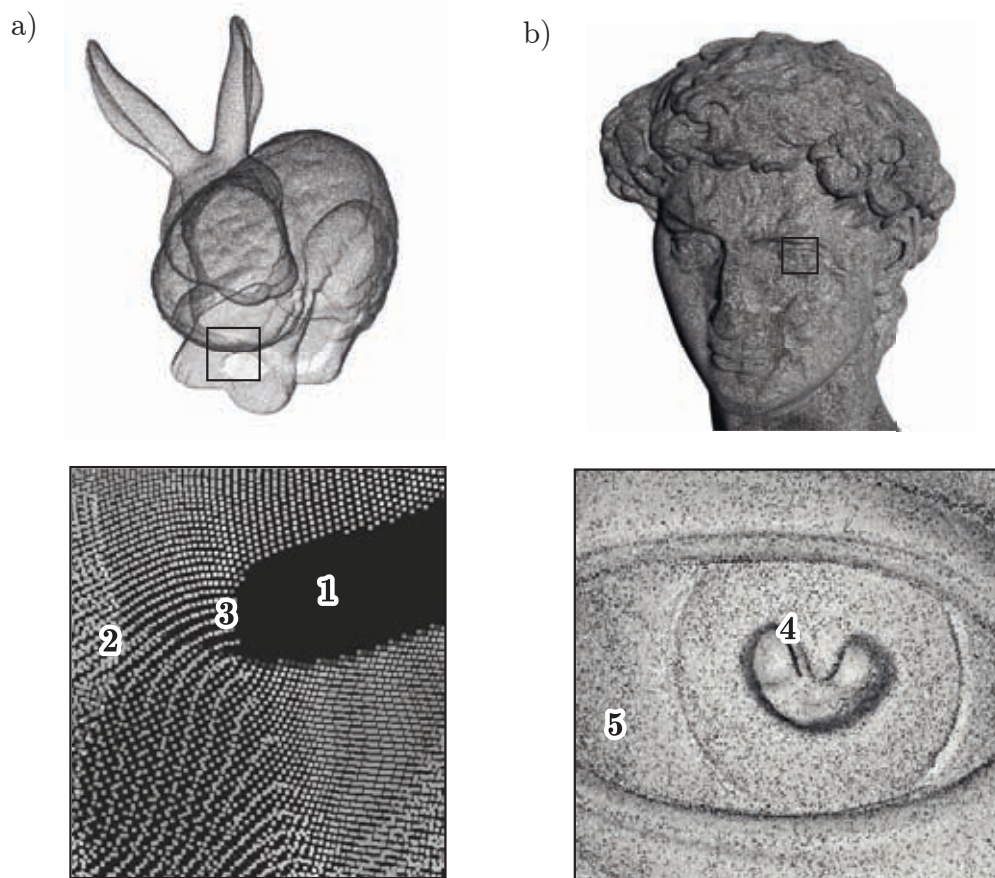


Figure 1.4: Two examples showing how multiple types of anomalies combine in real-world data.

for surface reconstruction. A number of cultural heritage projects, including the Digital Michelangelo project [34] and Pietà project [9] have scanned sculptures with datasets approaching one billion point samples each. New computer vision techniques [50] allow three dimensional point clouds to be extracted from photo collections; with an abundance of photographs of the same scene available through online photo sites, the potential for truly massive datasets is within reach. The size of these datasets presents modern surface reconstruction techniques with a

new set of challenges: Processing such large datasets can require thousands of hours of computing time and hundreds of gigabytes of storage.

## 1.3 Outline of Dissertation

In Chapter 2, we review a wide range of existing surface reconstruction techniques and develop a taxonomy to group methods based on their design and implementation. In Chapter 3 we present the *Poisson Surface Reconstruction* algorithm, a new technique for reconstructing surfaces that is computationally efficient and robust. In Chapter 4 we show that, despite being a global problem, the Poisson technique can be extended to a streaming computation model, allowing for the reconstruction of the extremely large datasets available from large scale 3D scanning projects by only requiring a small subset of the data to be accessible in memory at any one time. In Chapter 5 we show how the streaming technique can be adapted to process the octree data in parallel, allowing faster processing of large datasets on both shared memory and distributed memory computer systems. We conclude in Chapter 6 with a summary of our work, and a brief discussion of directions for future scholarship.

## Chapter 2

# Surface Reconstruction

Surface reconstruction has been a well studied problem in computer graphics and vision and a wide variety of methods have been suggested. The general approach of a surface reconstruction method can be most broadly categorized as either discrete or continuous. Discrete methods utilize the pointset directly, or structures from computational geometry to define the surface. Continuous methods take either a *surface fitting* approach, where a surface is fit directly to the samples, or a *function fitting* approach, where an implicit function is first fit to the samples and then used to define a surface.

There are a wide range of methods for scanning. In addition to triangulation based range scanners, many techniques from computer vision, including shape from stereo [7] and shape from shading [26] can take images of an object and produce a three-dimensional representation. Because of this diversity, there are

## CHAPTER 2. SURFACE RECONSTRUCTION

several different forms in which input data for surface reconstruction can take. Many techniques make use of these different forms to aid the reconstruction process. In the most general form, the surface is represented by a *point set*  $P = \{p_1, \dots, p_N\}$  where  $p_i \in \mathbb{R}^3$  are a sampling of positions on (or near) a surface. In addition to position of each sample, many scanning techniques can also provide information about the orientation of the surface at each sample point. In these cases, the scan data data forms an *oriented point set*  $P = \{(p_1, n_1), \dots, (p_N, n_N)\}$  where  $p_i, n_i \in \mathbb{R}^3$  and  $n_i$  represents the normal vector at each sample. A more specialized, but very common form of scan data, is the *range image*. A range image is a two-dimensional regular grid  $R \in \mathbb{R}^{N \times M}$  of values where each value represents the distance from the scanner source to points on a surface. With information such as the position of the scanner center and the scanner's orientation, the three-dimensional location of sample points can be computed from each element of the range image. Additionally, the implicit array structure provides connectivity between adjacent points, allowing the range image to represent a quadrangulated patch of a surface. Using this topology, a range image can also define a per sample surface normal.

In the remainder of this chapter, we will briefly describe some of the more significant surface reconstruction methods from the literature following the taxonomy of Figure 2.1. We also classify each method according to the type of input data required in Figure 2.2.

## CHAPTER 2. SURFACE RECONSTRUCTION

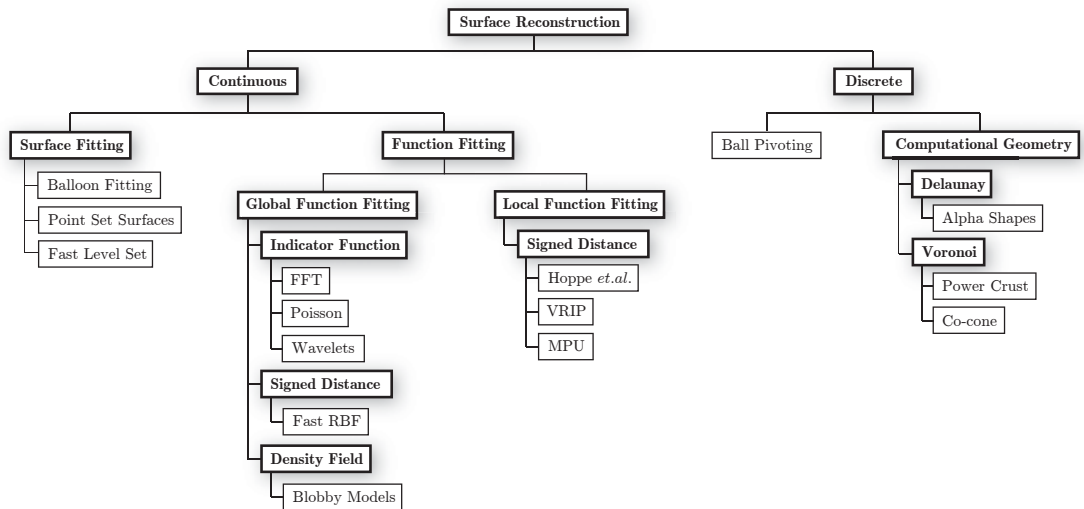


Figure 2.1: A taxonomy of surface reconstruction methods, based on the general approach to solving the reconstruction problem.

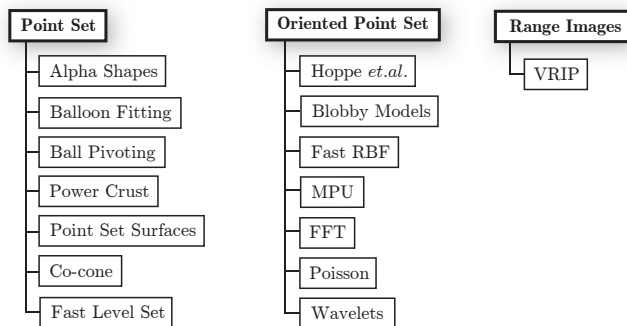


Figure 2.2: A categorization of surface reconstruction methods, based on the type of input data required.

## 2.1 Discrete Methods

### 2.1.1 Computational Geometry

Many of the earliest approaches to surface reconstruction used techniques from computational geometry. In general, these approaches take a set of points and compute combinatorial structures such as the Delaunay tetrahedralization or Voronoi diagram. From these partitions of space, a labeling process defines each partition as either interior or exterior to the shape, and the reconstructed surface is defined as the set of faces between interior and exterior regions. The surface that results from this process typically interpolate most or all of the points in  $P$ .

### 2.1.2 Alpha Shapes

Among the first of these was *alpha shapes* [20]. The alpha-shape  $S_\alpha(P)$  of a point-set  $P$  is a simplicial complex that can be thought of as a generalization of the convex hull, parameterized by  $\alpha$ . As  $\alpha \rightarrow \infty$ , the alpha shape is the convex hull of  $P$ . As  $\alpha \rightarrow 0$ , the alpha shape is  $P$  itself. For other values of alpha, a set of shapes are defined which are constructed from the Delaunay tetrahedralization  $DT(P)$ . The alpha shape is formed by iteratively removing all exposed edges of  $DT(P)$  where  $|x_i - x_j| < \alpha, i \neq j$ . Faces and tetrahedra are removed from  $S_\alpha$  when one of their corresponding edges or faces is removed.

Although simple to construct, alpha shapes have limited utility in surface reconstruction, especially when reconstructing from real-world data. Because  $\alpha$  is a *global* parameter, it can be hard to choose a single  $\alpha$ -value that can be used to extract a good representation of the surface everywhere: this becomes increasingly challenging when sampling density in  $P$  is non-uniform. Additionally, because  $S_\alpha(P)$  is an arbitrary simplicial complex, the resulting shape is not guaranteed to be manifold.

### 2.1.3 Power Crust

The power crust algorithm [4, 5] reconstructs a surface  $S$  by making the observation that a surface can be represented by its *medial axis*, or skeleton –  $MAT(S)$ . The medial axis is defined as the set of all points that are equi-distant to two or more points on  $S$ . The power crust algorithm approximates  $MAT(S)$  by constructing the Voronoi diagram of  $P$ ,  $V(P)$ . From  $V(P)$  the Voronoi vertices that form *poles* are used to define the points on the medial axis and are used to construct a set of *polar balls*. A vertex  $v \in V(P)$  is a pole  $p$  if it is the farthest vertex from the center of a Voronoi cell that it belongs to. Each pole defines a ball centered at  $p$  with a radius equal to the distance of  $p$  from the nearest point in  $P$ . To compute a surface, the polar balls are used to construct a power diagram (a Voronoi diagram of the poles, weighted by radius), cells of the power diagram are labelled as “interior” and the surface (“power crust”) is extracted as



the boundary.

With the power crust algorithm, Amenta *et al.* also provided theoretical guarantees. In particular, provided  $P$  is *sufficiently dense*, the surface that the power crust algorithm reconstructs is a (provably) smooth surface that is homeomorphic to the surface from which the points were sampled. Formally, a set of samples is defined to be sufficiently dense when the distance from any surface point to the nearest sample is at most a small constant  $\epsilon$  times the distance to medial axis. Intuitively, this means that  $P$  must be more densely sampled in regions of high curvature, or regions where other parts of the surface are nearby.

### 2.1.4 Ball Pivoting

The ball pivoting algorithm [8] reconstructs a surface  $S$  from a point cloud  $P$  using a ball of radius  $\rho$ . The surface is constructed from the set of triangles constructed from three distinct points in  $P$  which can form a ball of radius  $\rho$  without containing any other points from  $P$ . The algorithm is implemented by taking a “seed” ball and successively pivoting the ball across triangle edges until no more points can be visited. Although this method is highly efficient and can operate on large datasets, it has a number of practical limitations. Like methods from computational geometry, this method produces a surface that interpolates most of the input points, which can reconstruct undesirable sampling noise. In addition, as with alpha shapes, the value of  $\rho$  is constant which reduces the utility

when dealing with non-uniform data.

## 2.2 Continuous Methods

### 2.2.1 Surface Fitting

Surface fitting approaches take a set of points and deforms a base shape until it fits the points.

#### 2.2.1.1 Balloon Fitting

The “Balloon Fitting” method of Chen *et al.* [15] uses an approach inspired by the inflation of a balloon. The method takes a point set  $P$  as an input, along with a seed surface  $S$  (an icosahedron) that is completely contained inside the desired surface.  $S$  is used to form a mass-spring system where each vertex is connected to its neighbors via springs. The surface is iteratively grown by increasing the internal pressure of  $S$ , which causes each triangle to inflate in the direction of its surface normal. To ensure that triangles in  $S$  are kept sufficiently small, triangles are split when the spring force acting between two vertices exceeds some threshold. Once a triangle in  $S$  reaches a point in  $P$ , or, has no points in  $P$  in front of it (i.e. a hole) the vertices of the triangle become “anchored” and do not move in future updates. The surface is complete once all vertices become anchored.

## CHAPTER 2. SURFACE RECONSTRUCTION

In practice, there are two difficulties with the “Balloon Fitting” method. First, finding a seed surface automatically is not an easy problem, typically requiring user intervention. Second, because of the way the surface is inflated to fit the model, the genus of the surface is restricted to be the genus of the seed surface.

### 2.2.1.2 Fast Level Set Method

The fast level set method of Zhao *et al.* [58] takes an implicit approach to the surface-fitting problem. Given a general input data set ( $S$ ) that may contain points, curves or surface patches, a distance function  $d(x) = \text{dist}(x, S)$  is computed. Given an arbitrary initial surface  $\Gamma$ , an energy function  $E(\Gamma)$  is defined using  $d(x)$  and the energy flow is used to evolve the surface toward a better approximation of  $S$ .

Because the topological structure of the reconstructed surface is not known *á priori*, it is not effective to represent  $\Gamma$  in an explicit form. Instead, this method uses a level set formulation, allowing the topology of the surface to change throughout the evolution process.

### 2.2.1.3 Point Set Surfaces

The “Point Set Surfaces” method of Alexa *et al.* [3] uses the moving least squares (MLS) projection operator [33] to define a surface  $M$  implicitly from a set of points  $P$ . The MLS operator is a projection operator  $\Pi$  that takes a point  $r$  and

## CHAPTER 2. SURFACE RECONSTRUCTION

maps it to the unknown surface  $S$ . Given a point  $r$  that is near  $M$ , the projection operator is formed by fitting a plane  $H$  around  $r$  that minimizes the weighted sum of squared distances to all  $p_i \in P$ . Using the plane  $H$  as a parametrization domain, the surface is locally represented by the graph of a polynomial function  $g$  with approximates the heights of the  $p_i$  over  $H$ . The projection operator is then defined by projecting  $r$  onto  $H$  and evaluating  $g$  at the projected point to obtain the height of  $\Pi(r)$  over  $H$ . One aspect of this method that is different to all other methods we discuss in this chapter, is that the reconstructed surface  $S$  is not represented as a mesh, but as a dense collection of points that can be rendered with point-based rendering methods [35].

### 2.2.2 Implicit Function Fitting

Function fitting approaches attempt to define a function  $F : \mathbb{R}^3 \rightarrow \mathbb{R}$  such that the interior and exterior of the shape can be distinguished and the surface can be extracted as a level-set of  $F$ . In its essence, surface reconstruction via implicit function fitting is a scattered data interpolation problem [21]: The input point set forms a set of constraints to which an unknown function  $F$  is fit. A variety of different choices for  $F$  have been used, including signed [13, 17, 25] and unsigned [42] distance functions, and the indicator function [31, 39].

### 2.2.3 Local Function Fitting

In contrast to global function fitting approaches in which an input sample can influence the values of  $F$  over the entire domain, in local function fitting approaches a sample only influences the values of  $F$  in a small, localized neighborhoods. In practice, these approaches tend to be efficient because the local reconstruction of the surface only needs to consider a small subset of points from the dataset. The challenge for local methods is defining the locality of a sample. If the choice of neighborhood is too small, errors in the data, such as noise and misalignment can result in undesirable artifacts in the resulting surface. When the neighborhood is large, the solution can become inefficient to compute.

#### 2.2.3.1 Hoppe *et al.*

The approach of Hoppe *et al.* [25] was one of the first function fitting approaches to reconstruct a surface from an *unorganized* point set (i.e. a set of three-dimensional points with no normal or topological information). This approach constructs an approximation to the signed distance function,  $F$ , of the unknown surface. The signed distance function of a surface  $S$ , is a scalar function  $F : \mathbb{R}^3 \rightarrow \mathbb{R}$  where the value of  $F(x)$  is defined as the Euclidean distance of  $x$  from the nearest point on  $S$  with points inside  $S$  assigned a negative distance, and points outside assigned a positive distance value. Once  $F$  is computed, the surface is extracted as the zero-set of  $F$  using a contouring algorithm.

## CHAPTER 2. SURFACE RECONSTRUCTION

To define  $F$ , each point  $p_i \in P$  is associated with an oriented plane  $T_i \equiv \langle p_i, n_i \rangle = 0$  which defines a local linear approximation to the Euclidean distance function of the surface. Each  $T_i$  is estimated by fitting a plane to the  $k$ -nearest points to  $p_i$  in  $P$ . The plane normal is defined as the smallest eigen-vector of the covariance matrix of the points in the neighborhood.

To define surface normals that are consistently oriented (essential to robustly construct the signed distance function) an additional step is taken to correctly orient the tangent planes. To do this, a graph is formed where each tangent plane  $T_i$  forms a node  $N_i$  in the graph. Two nodes of the graph  $N_i$  and  $N_j$  are connected with an edge when the  $k$ -neighborhoods of  $T_i$  and  $T_j$  have at least one point in common. Edges are weighted according to the absolute value of the dot product of  $n_i$  and  $n_j$ . Then, a minimal spanning tree of the graph is created and the normal directions are defined by assigning an (arbitrary) orientation to a node and propagating the orientation through the tree.

### 2.2.3.2 Volumetric Range Image Processing (VRIP)

The Volumetric Range Image Processing (VRIP) method [17] reconstructs surfaces from an aligned set of range images. From each range image  $R_i$ , a view dependent signed distance function  $d_i(x)$  and a corresponding weight function  $w_i(x)$  are constructed. Then, a combined distance function  $D(x)$  is constructed as  $\frac{\sum w_i(x)d_i(x)}{\sum w_i(x)}$  and a surface is extracted as the iso-surface  $D^{-1}(0)$ .

## CHAPTER 2. SURFACE RECONSTRUCTION

To prevent the distance function  $d_i$  of one scan influencing  $D$  far away from the scan, the weight function  $w_i$  tapers to zero over a small distance called the *ramp* size. The ramp size is typically chosen to be half the maximum error expected in range image distances. Because of the spatial locality of  $w_i$ , large portions of  $w_i d_i$  (and therefore  $D$ ) are zero. This is exploited to reduce the storage requirements of  $D$  by using run-length encoding.

In general, regions of the surface without range image coverage will not have a well-defined iso-surface, leaving boundary contours in the reconstructed surface. To seal some of these holes, VRIP uses *space carving* to exploit the fact that a range image not only gives information about where the surface is, but also where it is not. This is used to label the parts of space at which the view from the scanner is un-occluded. Carving out the un-occluded regions from the reconstruction volume results in an effective way for sealing some of these holes.

### 2.2.3.3 Multi-level Partitions of Unity (MPU)

The MPU [43] method reconstructs an approximation to the signed distance function from an oriented point set. The signed distance function  $F$  is defined as a set of locally defined functions  $f_i$  blended together with a set of weights which form a *partition of unity* (that is, for a given point  $x$  the weights always sum to one). To construct the local functions  $f_i$  an octree is used to recursively partition space. For a given octree node  $o_i$ , a (piecewise) quadratic approximation  $Q_i$  is

## CHAPTER 2. SURFACE RECONSTRUCTION

fit to the samples that fall within the spatial bounds of the octree node. If  $Q_i$  is a poor representation of the points (as measured by the Taubin distance [51]) the octree node is split, and the fitting process is repeated for each octant. If the number of points in an octree node is too small,  $Q_i$  may not be a robust representation. In these cases, the next closest points are incrementally included in computing  $Q_i$  until a minimum number of points is reached. Once a  $Q_i$  has been fit to all nodes in the octree, local signed distance functions  $f_i$  are computed from  $Q_i$ . To form the final implicit function  $F$ , the  $f_i$  are blended together using the partition of unity.

### 2.2.4 Global Function Fitting

Global function fitting approaches consider all points when defining the value of the implicit function at a location. In general, global approaches are more robust, as a local effects like noise or scan misalignment have a less direct influence on the value of the function. There have been a number of surface reconstruction techniques that use global function fitting methods. We briefly describe some of these approaches.

#### 2.2.4.1 Blobby Models

The concept of the “Blobby Model” was introduced by Blinn [10]. The idea was that a 3D model can be represented as an iso-surface of a field generated



## CHAPTER 2. SURFACE RECONSTRUCTION

from a number of primitives:  $F(x) = \sum_{i=1}^N b_i e^{-a_i f_i(x)}$  where  $b_i$  and  $a_i$  control the amplitude and fall-off of the primitive and  $f_i$  is a function that describes the shape of the primitive (Often,  $f_i(x) = \|x - x_i\|^2$ , where  $x_i$  is the origin of the primitive).

The work of Muraki [42] applied Blinn’s work to the context of surface reconstruction. The problem is, given a range image  $R$ , to find a set of primitives that can generate a blobby model representation of  $R$ . Since directly finding  $N$  primitives to fit  $R$  is a difficult problem, a greedy approach is used. Starting with  $N = 1$ , primitives are recursively split and an energy minimization problem is solved to fit the new primitives.

One of the problems with using a blobby model approach for surface reconstruction is a limitation of the blobby representation itself. First, because the primitives are smooth functions, objects with sharp features require a large number of primitives to be represented accurately. Second, because primitives have global support, local changes may introduce undesirable artifacts in other regions of  $F$ .

### 2.2.4.2 Fast RBF

The FastRBF approach [13] takes a scattered data interpolation interpretation of the reconstruction problem. The authors define  $F$  to be an approximation to the signed distance function of the surface. To define  $F$ , first, each sample point  $p_i$  is used to set a constraint on  $F$  such that  $F(p_i) = 0$ . To avoid the trivial

## CHAPTER 2. SURFACE RECONSTRUCTION

solution of  $F = 0$ , additional constraints are added. “Off surface” points  $p_i^{in}$  and  $p_i^{out}$  are defined as  $p_i \pm \delta n_i$  that form constraints on  $F$  such that  $F(p_i^{in}) = -\delta$  and  $F(p_i^{out}) = +\delta$ . Care is taken to ensure that these interior and exterior constraints do not conflict in regions where the surface folds together. To solve for  $F$ , a radial basis function scheme is used.  $F$  is represented as the weighed sum of radial basis function  $F(x) = \sum_{i=1}^N w_i \phi(\|x - c_i\|)$  where  $c_i$  is a constraint center,  $w_i$  is a weight and  $\phi(x)$  is a function that has global support. Given the values  $f_i$  at the constraint points, a set of weights  $w_i$  can be found by solving a linear least squares problem.

Because  $\phi(x)$  has global support, the linear system to find  $w_i$  is dense and poorly conditioned, and is therefore difficult to solve robustly as  $N$  grows. To use radial basis functions to reconstruct surfaces from a large number of points, a number of optimizations and approximations are used. First, fast multi-pole methods are used to evaluate  $F(x)$ . This optimization works by reducing the number of constraints that need to be evaluated at  $x$  by approximating clusters of centers far from  $x$  as a single constraint. Second, a greedy algorithm is used to iteratively fit a small number of constraints to a given point set in order to reconstruct the surface to within a desired fitting accuracy.

### 2.2.4.3 Fast Fourier Transform

The work of Kazhdan [31] was the first function fitting method which used the indicator function as its choice of implicit function. For a given solid  $M$ , the indicator function  $\chi_M$  is a scalar function that is defined as  $\chi_M(x) = 1$  if  $x \in M$  and  $\chi_M(x) = 0$  otherwise. The FFT method constructs the indicator function through an application of Stokes' theorem, which expresses a volume integral as a surface integral, a quantity that can be approximated from an oriented point set. Specifically, the work shows that the Fourier coefficients of the indicator function can be expressed as surface integrals computed using the oriented point samples. As a result, the indicator function can be obtained by computing the Fourier coefficients and running the inverse Fourier transform. The surface is then extracted from the volume using the marching cubes [37] algorithm. Non-uniformity in the input point set is handled by weighting the contribution of each oriented point to the vector field by the result of a kernel density estimator.

Because of its global nature, the FFT method is robust to a variety of degeneracies in the input data, including noise (in both sample position, and orientation) and non-uniform sampling. Holes in the input data are plausibly and smoothly filled in the output mesh. However, a significant disadvantage of this method is the spatial and temporal complexity. Using an  $O(r^3)$  regular grid limits the practicality of the method when reconstructing large models with high resolution. More recent work by Schall *et al.* [46] has taken the FFT approach and

## CHAPTER 2. SURFACE RECONSTRUCTION

used it in an adaptive setting. This approach partitions a large model using an adaptive octree and computes a number of local FFT's that get blended for the final indicator function, in a manner similar to the blending of the MPU approach. Although this provides a more scalable solution than the original method, the local decisions used to form and blend local FFT reconstructions can make the method less robust.

### 2.2.4.4 Wavelets

The Wavelet based-approach of Manson *et al.* [39] uses a similar approach as the FFT method, computing the indicator function from an oriented point set using Stokes' theorem. However, instead of using the Fourier basis, this method uses an orthogonal wavelet basis with compact support. The key observation is that, in the case of the Fourier basis, computing each Fourier coefficient requires summation across all of sample points. In contrast, when using a wavelet basis (with compactly supported basis functions) computing each wavelet coefficient only requires the summation of samples within the support of the basis.

This approach offers a number of practical advantages over the FFT based method. First, the algorithm is more efficient. Second, the spatial complexity of the algorithm is lower, since only wavelet coefficients whose support overlaps the sample points need to be stored explicitly.

### 2.2.4.5 Our Approach

The approach that we describe in this dissertation is similar in spirit to the FFT approach. Like the FFT approach, we reconstruct surfaces by first constructing an approximation the indicator function  $\chi$  from a set of oriented points, and then extracting a surface from  $\chi$ . We address a number of the limitations of the FFT approach by using an adaptive function basis formed on in octree.

## Chapter 3

# Poisson Surface Reconstruction

Reconstructing 3D surfaces from point samples is a well-studied problem in computer graphics. It allows for the fitting of surfaces to scanned data, the filling of surface holes, and the re-meshing of existing models. In this chapter, we describe a surface reconstruction approach that expresses surface reconstruction as the solution to a Poisson equation.

### 3.1 The Poisson Idea

Like much previous work, we approach the problem of surface reconstruction using an implicit function framework. Specifically, like [31] we compute a 3D *indicator function*  $\chi$  (defined as 1 at points inside the model, and as 0 at points outside), and then obtain the reconstructed surface by extracting an appropriate

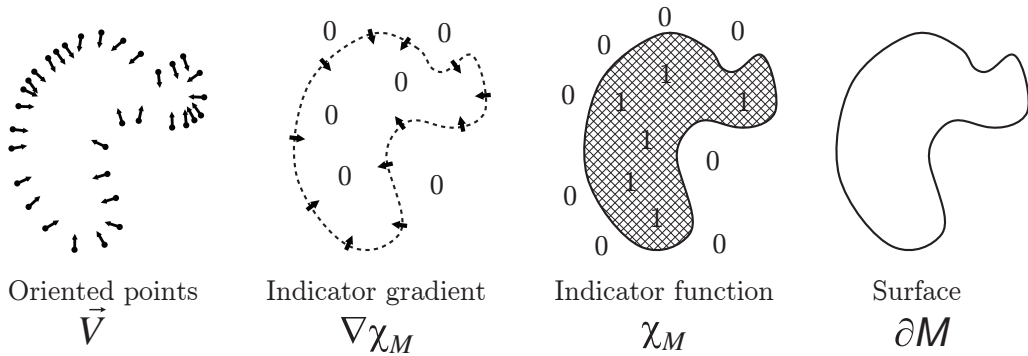


Figure 3.1: Intuitive illustration of Poisson reconstruction in 2D.

iso-surface.

The key insight in our approach is that there is an integral relationship between oriented points sampled from the surface of a model and the indicator function of the model. Specifically, the gradient of the indicator function is a vector field that is zero almost everywhere (since the indicator function is constant almost everywhere), except at points near the surface, where it points in the direction of the inward surface normal. Thus, the oriented point samples can be viewed as samples of the gradient of the model’s indicator function. Figure 3.1 illustrates this idea in two dimensions.

The problem of computing the indicator function therefore reduces to inverting the gradient operator; that is, finding the scalar function  $\chi$  whose gradient best approximates the vector field  $\vec{V}$  defined by the samples (i.e.  $\min_{\chi} \|\nabla\chi - \vec{V}\|$ ). Applying the divergence operator, this variational problem transforms into a

## CHAPTER 3. POISSON SURFACE RECONSTRUCTION

standard Poisson problem:

$$\Delta\chi \equiv \nabla \cdot \nabla\chi = \nabla \cdot \vec{V}. \quad (3.1)$$

We will make these definitions precise in Sections 3.2 and 3.3.

Formulating surface reconstruction as a Poisson problem offers a number of advantages. Many implicit surface fitting methods first segment the data into regions for local fitting, and then combine these local approximations using blending functions. In contrast, Poisson reconstruction is a global solution that considers all the data at once, without resorting to heuristic partitioning or blending. Thus, like radial basis function (RBF) approaches, Poisson reconstruction creates smooth surfaces that robustly fit noisy data. But, whereas ideal RBFs are globally supported and non-decaying, the Poisson problem admits a hierarchy of *locally supported* functions, and therefore its solution reduces to a well-conditioned sparse linear system.

Moreover, in many implicit fitting schemes, the value of the implicit function is constrained only near the sample points, and consequently the reconstruction may contain spurious surface sheets away from these samples. Typically, this problem is reduced by introducing auxiliary “off-surface” points (e.g. [13, 43]). With Poisson surface reconstruction, such surface sheets do not arise because the gradient of the implicit function is constrained at *all* spatial points. In particular, it is constrained to zero away from the samples.



There has been broad interdisciplinary research on solving Poisson problems and many efficient and robust methods have been developed. One particular aspect of our problem instance is that an accurate solution to the Poisson equation is only necessary near the reconstructed surface. This allows us to leverage adaptive Poisson solvers to develop a reconstruction algorithm whose spatial and temporal complexities are proportional to the size of the reconstructed surface.

## 3.2 Approach

The input to the surface reconstruction is an oriented point set  $P = \{s_i = (p_1, n_1), \dots, s_N = (p_N, n_N)\}$  that consists of a sample  $s_i$  with a position  $s.p$  and an inward-facing normal  $s.n$ , assumed to lie on or near the surface  $\partial M$  of an unknown model  $M$ . The goal is to reconstruct a watertight, triangulated approximation to the surface by approximating the indicator function of the model and extracting the iso-surface, as illustrated in Figure 3.2.

In the next sections, we derive a relationship between the (smoothed) gradient of the indicator function and an integral of the normal field over the surface. We then approximate this surface integral by a summation over the given oriented point samples. Finally, we reconstruct the indicator function from this gradient field as the solution to a Poisson problem.

### 3.2.1 Defining the gradient field

Because the indicator function is a piecewise constant function, explicit computation of its gradient field would result in a vector field with unbounded values at the surface boundary. To avoid this, we convolve the indicator function with a smoothing filter and consider the gradient field of the smoothed function. The following lemma formalizes the relationship between the gradient of the smoothed indicator function and the surface normal field.

**Lemma:** Given a solid  $M$  with boundary  $\partial M$ , let  $\chi_M$  denote the indicator function of  $M$ ,  $\vec{N}_{\partial M}(p)$  be the inward surface normal at  $p \in \partial M$ ,  $\tilde{F}(q)$  be a smoothing filter, and  $\tilde{F}_p(q) = \tilde{F}(q-p)$  its translation to the point  $p$ . The gradient of the smoothed indicator function is equal to the vector field obtained by smoothing the surface normal field:

$$\nabla \left( \chi_M * \tilde{F} \right) (q_0) = \int_{\partial M} \tilde{F}_p(q_0) \vec{N}_{\partial M}(p) dp. \quad (3.2)$$

**Proof:** To prove this, we show equality for each of the components of the vector field. Computing the partial derivative of the smoothed indicator function with

## CHAPTER 3. POISSON SURFACE RECONSTRUCTION

respect to  $x$ , we get:

$$\begin{aligned}
 \frac{\partial}{\partial q_x} \Big|_{q_0} (\chi_M * \tilde{F})(q) &= \frac{\partial}{\partial q_x} \Big|_{q_0} \int_M \tilde{F}(q-p) dp \\
 &= \int_M \left( -\frac{\partial}{\partial p_x} \tilde{F}(q_0-p) \right) dp \\
 &= - \int_M \nabla \cdot (\tilde{F}(q_0-p), 0, 0) dp \\
 &= \int_{\partial M} \left\langle (\tilde{F}_p(q_0), 0, 0), \vec{N}_{\partial M}(p) \right\rangle dp.
 \end{aligned}$$

(The first equality follows from the fact that  $\chi_M$  is equal to zero outside of  $M$  and one inside. The second follows from the fact that  $(\partial/\partial q_x)\tilde{F}(q-p) = -(\partial/\partial p_x)\tilde{F}(q-p)$ . The last follows from the Divergence Theorem.)

A similar argument shows that the  $y$ , and  $z$ -components of the two sides are equal, thereby completing the proof.  $\square$

### 3.2.2 Approximating the gradient field

Of course, we cannot evaluate the surface integral since we do not yet know the surface geometry. However, the input set of oriented points provides precisely enough information to approximate the integral with a discrete summation. Specifically, using the point set  $P$  to partition  $\partial M$  into distinct patches  $\mathcal{P}_s \subset \partial M$ , we can approximate the integral over a patch  $\mathcal{P}_s$  by the value at point sample  $s.p$ ,

## CHAPTER 3. POISSON SURFACE RECONSTRUCTION

scaled by the area of the patch:

$$\begin{aligned} \nabla(\chi_M * \tilde{F})(q) &= \sum_{s \in P} \int_{\mathcal{P}_s} \tilde{F}_p(q) \vec{N}_{\partial M}(p) dp \\ &\approx \sum_{s \in P} |\mathcal{P}_s| \tilde{F}_{s,p}(q) \text{ s.n.} \equiv \vec{V}(q). \end{aligned} \tag{3.3}$$

It should be noted that although Equation 3.2 is true for any smoothing filter  $\tilde{F}$ , in practice, care must be taken in choosing the filter. In particular, we would like the filter to satisfy two conditions: (1) it should be sufficiently narrow so that we do not over-smooth the data; (2) it should be wide enough so that the integral over  $\mathcal{P}_s$  is well approximated by the value at  $s.p$  scaled by the patch area. A good choice of filter that balances these two requirements is a Gaussian whose variance is on the order of the sampling resolution.

### 3.2.3 Solving the Poisson problem

Having formed a vector field  $\vec{V}$ , we want to solve for the function  $\tilde{\chi}$  such that  $\nabla \tilde{\chi} = \vec{V}$ . However,  $\vec{V}$  is generally not integrable (i.e. it is not curl-free), so an exact solution does not generally exist. To find the least-squares solution, we apply the divergence operator to form the Poisson equation:

$$\Delta \tilde{\chi} = \nabla \cdot \vec{V} \tag{3.4}$$

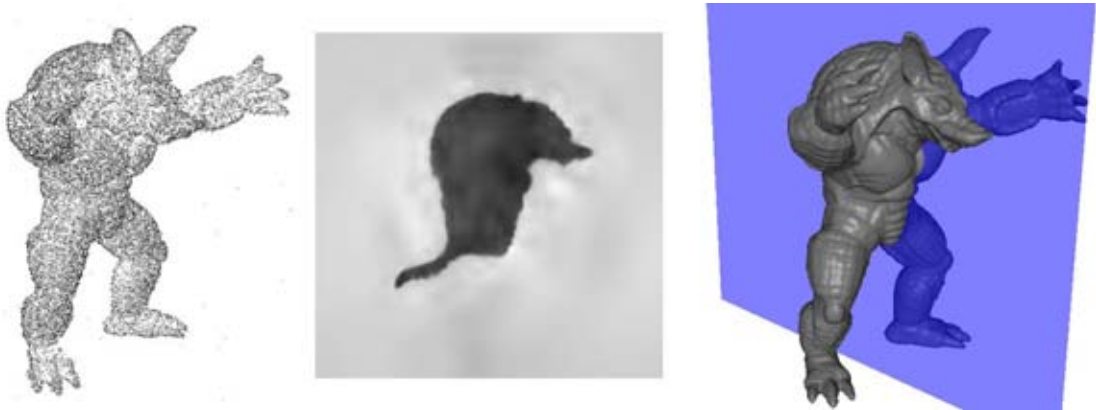


Figure 3.2: Points from scans of the “Armadillo Man” model (left), our Poisson surface reconstruction (right), and a visualization of the indicator function (middle) along a plane through the 3D volume.

### 3.3 Implementation

In this section, we describe our implementation of the Poisson surface reconstruction algorithm in more detail. We first present our algorithm under the assumption that the point samples are uniformly distributed over the model surface. We define a space of functions with high resolution near the surface of the model and coarser resolution away from it; we express the vector field  $\vec{V}$  as a linear sum of functions in this space; we set up and solve the Poisson equation; and we extract an iso-surface of the resulting indicator function. The extension of the algorithm to the case of non-uniformly sampled points is described in the next section.

### 3.3.1 Problem Discretization

First, we must choose the space of functions over which to discretize the problem. The most straightforward approach is to start with a regular 3D grid [31]. However, such a uniform structure becomes impractical for fine-detail reconstruction, since the dimension of the space is cubic in the resolution while the number of surface triangles grows quadratically.

Fortunately, an accurate representation of the implicit function is only necessary near the reconstructed surface. This motivates the use of an adaptive octree, both to represent the implicit function and to solve the Poisson system (e.g. [23, 38]). Specifically, we use the positions of the sample points to define an octree  $\mathcal{O}$  and associate a function  $F_o$  to each node  $o \in \mathcal{O}$  of the tree, choosing the tree and the functions so that the following conditions are satisfied:

1. The vector field  $\vec{V}$  can be precisely and efficiently represented as the linear sum of the  $F_o$ ;
2. The matrix representation of the Poisson equation, expressed in terms of the  $F_o$ , can be solved efficiently; and
3. A representation of the indicator function as the sum of the  $F_o$  can be precisely and efficiently evaluated near the surface of the model.

### 3.3.1.1 Defining the function space

Given a set of point samples  $P$  and a maximum tree depth  $D$ , we define the octree  $\mathcal{O}$  to be the minimal octree with the property that every point sample falls into a leaf node at depth  $D$ . Next, we define a space of functions obtained as the span of translates and scales of a fixed base function  $F : \mathbb{R}^3 \rightarrow \mathbb{R}$ . For every node  $o \in \mathcal{O}$ , we set  $F_o$  to be the “node basis function” centered about the node  $o$  and stretched by the size of  $o$ :

$$F_o(q) \equiv F\left(\frac{q - o.c}{o.w}\right) \quad (3.5)$$

where  $o.c$  and  $o.w$  are the center and width of node  $o$ .

This space of functions  $\mathcal{F}_{\mathcal{O},F} \equiv \text{Span}\{F_o\}$  has a multi-resolution structure: functions associated with finer nodes encode higher frequencies, and the function representation becomes more precise as we near the surface. Note that, because the space is adaptive, not all coarse functions can be represented as a linear combination of finer functions. Thus, the functions we will consider will be represented as linear combinations of nodal basis functions across all levels, not just the basis functions at the finest level.

### 3.3.1.2 Selecting a base function

In selecting a base function  $F$ , our goal is to choose a function so that the vector field  $\vec{V}$ , defined in Equation 3.3, can be precisely and efficiently represented as the linear sum of the node functions  $\{F_o\}$ .

Since a maximum tree depth of  $D$  corresponds to a sampling width of  $2^{-D}$ , the smoothing filter should approximate a Gaussian with variance on the order of  $2^{-D}$ . Thus,  $F$  should approximate a Gaussian with unit-variance.

For efficiency, we approximate the unit-variance Gaussian by a compactly supported function so that: (1) the resulting Divergence and Laplacian operators are sparse; and (2) the evaluation of a function expressed as the linear sum of  $F_o$  at some point  $q$  only requires summing over the nodes  $o \in \mathcal{O}$  that are close to  $q$ . Thus, we set  $F$  to be the  $n$ -th convolution of a box filter with itself resulting in the base function  $F$ :

$$F(x, y, z) \equiv (B(x)B(y)B(z))^{*n} \quad \text{with} \quad B(t) = \begin{cases} 1 & |t| < 0.5 \\ 0 & \text{otherwise} \end{cases} \quad (3.6)$$

Note that as  $n$  is increased,  $F$  more closely approximates a Gaussian and its support grows larger: in our implementation we use a piecewise quadratic approximation with  $n = 3$ . Therefore, the function  $F$  is supported on the domain  $[-1.5, 1.5]^3$  and, for the basis function of any octree node, there are at most  $5^3 - 1 = 124$  other nodes at the same depth whose functions have overlapping



support.

### 3.3.2 Vector Field Definition

If we were to replace the position of each sample with the center of the leaf node in which it falls, the vector field  $\vec{V}$  could be simply expressed as the linear sum of  $\{F_o\}$ . This way, each sample would contribute a single term (the normal vector) to the coefficient corresponding to its leaf's node function. Since the sampling width is  $2^{-D}$  and the samples all fall into leaf nodes of depth  $D$ , the error arising from the clamping can never be too big (at most, on the order of half the sampling width). To allow for sub-node precision, we avoid clamping a sample's position to the center of the containing leaf node and instead use interpolation to distribute the sample across the one ring neighborhood of nodes. In particular, we define our approximation to the gradient field of the indicator function as:

$$\vec{V}(q) = \sum_{o \in \mathcal{O}^D} F_o(q)v_o \quad (3.7)$$

with

$$v_o = \sum_{s \in P} F_o(s.p)s.n \quad (3.8)$$

where  $\mathcal{O}^D$  is the set of all nodes from the octree at depth  $D$ . Note that  $F_o(s.p)$  is only non-zero when  $o$  is in the one-ring neighborhood of the node containing  $s.p$ . Thus, in practice, the coefficients of the vector field can be computed by

“splatting” the normal vector  $s.n$  into the one-ring neighborhood of  $s.p$ . To ensure that we have an adequate ability to represent  $\vec{V}$  in this way, we construct the octree so that a node  $o$  is in the tree whenever there exists an  $s \in P$  such that  $F_o(s.p) \neq 0$ .

Since we assume that the samples are uniform, the area of a patch  $\mathcal{P}_s$  is constant and  $\vec{V}$  is a good approximation, up to a multiplicative constant, of the gradient of the smoothed indicator function. We will show that the choice of multiplicative constant does not affect the reconstruction.

### 3.3.3 Linear System Definition

Having defined the vector field  $\vec{V}$ , we would like to solve for the function  $\tilde{\chi} \in \mathcal{F}_{\mathcal{O},F}$  whose gradient is closest to  $\vec{V}$ : that is, we would like to solve the Poisson equation  $\Delta\tilde{\chi} = \nabla \cdot \vec{V}$ . One challenge of solving for  $\tilde{\chi}$  is that although  $\tilde{\chi}$  and the coordinate functions of  $\vec{V}$  are in the space  $\mathcal{F}_{\mathcal{O},F}$ , it is not necessarily the case that the functions  $\Delta\tilde{\chi}$  and  $\nabla \cdot \vec{V}$  are. To address this issue, we need to solve for the function  $\tilde{\chi}$  such that the projection of  $\Delta\tilde{\chi}$  onto the space  $\mathcal{F}_{\mathcal{O},F}$  is equals the projection of  $\nabla \cdot \vec{V}$ . Since, in general, the functions  $F_o$  do not form an orthonormal basis, solving this problem directly is expensive. However, we can simplify the problem using the Galerkin formulation by solving for the function  $\tilde{\chi}$

### CHAPTER 3. POISSON SURFACE RECONSTRUCTION

with:

$$\langle \Delta \tilde{\chi}, F_o \rangle = \langle \nabla \cdot \vec{V}, F_o \rangle \quad (3.9)$$

for all  $o \in \mathcal{O}$ . Thus given the  $|\mathcal{O}|$ -dimensional vector  $b$  whose  $o$ -th coordinate is  $b_o = \langle \nabla \cdot \vec{V}, F_o \rangle$ , the goal is to solve for the function  $\tilde{\chi}$  such that the vector obtained by taking the dot product of the Laplacian of  $\tilde{\chi}$  with each of the  $F_o$  is equal to  $b$ .

To express this in matrix form, we let  $\tilde{\chi} = \sum_o x_o F_o$ , so that we are solving for the vector  $x \in \mathbb{R}^{|\mathcal{O}|}$ . Then, we define the  $|\mathcal{O}| \times |\mathcal{O}|$  matrix  $L$  so that  $Lx$  returns the dot product of the Laplacian with each of the  $F_o$ . Specifically, for all  $o, o' \in \mathcal{O}$ , the  $(o, o')$ -th entry of  $L$  is set to:

$$L_{o,o'} \equiv \left\langle \frac{\partial^2 F_o}{\partial x^2}, F_{o'} \right\rangle + \left\langle \frac{\partial^2 F_o}{\partial y^2}, F_{o'} \right\rangle + \left\langle \frac{\partial^2 F_o}{\partial z^2}, F_{o'} \right\rangle. \quad (3.10)$$

Thus, solving for  $\tilde{\chi}$  amounts to finding

$$Lx = b \quad (3.11)$$

Note that in solving for  $\tilde{\chi}$ , we do not explicitly compute the projection of the divergence of  $\vec{V}$  onto  $\mathcal{F}_{\mathcal{O},F}$ . We only compute the dot product of the divergence with each  $F_o$ . Since the  $F_o$  are compactly supported, this can be done efficiently.

## CHAPTER 3. POISSON SURFACE RECONSTRUCTION

Note also that the matrix  $L$  is sparse and symmetric. (Sparse because the  $F_o$  are compactly supported, and symmetric because  $\int f''g = -\int f'g'$ .)

Furthermore, there is an inherent multiresolution structure on  $\mathcal{F}_{\mathcal{O},F}$ , so we use a multigrid approach. The linear system  $Lx = b$  is transformed into successive linear systems  $L^d x^d = b^d$  (solved using conjugate gradients), one per octree depth  $d$ . The solutions at finer depths only consider the residual divergence not accounted for at coarser depths. More precisely, after solving at depths  $d' < d$ , the divergence constraints are updated at depth  $d$  to subtract those components of the constraints that have already been satisfied at the coarser resolutions:

$$b_o^d \leftarrow b_o^d - \sum_{d' < d} \sum_{o' \in \mathcal{O}^{d'}} L_{o,o'} x_{o'}, \quad (3.12)$$

where  $\mathcal{O}^d$  denotes the set of octree nodes at depth  $d$ . Note that this approach means that we use a cascadic multigrid solver (i.e. we do not restrict finer solutions back to coarser solutions).

### 3.3.4 Iso-Surface Extraction

In order to obtain a reconstructed surface  $\partial\tilde{M}$ , it is necessary first to select an iso-value and then to extract the corresponding iso-surface from the computed indicator function.

We choose the iso-value so that the extracted surface closely approximates the

## CHAPTER 3. POISSON SURFACE RECONSTRUCTION

positions of the input samples. We do this by evaluating  $\tilde{\chi}$  at the sample positions, and use the average of the values for iso-surface extraction:

$$\partial\tilde{M} \equiv \{q \in \mathbb{R}^3 \mid \tilde{\chi}(q) = \gamma\} \quad \text{with} \quad \gamma = \frac{1}{|S|} \sum_{s \in P} \tilde{\chi}(s.p). \quad (3.13)$$

This choice of iso-value has the property that scaling  $\tilde{\chi}$  does not change the iso-surface. Thus, knowing the vector field  $\vec{V}$  up to a multiplicative constant provides sufficient information for reconstructing the surface.

To extract the iso-surface from the indicator function, we use the method of [32] which is similar to previous adaptations of the Marching Cubes [37] to an octree representation (e.g. [47, 54, 55]), but supports non-conforming trees, preventing cracks from arising when coarser nodes share a face with finer ones.

### 3.3.5 Non-uniform Samples

We now describe the extension of our method to the case of non-uniformly distributed point samples. As in [31], our approach is to estimate the local sampling density, and scale the contribution of each point accordingly. However, rather than simply scaling the *magnitude* of a *fixed*-width kernel associated with each point, we additionally adapt the kernel width. This results in a reconstruction that maintains sharp features in areas of dense sampling and provides a smooth fit in sparsely sampled regions. Figure 3.3 illustrates the problems associated with

## CHAPTER 3. POISSON SURFACE RECONSTRUCTION

using a fixed-width kernel to perform sample density estimation. In (b) and (c), we can see the reconstructions of the cow using a low and high resolutions (i.e. wider and narrower kernels) respectively. Because of the highly non-uniform nature of the input point set, the use of a fixed-width kernel cannot simultaneously produce a good estimation of sample density in all regions, and one must choose between accurately capturing sharp features (such as the head) or smoothly reconstructing the sparsely sampled body. In contrast, the use of adaptive width density kernels, illustrated in (d), allows both regions to be reconstructed accurately by adapting the filter width to the sampling density.

### 3.3.5.1 Estimating local sampling density

Following the approach of [31], we implement the density computation using a kernel density estimator [45]. The approach is to estimate the number of points in a neighborhood of a sample by “splatting” the samples into a 3D grid, convolving the “splatting” function with a smoothing filter, and evaluating the convolution at each of the sample points.

We implement the convolution in a manner similar to Equation 3.7. For each depth  $\hat{D} \leq D$  we compute a density estimator as the sum of node functions at depth  $\hat{D}$ :

$$W_{\hat{D}}(q) = \sum_{o \in \mathcal{O}^{\hat{D}}} F_o(q) k_o \quad (3.14)$$

## CHAPTER 3. POISSON SURFACE RECONSTRUCTION

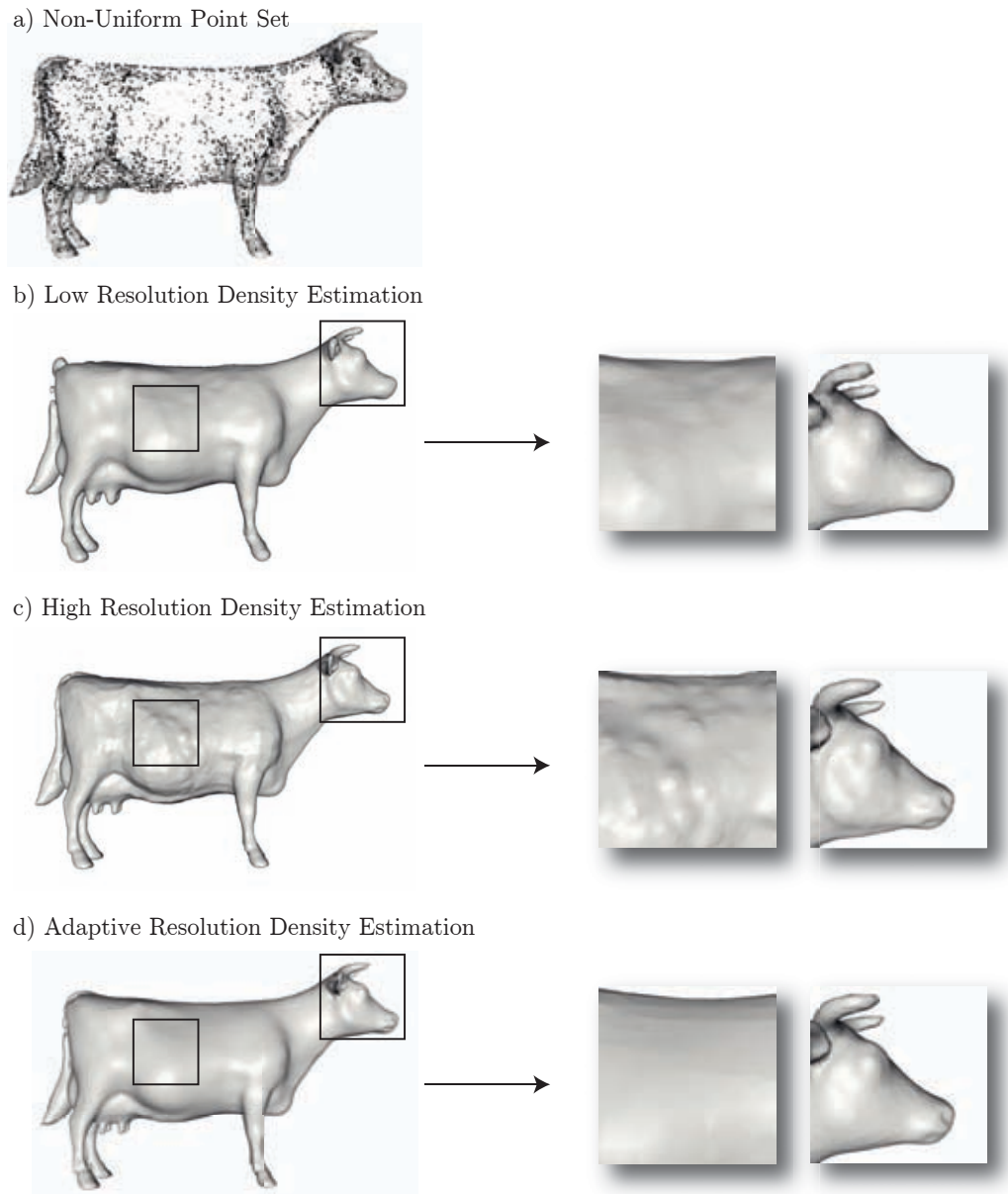


Figure 3.3: A comparison of the reconstruction of a highly non-uniform dataset using a low resolution (b), high resolution (c) and adaptive resolution sample density estimation (d).

with

$$k_o = \sum_{s \in P} F_o(s.p) \quad (3.15)$$

Since octree nodes at lower resolution are associated with functions that approximate Gaussians of larger width, computing  $W_{\hat{D}}$  at each level in the tree provides a way to estimate sampling density over a wide range of widths. Furthermore, because the basis functions at depth  $\hat{D}$  form a partition of unity, the weight  $W_{\hat{D}}(q)$  can be viewed as a (local) measure of the number of samples falling into a node at depth  $\hat{D}$ .

### 3.3.5.2 Estimating a samples depth

Given a user-supplied parameter  $\kappa$ , which determines the number of input samples that should fall into an octree node, we determine the fractional depth  $\text{Depth}(s.p)$  to represent the depth at which a sample point  $s \in P$  should be splatted. Specifically, we find the finest level of the tree  $D_{splat}$  at which the sampling density  $W_{D_{splat}}(s.p)$  is greater than  $\kappa$ , and set:

$$\text{Depth}(s.p) \equiv \min \left( D, D_{splat} + \frac{\log\left(\frac{W_{D_{splat}}(s.p)}{\kappa}\right)}{\log\left(\frac{W_{D_{splat}}(s.p)}{W_{D_{splat}+1}(s.p)}\right)} \right) \quad (3.16)$$

### 3.3.5.3 Computing the vector field

Using the density estimator at the splatting depth, we modify the summation in Equation 3.7 so that each sample's contribution is proportional to its associated



### CHAPTER 3. POISSON SURFACE RECONSTRUCTION

area on the surface ( $4^{\text{Depth}(s.p)}$ ). However, adapting only the magnitudes of the sample contributions results in poor noise filtering in sparsely sampled regions as, shown in Figure 3.7. Therefore, we also adapt the width of the smoothing filter  $\tilde{F}$  to the local sampling density. Adapting the filter width allows us to retain fine detail in regions of dense sampling, while smoothing out noise in regions of sparse sampling.

To do this, we adapt the depth of the basis function with which we splat in a normal to the local sampling density. For points in regions of low sampling density, we splat the associated normals in with node functions from coarser nodes (which have wider support); for points in regions of high sampling density we use the functions from finer nodes. Using a sample's fractional depth value,  $\text{Depth}(s.p)$ , we define  $\delta = \text{Depth}(s.p) - \lfloor \text{Depth}(s.p) \rfloor$  and splat the sample normal into depths  $D_1 = \lfloor \text{Depth}(s.p) \rfloor$  and  $D_2 = \lceil \text{Depth}(s.p) \rceil$  using linear interpolation. Specifically, we define:

$$\vec{V}(q) \equiv \sum_{s \in P} \left[ \frac{(1 - \delta)8^{D_1}}{4^{\text{Depth}(s.p)}} \sum_{o \in \mathcal{N}_{D_1}^1(s.p)(s)} \alpha_{o,s} F_o(q) s.n \right. \\ \left. + \frac{\delta 8^{D_2}}{4^{\text{Depth}(s.p)}} \sum_{o \in \mathcal{N}_{D_2}^1(s.p)(s)} \alpha_{o,s} F_o(q) s.n \right] \quad (3.17)$$

so that the width of the smoothing filter with which  $s$  contributes to  $\vec{V}$  is

proportional to the radius of its associated surface patch  $P_s$ .

### 3.3.6 Selecting an iso-value

Finally, we modify the surface extraction step by selecting an iso-value that is the weighted average of the values of  $\tilde{\chi}$  at the sample positions:

$$\partial\tilde{M} \equiv \{q \in \mathbb{R}^3 \mid \tilde{\chi}(q) = \gamma\} \quad \text{with} \quad \gamma = \frac{\sum \frac{1}{W_{D_{splat}}(s,p)} \tilde{\chi}(s,p)}{\sum \frac{1}{W_{D_{splat}}(s,p)}}. \quad (3.18)$$

We weight the iso-value contribution of a point by the reciprocal of a samples estimated surface patch area so that the final iso-surface more closely matches samples from areas of high sampling density.

## 3.4 Results

To evaluate our method, we conducted a series of experiments. Our goal was to address three separate questions: How well does the algorithm reconstruct surfaces? How does it compare to other reconstruction methods? And, what are its performance characteristics?

Much practical motivation for surface reconstruction derives from 3D scanning, so with the exception of the first experiments, we have focused our experiments

on the reconstruction of 3D models from real-world data.

### 3.4.1 Resilience to Noise

One of the advantages of using a global system like the Poisson equation is its robustness to noise. To evaluate the effect that sampling noise has on our method, we created a 200,000 point dataset by sampling the surface of the “Armadillo Man” model and adding varying degrees of random noise to both the position and normal of samples. For positional noise, we added a random displacement of a fixed length,  $\delta$ , to each of the samples. For normal noise, we randomly changed the orientation of the normal by a fixed angle  $\theta$ . Figure 3.4 presents a grid of the reconstruction result obtained on sixteen datasets with different combinations of  $\delta$  (in rows) and  $\theta$  (in columns). We express  $\delta$  as a proportion of the radius of the bounding sphere of the model  $r$ , and  $\theta$  as degrees. Note that the reconstruction depth is 9, so the finest nodes are approximately  $\frac{r}{512}$  in size.

When adding positional noise, we can see that the finer features such as the patterns on the arms and legs are still well preserved when  $\delta = \frac{r}{256}$ . Fine features are lost when  $\delta = \frac{r}{64}$ , and at  $\delta = \frac{r}{16}$  the ears, fingers and tail are not reconstructed correctly. From the columns of Figure 3.4, we can see that our method is remarkably stable in the presence of normal noise. When  $\theta = 30$ , there are no significant artifacts on the reconstructions. As  $\theta$  increases further, a rippling can be observed across the surfaces, and when combined with large

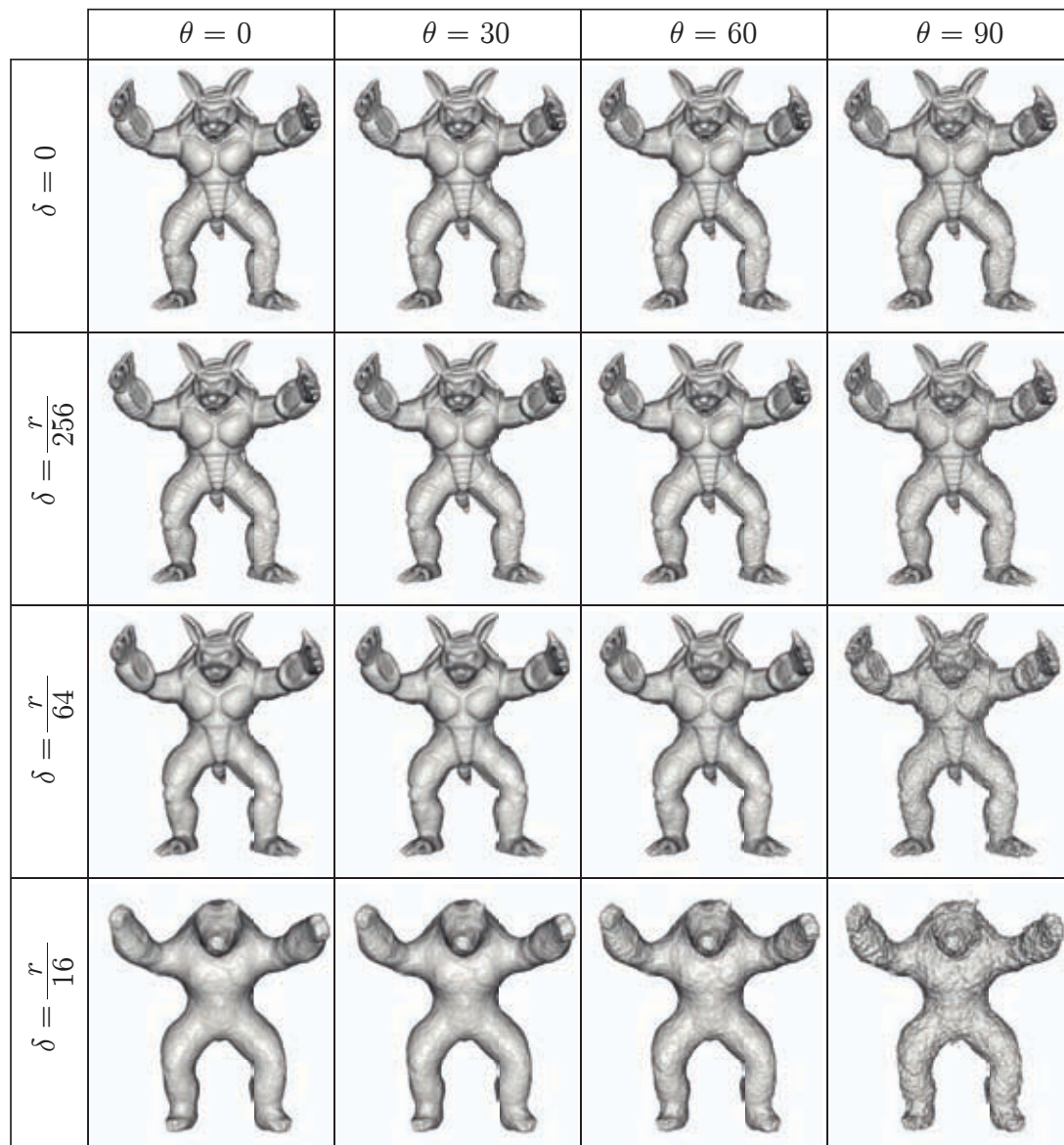


Figure 3.4: Reconstructions of an 200,000 point sampling of the “Armadillo Man” model at depth 9 with varying amounts of random noise introduced to the position ( $\delta$ ) and normal ( $\theta$ ) component to the samples.  $r$  is the radius of the models bounding sphere.

amounts of positional noise, parts of the model begin to disconnect (e.g. the ears and tail).

In addition to being robust to synthetic noise, the results in the rest of this chapter also highlight our method’s ability to perform well with the types of noise and other anomalies found in real-world scan data.

### 3.4.2 Comparison to Previous Work

In order to provide a context for evaluating the performance and reconstruction abilities of our method, we compare the results of our algorithm to the results obtained using Power Crust [4], Robust Cocone [18], Fast Radial Basis Functions (FastRBF) [13], Multi-Level Partition of Unity Implicits (MPU) [43], Surface Reconstruction from Unorganized Points [25], Volumetric Range Image Processing (VRIP) [17], the Wavelet-based method of [39], and the FFT-based method of [31].

Our initial test case is the Stanford Bunny raw dataset of 362,000 points assembled from ten range images. The data was processed to fit the input format of each algorithm. For example, when running our method, we estimated a sample’s normal from the positions of its neighbors. Running VRIP, we used the registered scans as input, maintaining the regularity of the sampling, and providing the confidence values.

Figure 3.5 compares the different reconstructions. Since the scanned data contains noise, interpolatory methods such as Power Crust (a) and Robust Cocone

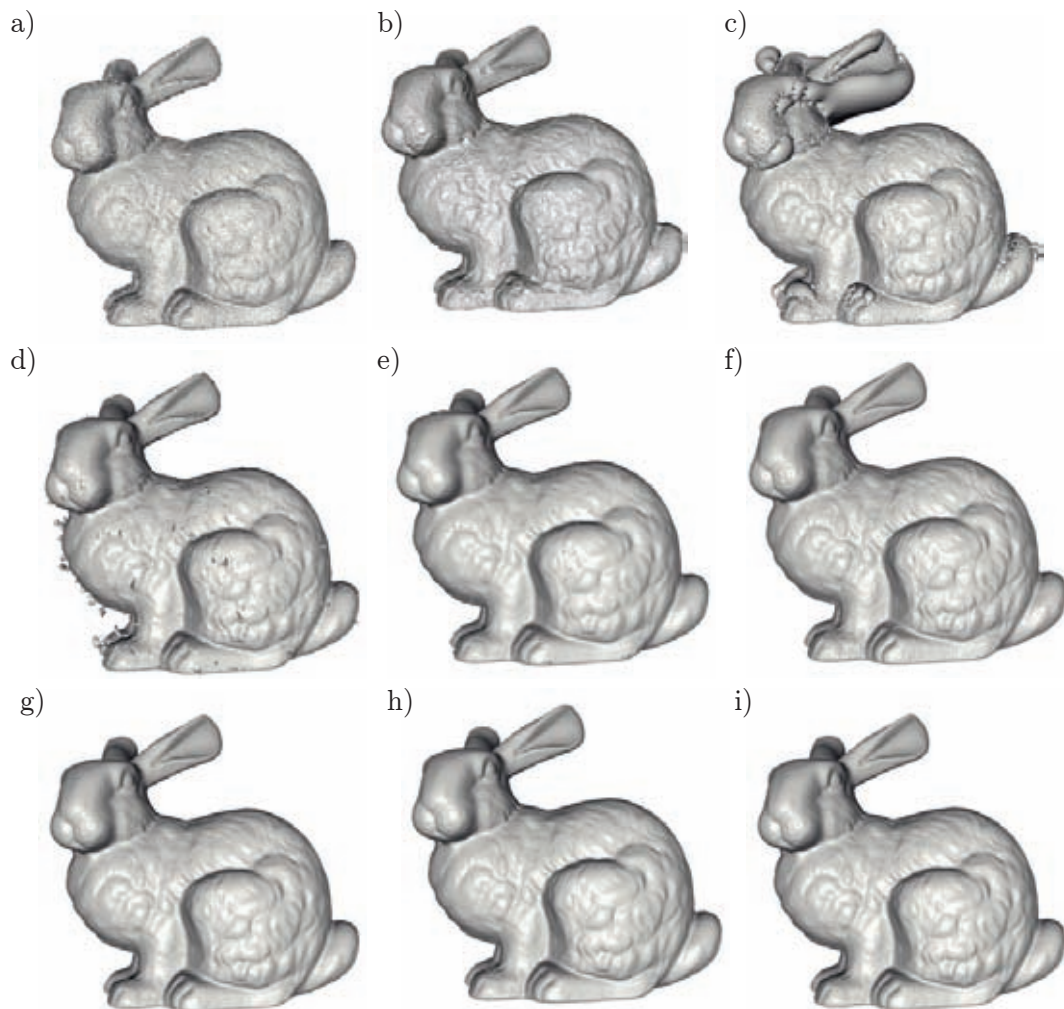


Figure 3.5: Reconstructions of the Stanford Bunny using Power Crust (a), Robust Cocone (b), Fast RBF (c), MPU (d), Hoppe *et al.*'s reconstruction (e), Wavelet-based reconstruction (f), FFT-based reconstruction (g), VRIP (h), and our Poisson reconstruction (i).

(b) generate surfaces that are themselves noisy. Methods such as Fast RBF (c) and MPU (d), which only constrain the implicit function near the sample points, result in reconstructions with spurious surface sheets. Non-interpolatory methods, such as the approach of Hoppe *et al.* [25] (e), can smooth out the noise, although often at the cost of model detail. The FFT-based approach (g), VRIP (h), and our approach (i) all accurately reconstruct the surface of the bunny, even in the presence of noise. We compare these three methods in more detail below.

### 3.4.2.1 Comparison to Wavelet-based approach

The Wavelet-based approach of Manson *et al.* [39] takes an approach similar to ours in solving the reconstruction problem. Both methods reconstruct surfaces using an implicit function fitting approach where the choice of implicit function is the indicator function. The methods differ in how the indicator function is constructed. The Wavelet method represents the indicator function using a wavelet-based function space, and is able to compute the wavelet coefficients directly from the input samples. Our approach constructs and solves a sparse linear system to compute the indicator function.

Figure 3.6 compares our method to the Wavelet-based approach. Although apparently reconstructing more fine detail than our method, the wavelet reconstruction also has axis-aligned contouring effects, which are especially noticeable when the reconstructed surface is almost parallel to the grid axes (e.g.

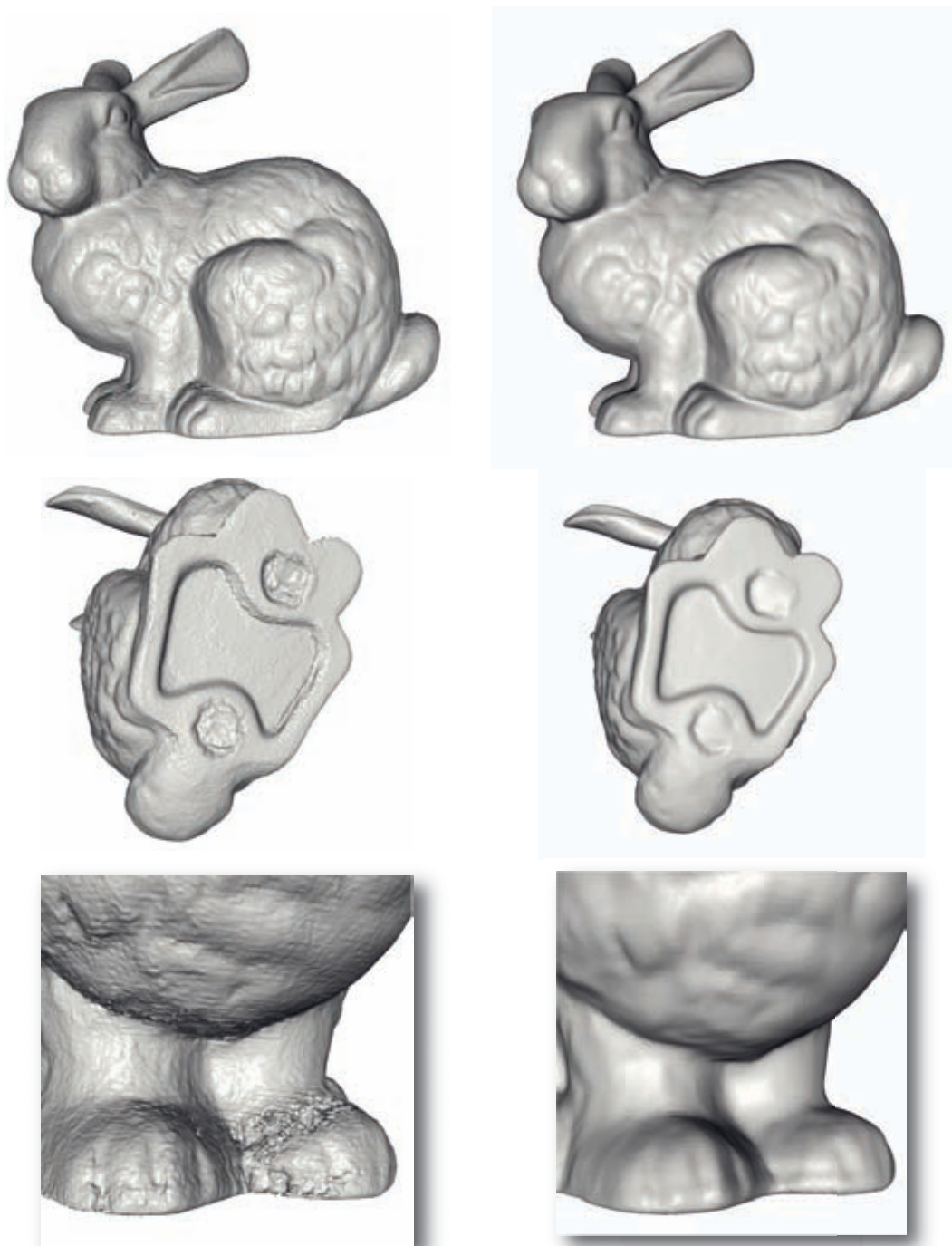


Figure 3.6: Several views of the reconstruction of the Stanford Bunny model using the Wavelet technique (using the D4 basis function) and our method



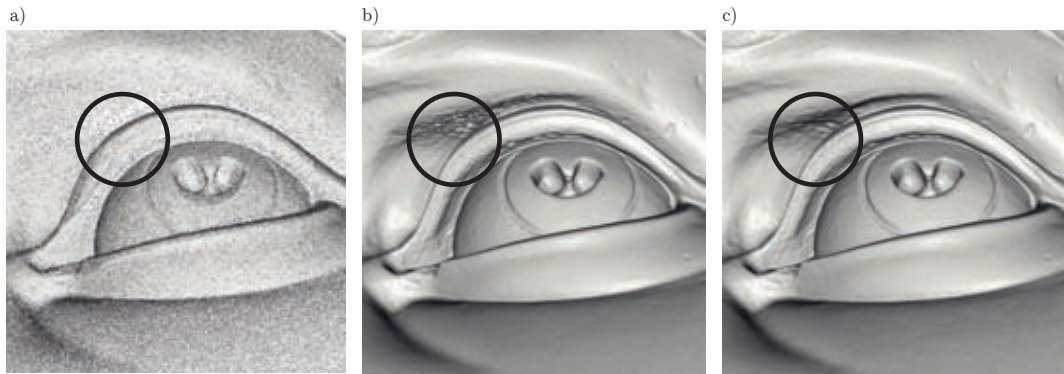


Figure 3.7: Reconstruction of samples from the region around the left eye of the David model (a), using the fixed-resolution FFT approach (b), and Poisson reconstruction (c).

on the tops of the feet and the bottom of the model). Another situation where the Wavelet method performs poorly is when the input data is highly non-uniform and contains holes. This is particularly noticeable in the third comparison, showing the Bunny’s feet. In this case, the wavelet method generates a highly irregular surface containing disconnected surfaces, tunnels, and loops. Our Poisson method, although smoother, reconstructs a surface with no unexpected topological changes.

### 3.4.2.2 Comparison to the FFT-based approach

As Figure 3.5 demonstrates, our Poisson reconstruction (i) closely matches the one obtained with the FFT-based method (g). Since our method provides an adaptive solution to the same problem, the similarity confirms that, in adapting the octree to the data, our method does not discard salient, high-frequency information.

## CHAPTER 3. POISSON SURFACE RECONSTRUCTION

Although theoretically equivalent in the context of uniformly sampled data, our use of adaptive-width filters (Section 3.3.5) gives better reconstructions than the FFT-based method when reconstructing the non-uniform data commonly encountered in 3D scanning. As an example, we consider the region around the left eye of the David model, shown in Figure 3.7(a). The area above the eyelid (circled in black) is sparsely sampled because it is in a concave region and is seen only by a few scans. Furthermore, the scans that do sample the region tend to sample at near-grazing angles resulting in noisy position and normal estimates. Consequently, fixed-resolution reconstruction schemes such as the FFT-based approach (b) introduce aliasing artifacts in these regions. In contrast, our method (c), which adapts both the scale and the variance of the samples’ contributions, fits a smoother reconstruction to these regions without sacrificing fidelity in areas of dense sampling.

### 3.4.2.3 Comparison to VRIP

A challenge in surface reconstruction is the recovery of sharp features. We compared our method to VRIP by evaluating the reconstruction of sample points obtained from fragment 661a of the *Forma Urbis Romae* (30 scans, 2,470,000 points) and the Happy Buddha model (48 scans, 2,468,000 points) shown in Figures 3.8 and 3.9. In both cases, we find that VRIP exhibits a “lipping” phenomenon at sharp creases. This is due to the fact that VRIP’s distance

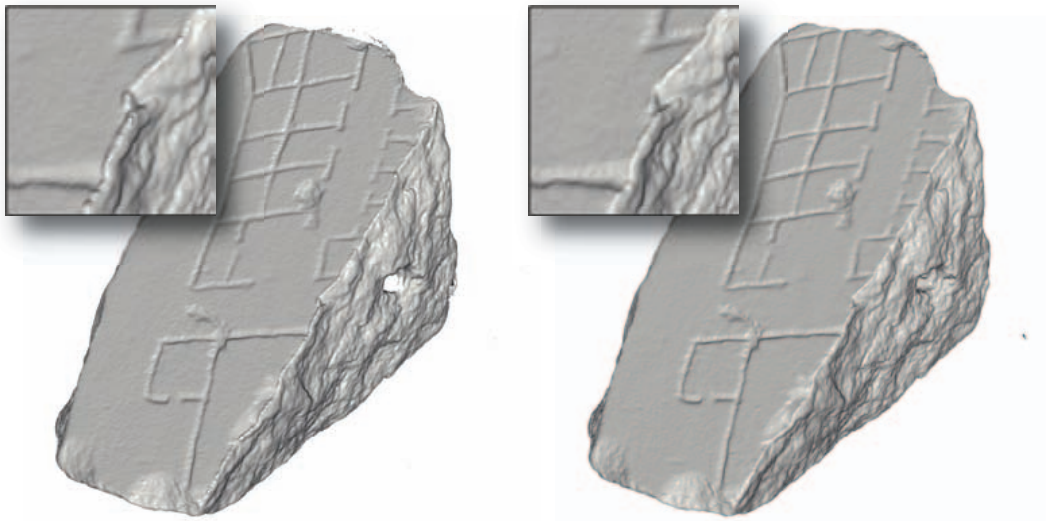


Figure 3.8: Reconstructions of a fragment of the Forma Urbis Romae tablet using VRIP (left) and the Poisson solution (right).

function is grown perpendicular to the view direction, not the surface normal. In contrast, our Poisson reconstruction, which is independent of view direction, accurately reconstructs the corner of the fragment and the sharp creases in the Buddha's cloak.

#### 3.4.2.4 Limitation of our approach

A limitation of our method is that it does not incorporate information associated with the acquisition modality. Figure 3.9 shows an example of this in the reconstruction at the base of the Buddha. Since there are no samples between the two feet, our method (right) connects the two regions. In contrast, the ability to use secondary information like line of sight allows VRIP (left) to



Figure 3.9: Reconstructions of the “Happy Buddha” model using VRIP (left) and Poisson reconstruction (right). Although our method generates a more accurate reconstruction of the sharp features, its independence of acquisition modality makes it incapable of leveraging line-of-sight information to carve out the space between the legs.

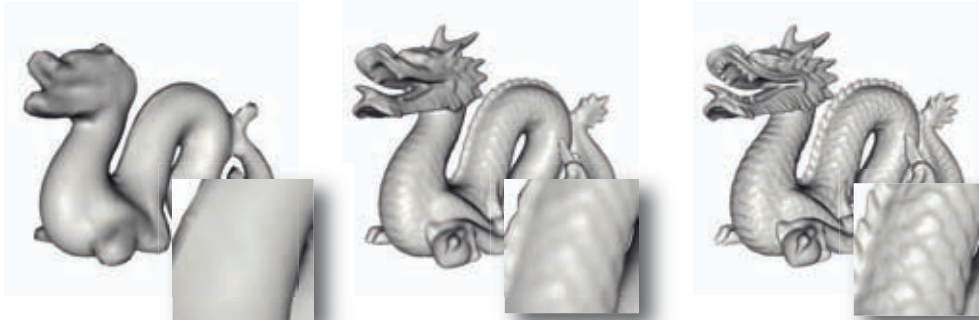


Figure 3.10: Reconstructions of the Dragon model at octree depths 6 (left), 8 (middle), and 10 (right).

perform the space carving necessary to disconnect the two feet, resulting in a more accurate reconstruction.

### 3.4.3 Performance and Scalability

Table 3.1 summarizes the temporal and spatial efficiency of our algorithm on the “Dragon” model, and images of the reconstructions at depths 6, 8, and 10 are presented in Figure 3.10. The numerical results indicate that the memory and time requirements of our algorithm are roughly quadratic in the resolution. Thus, as we increase the octree depth by one, we find that the running time, the memory overhead, and the number of output triangles increases roughly by a factor of four.

The running time and memory performance of our method in reconstructing the Stanford Bunny at a depth of 9 is compared to the performance of related methods in Table 3.2. Although in this experiment, our method is neither the

## CHAPTER 3. POISSON SURFACE RECONSTRUCTION

Tree Depth	Time (s)	Peak Memory (MB)	Number of Triangles
6	3	7	4,883
7	6	19	21,000
8	26	75	90,244
9	126	155	374,868
10	633	699	1,516,806

Table 3.1: The running time (in seconds), the peak memory usage (in megabytes), and the number of triangles in the reconstructed model for the different depth reconstructions of the Dragon model. A kernel depth of 6 was used for density estimation.

fastest nor the most memory efficient, its quadratic nature makes it scalable to higher resolution reconstructions. As an example, Figure 3.11 shows a reconstruction of the head of Michelangelo’s David at a depth of 11 from a set of 215,613,477 samples. The reconstruction was computed in 1.9 hours and required 5.2GB of RAM, generating a 16,328,329 triangle model. Trying to compute an equivalent reconstruction with methods such as the FFT approach would require constructing two voxel grids at a resolution of  $2048^3$  and would require in excess of 100GB of memory.

### CHAPTER 3. POISSON SURFACE RECONSTRUCTION

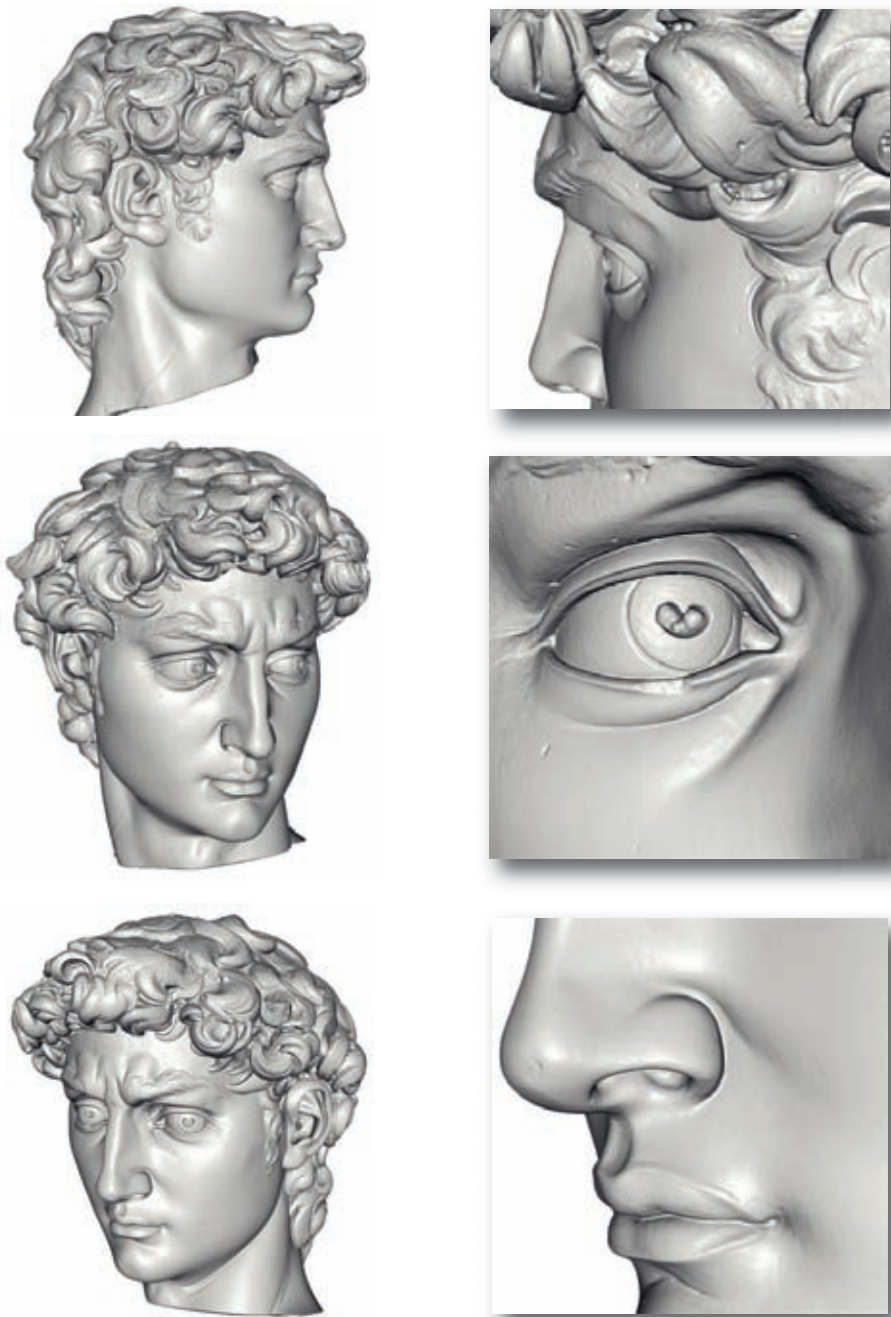


Figure 3.11: Several images of the reconstruction of the head of Michelangelo's David, obtained running our algorithm with a maximum tree depth of 11. The ability to reconstruct the head at such a high resolution allows us to make out the fine features in the model such as the inset iris, the drill marks in the hair, the chip on the eyelid, and the creases around the nose and mouth.

## CHAPTER 3. POISSON SURFACE RECONSTRUCTION

Method	Time (s)	Peak Memory (MB)	Number of Triangles
Power Crust	380	2653	554,332
Robust Cocone	892	544	272,662
FastRBF	4919	796	1,798,154
MPU	28	260	925,240
Hoppe <i>et al.</i>	70	330	950,562
VRIP	86	186	1,038,055
Wavelets (D4)	82	280	1,086,234
FFT	125	1684	910,320
Poisson	263	310	911,390

Table 3.2: The running time (in seconds), the peak memory usage (in megabytes), and the number of triangles in the reconstructed surface of the Stanford Bunny generated by the different methods.



# Chapter 4

## Streaming Surface

### Reconstruction

In Chapter 3, we demonstrated that surface reconstruction from oriented points can be made more resilient to data errors by casting the problem as a global Poisson system. Intuitively, the idea is to interpret the oriented points as samples of the gradient of the model's indicator function  $\chi$  (defined as 1 at points inside the model, and 0 at points outside). Thus, the desired indicator function is the one whose Laplacian equals the divergence of a vector field  $\vec{V}$  constructed from the oriented points:  $\Delta\chi = \nabla \cdot \vec{V}$ . By representing  $\chi$  using a basis defined over an adaptive octree, the Poisson equation is discretized into a sparse linear system  $Lx = b$  where the size of the system is proportional to the complexity of the reconstructed surface. Then, the desired model is extracted as an iso-surface

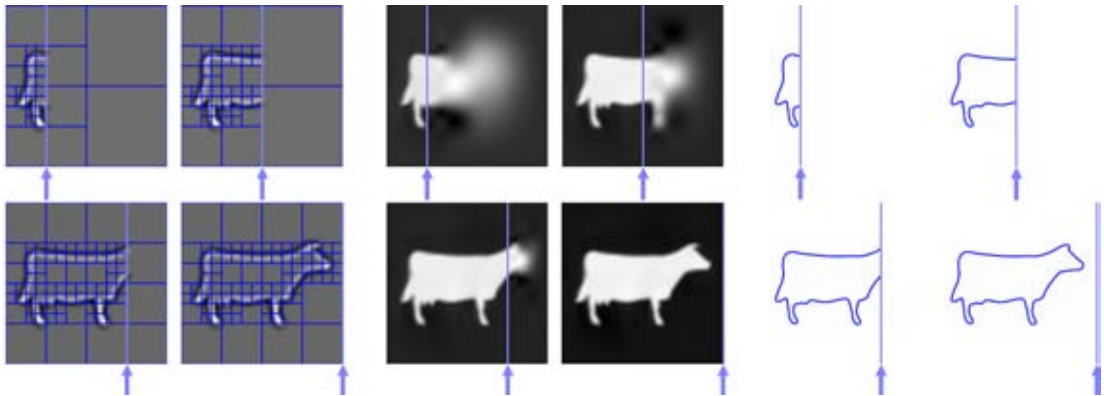


Figure 4.1: Example of curve reconstruction in 2D as a sequence of three multilevel streaming passes over an adaptive quadtree.

of the resulting indicator field.

The fact that Poisson reconstruction has global support would seem to preclude an easy out-of-core solution, making it challenging to apply the technique to some of the larger point sets returned by recent scanning technologies. Indeed, for very large models, not only is the matrix  $L$  too large to fit in memory, but the vectors  $b$  and  $x$  are also too large. In this chapter, we will show that the reconstruction process can be implemented efficiently as a sequence of *streaming* operations, performed in three passes over out-of-core data. These operations include the creation of the linear system, its solution, and the final iso-surface extraction. The 2D example in Figure 4.1 helps to illustrate this streaming process. In this example, we show four moments in time for each of the three streaming passes being used to reconstruct the cow. The octree and linear system are constructed (left), the linear system is solved (middle), and the surface extracted (right) as a plane sweeps through the reconstruction domain in each pass.

## CHAPTER 4. STREAMING SURFACE RECONSTRUCTION

In general, a streaming approach is advantageous because data is accessed sequentially from disk, and it is only loaded once. Sequential access is typically more efficient because it allows for data prefetching. In computer graphics, streaming computation has been performed over many data types including triangle meshes, point sets and tetrahedral meshes, as reviewed in Section 4.1.

A unique aspect of our problem is the requirement for an adaptive multiresolution structure, namely an octree, because a solution over a uniform 3D grid is not scalable [31]. Interestingly, the operations performed on the octree have different types of inter-level data dependencies and, consequently, no single linear ordering of the octree nodes is adequate. To overcome these dependencies, we introduce a *multilevel streaming* representation in which each level is stored as a separate stream. A processing pass sweeps over the octree by concurrently advancing through the multiple streams, iterating at a faster rate through the finer nodes than the coarser ones. Depending on the operation, information flows up and/or down the tree, and computations on coarser levels precede or succeed those on finer levels.

A surprising result is that we are able to solve the sparse Poisson system  $Lx = b$  with sufficient accuracy for our reconstruction application in only two multi-stream passes through the data; one pass to compute the divergence, and a second pass to solve the linear system. We are able to do this in two passes through the data because clever scheduling of the computation across levels lets us

realize a multigrid scheme using Gauss-Seidel updates [11], enabling sufficiently accurate convergence using only local updates.

Using this method, we are able to obtain reconstructions of highly complex models (210 million triangles) on a PC with only 1 GB of memory, and demonstrate scalable performance.

## 4.1 Related Work

### 4.1.1 Out-of-core Surface Reconstruction

Several surface reconstruction algorithms lend themselves naturally to out-of-core computation because their access patterns are highly localized. For instance, the range-image volumetric merging scheme of Curless and Levoy [17] can easily be computed independently on blocks of the domain space. For each block, one conservatively finds the scanned points that can contribute to it. Schemes based on local neighborhood fitting such as [3, 25] could also be computed in a streaming traversal, for instance using the scheme of Pajarola [44]. The multilevel partition of unity (MPU) approach of [43] uses an adaptive octree structure to blend together estimated implicit surface patches. Its use of local weights should make it amenable to out-of-core processing. The ball-pivoting algorithm of [8] is implemented out-of-core by partitioning the domain into slices.

Our work is the first to present an out-of-core implementation of a *global*

surface reconstruction technique.

### 4.1.2 Stream Processing

Much of the streaming work in computer graphics focuses on irregular triangle meshes [2, 6, 27, 29, 56]. Streaming operations include surface smoothing, mesh simplification, remeshing, and normal estimation. Streaming has also been applied to irregular tetrahedral mesh compression [30] and simplification [53]. Pajarola [44] describes stream processing on points. His streaming scheme is able to find the  $k$ -closest neighborhoods of the points, to enable processing operations such as density computation, normal estimation, and geometric smoothing. Isenburg *et al.* [28] stream through a set of points to incrementally construct a Delaunay triangulation. Whereas prior streaming methods operate at a single resolution on the data, we introduce a multiresolution streaming framework.

### 4.1.3 Other Out-of-core Processing

Cignoni *et al.* [16] introduce an octree-based external memory structure to store an irregular mesh out-of-core. They describe how to handle triangles that span octree cell boundaries. Processing a subtree involves loading its adjacent leaf-nodes into memory. Maintaining random access to the octree nodes is beneficial for view-dependent rendering, as also shown in [36].

### 4.1.4 Out-of-core Linear Solvers

Toledo [52] provides a nice survey of methods for solving linear systems out-of-core. For sparse systems, most modern methods assume that the system matrix itself can fit in memory. A common approach is to construct a Cholesky factorization out-of-core (e.g. [22]). In our problem, even the solution vector itself is too large to lie in-core. We must therefore resort to simple iterative updates. However, we show that doing so in a cascadic multigrid setting, with a per-block Gauss-Seidel scheme, is sufficient to produce adequate accuracy for surface reconstruction in a single multi-stream pass.

## 4.2 Representation

In this work, we show that Poisson surface reconstruction can be performed as a sequence of streaming passes over an out-of-core octree representation.

Each streaming pass traverses the octree, sweeping along the  $x$  axis. For an octree of height  $D+1$ , each traversal step is associated with a sweep index  $0 \leq i < 2^D$  defining the sweep plane  $x = (2i+1)/2^D$ . Because streaming computations are local, only the subset of the octree intersecting with or near to the sweep plane needs to be maintained in main memory. Thus, as we advance to sweep index  $i+1$ , nodes at the back of the tree (with smaller  $x$  coordinates) can be removed from memory, while nodes at the front of the tree need to be loaded in.

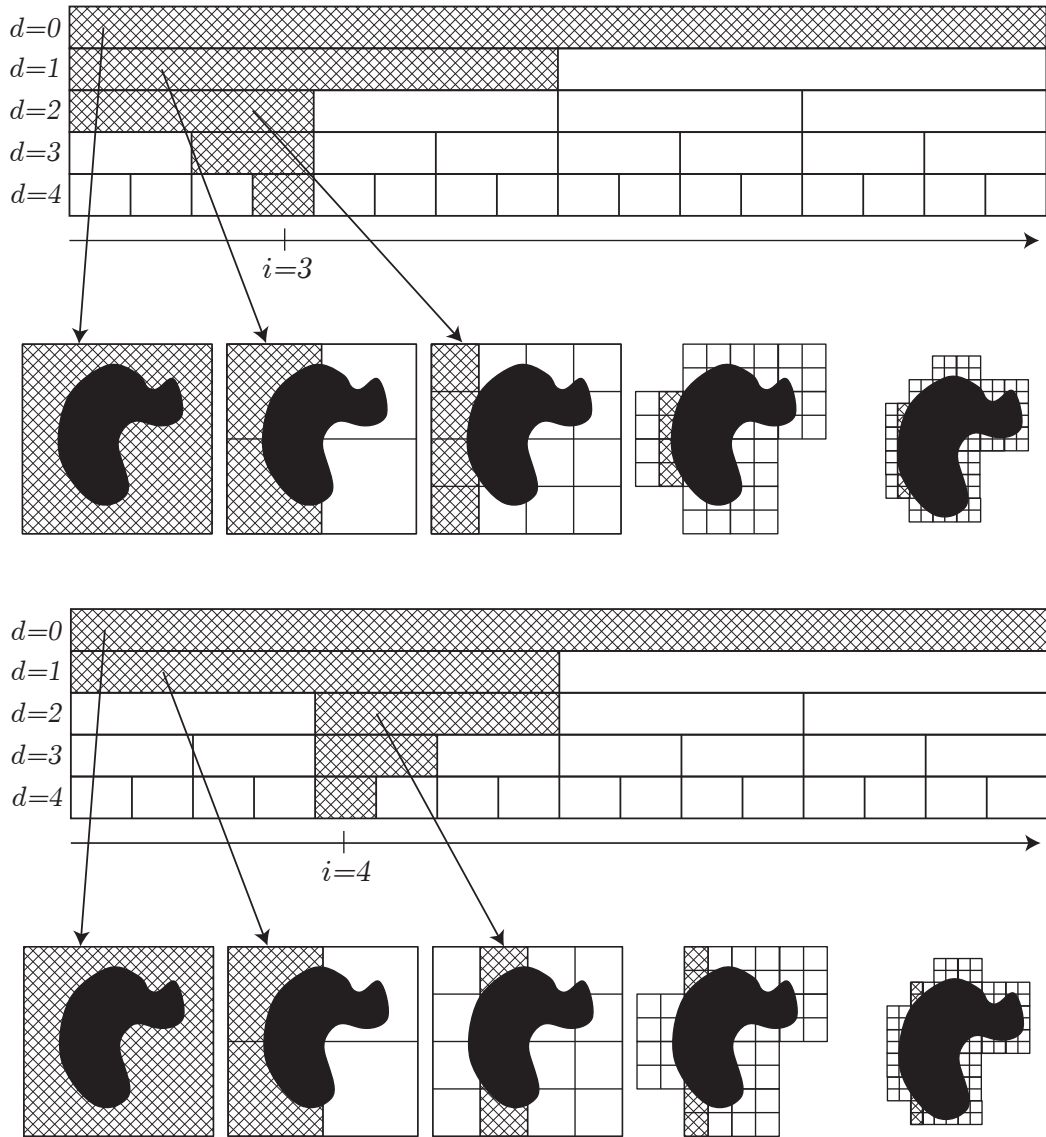


Figure 4.2: Illustration of the multilevel stream structure (top rows) and the corresponding quadtree nodes (bottom rows) at two moments in time ( $i = 3, 4$ ). In-core blocks and nodes are highlighted.

## CHAPTER 4. STREAMING SURFACE RECONSTRUCTION

To implement a data structure that supports this traversal pattern, we must address the fact that the in-core persistence of nodes depends on their depth, since coarser nodes are maintained in memory longer than finer ones (see Figure 4.2). This motivates the construction of a multi-stream octree data structure, consisting of  $D + 1$  different streams  $\{\mathcal{S}^0, \dots, \mathcal{S}^D\}$ .

Each stream  $\mathcal{S}^d$  contains all nodes  $o \in \mathcal{O}^d$ , and is partitioned into blocks  $\mathcal{S}^d[0], \dots, \mathcal{S}^d[2^d - 1]$  with the nodes in block  $\mathcal{S}^d[j]$  all centered on the plane  $x = (2j + 1)/2^{d+1}$ . Thus, at the coarsest depth,  $\mathcal{S}^0$  contains only one block  $\mathcal{S}^0[0]$  which in turn contains only one node, namely the octree root node. At finer depths, each block  $\mathcal{S}^d[j]$  generally contains  $O(2^d)$  nodes (out of  $2^{2d}$  nodes in a complete octree) because the surface has co-dimension 1.

Figure 4.2 shows a visualization of the multi-stream structure for a quadtree representation. Each row marked with a depth  $d = 0 \dots 4$  corresponds to a separate stream  $\mathcal{S}^d$ , and the rectangles within a row denote the blocks  $\mathcal{S}^d[j]$ . In the top two rows of the diagram, we see the data structure at sweep index  $i = 3$ . The in-core blocks which correspond to all the quadtree nodes that intersect the sweep-plane are highlighted. Note that as we advance to sweep index  $i = 4$  (shown in bottom two rows), not all streams need to be updated; in this example, it is only the streams at depths  $d = 2, 3, 4$  that are advanced.

At index  $i$ , the sweep plane intersects the nodes contained in  $\mathcal{S}^d[\lfloor i/2^{D-d-1} \rfloor]$ , which we denote by  $\mathcal{S}^d[\phi_d(i)]$ , or simply as  $\mathcal{S}_i^d$ . More generally, stream processing



operations may require access to nodes in a small neighborhood of the sweep plane. If the operation needs access to a  $k$ -neighborhood at each depth, we maintain an *in-core octree*  $\mathcal{O}_{i,k} \subset \mathcal{O}$  defined as the union

$$\mathcal{O}_{i,k} = \bigcup_{d=0}^D \mathcal{S}_{i,k}^d \quad \text{where} \quad \mathcal{S}_{i,k}^d = \bigcup_{j=-k}^k \mathcal{S}^d[\phi_d(i) + j]. \quad (4.1)$$

Thus, Figure 4.2 can be seen to correspond to  $\mathcal{O}_{i,0}$  at  $i = 3, 4$ .

An essential property of the in-core octree is that for any node  $o \in \mathcal{S}_i^d$  and any depth  $d' \leq d$ , the  $k$ -neighborhood of the ancestor of  $o$  at depth  $d'$ , denoted  $N_k^{d'}(o)$ , is guaranteed to be contained in  $\mathcal{O}_{i,k}$ , (i.e. to be in-core). As the sweep index is advanced from  $i$  to  $i + 1$ , the in-core octree  $\mathcal{O}_{i,k}$  is updated. Specifically, we compute the set of depths,  $D_i$ , at which the streams need to be advanced:

$$D_i = \{d \mid \phi_d(i) \neq \phi_d(i + 1)\} \quad (4.2)$$

and for each  $d \in D_i$  we can unload the block  $\mathcal{S}^d[\phi_d(i) - k]$  and load the block  $\mathcal{S}^d[\phi_d(i) + k + 1]$  into memory.

### 4.2.1 Implementation

We store each stream in a separate file, and using a 64-bit operating system, reserve contiguous blocks of virtual address space large enough to fully span the streams. An advantage of using virtual addressing is that, by simple addition with

## CHAPTER 4. STREAMING SURFACE RECONSTRUCTION

a base address, a pointer to a node can be represented by the node’s offset in the file.

Within each stream, an “active window” between a head pointer and a tail pointer is mapped to physical memory. To efficiently update these pointers during the sweep, we store the offset and extent of all blocks in an index structure, which forms a complete binary tree of height  $D + 1$ .

Although we exploit virtual memory addressing, we never rely on the operating system for demand-based paging, as this can be inefficient. Instead, we explicitly manage the memory mapping. As the head pointer advances through a stream, the appropriate pages of virtual memory are committed to physical memory and read from disk. And, as the tail pointer advances, dirty data is written to disk and memory pages are uncommitted. Memory management and I/O are performed asynchronously by a background thread, to allow for lazy write-back and anticipatory read-ahead. All I/O is performed at the granularity of 1 MB to maximize disk bandwidth and minimize disk seek overhead.

Additionally, we vertically partition the data for each depth into two separate streamed files that are advanced in lockstep; one containing the octree topology, and the other containing the Poisson system data (e.g. vector-field coefficients, divergence coefficients, solution, density, and iso-value). Since the first file becomes read-only after creation, it doesn’t need to be written back to disk in subsequent passes, thereby reducing the I/O workload.

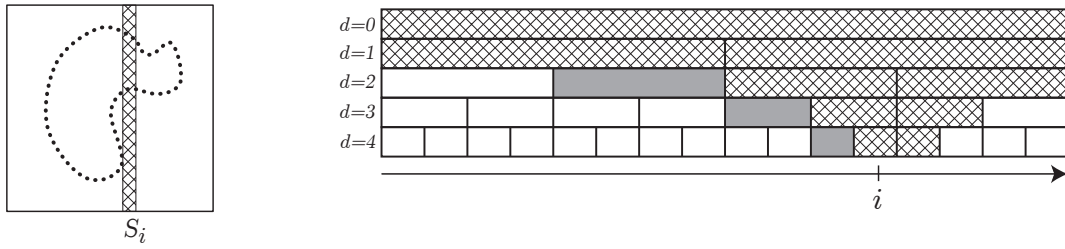


Figure 4.3: Construction of the out of core octree as points  $S_i$  are added to the tree. To process these points, the sub-tree that can be modified by the processing of points  $S_i$  is maintained in core (highlighted in grey and diamond hatching). After the points in  $S_i$  have been processed, the nodes that cannot be affected by the processing of points in  $S_{i+1}$  (grey) are written out to the streams.

### 4.3 A Simple Streaming Reconstruction

We now describe how Poisson surface reconstruction can be decomposed into a sequence of streaming passes (Figure 4.4). The focus here is to demonstrate that, thanks to the compact support of the basis functions  $F_o$ , each step of the reconstruction process involves local computation, and can therefore be implemented as a streaming pass. In Section 4.4 we show how these individual steps can be combined more efficiently into just three passes over the out-of-core data.

The discussion in this section is guided by Table 4.1, which summarizes the extent of the data that needs to be in-core to process block  $\mathcal{S}_i^d$  in each step of reconstruction. The key property that enables streaming reconstruction is that this data extent is always bounded by a neighborhood  $k$  at each depth: all the necessary data is available if we maintain an in-core octree  $\mathcal{O}_{i,k}$  as we sweep over

CHAPTER 4. STREAMING SURFACE RECONSTRUCTION

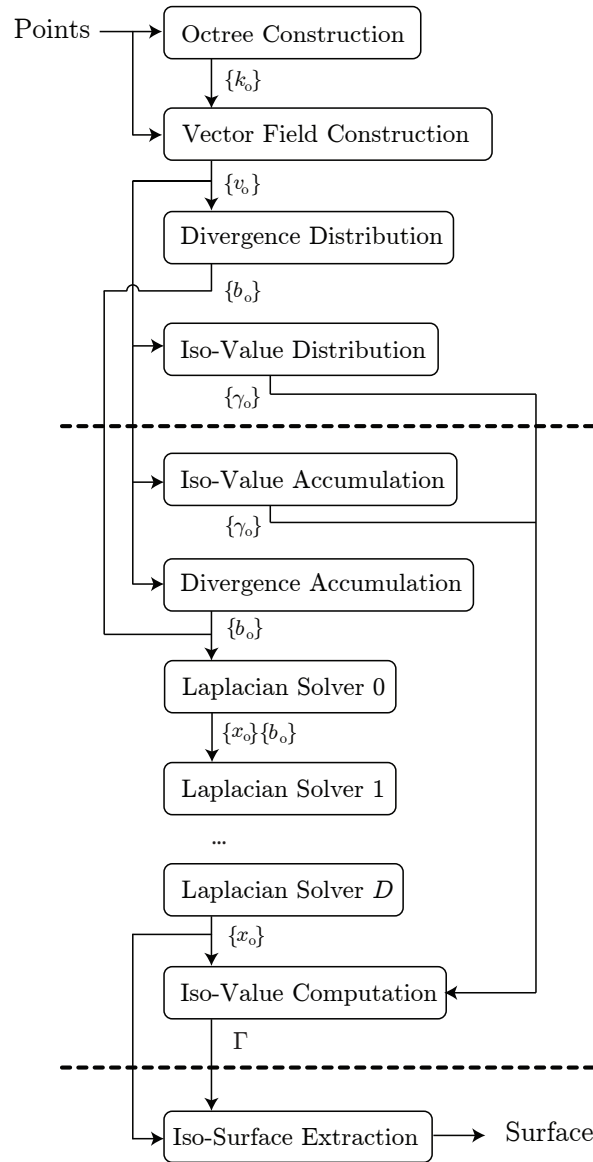


Figure 4.4: Sequence of streaming passes and flow of the out-of-core octree data, as described in the naive implementation of Section 4.3.

Step	Read	Write
Octree Construction ( $d=D-1$ )	$S_i$	$k_o: \mathcal{S}_{i,1}^{d'}$ $d' \leq d$
Vector Field Construction	$k_o: \mathcal{S}_{i,1}^d, S_j \ \phi_d(j)=\phi_d(i)$	$\vec{v}_o: \mathcal{S}_{i,1}^d$
Divergence Distribution	$\vec{v}_o: \mathcal{S}_i^d$	$b_o: \mathcal{S}_{i,2}^{d'}$ $d' \leq d$
Iso-Value Distribution	$ \vec{v}_o : \mathcal{S}_i^d$	$\gamma_o: \mathcal{S}_{i,1}^{d'}$ $d' \leq d$
Iso-Value Accumulation	$ \vec{v}_o : \mathcal{S}_{i,1}^{d'}$	$d' < d$ $\gamma_o: \mathcal{S}_i^d$
Divergence Accumulation	$\vec{v}_o: \mathcal{S}_{i,2}^{d'}$	$d' < d$ $b_o: \mathcal{S}_i^d$
Divergence Update	$x_o: \mathcal{S}_{i,2}^{d'}$	$d' < d$ $b_o: \mathcal{S}_i^d$
Laplacian Solver	$b_o: \mathcal{S}_{i,2}^d$	$x_o: \mathcal{S}_i^d$
Iso-Value Computation	$ \vec{v}_o , x_o, \gamma_o: \mathcal{S}_i^d$	iso-value $\Gamma$
Iso-Surface Extraction	$x_o: \mathcal{S}_{i,2}^d, \Gamma$	Surface Mesh

Table 4.1: Read and write operations when processing block  $\mathcal{S}_i^d$  in the various multilevel streaming computations.

index  $i$ .

Below, we briefly review the individual steps of the reconstruction process, providing the value of the neighborhood  $k$  that defines the size of the necessary in-core octree  $\mathcal{O}_{i,k}$ .

### 4.3.1 Pre-processing

First, we rotate the point set so that the major axis of its covariance matrix is aligned with the  $x$ -axis. The intention is to reduce the size of the cross-section encountered during the sweep, and hence the peak memory of the in-core octree  $\mathcal{O}_{i,k}$ . We then uniformly scale and translate the points so that they fit into the unit cube. Finally, we partition the points into subsets  $S_i \subset S$ , whose  $x$ -coordinates lie in the range  $[i/2^D, (i+1)/2^D]$ . This partitioning process

is essentially a binning process, and is implemented efficiently as a single-input/multiple-output streaming operation.

---

**Algorithm 4.1** The algorithm to preprocess the pointset.

---

```

PointSamples  $\leftarrow$  PCAAlign(PointSamples)
PointSamples  $\leftarrow$  NormalizeBoundingBox(PointSamples)
for all  $s \in$  PointSamples do
   $i \leftarrow s.$ Position.x  $\times 2^D$ 
  WriteToBucket( $i, s$ )
end for
PointSamples  $\leftarrow$  nil
for all  $b \in$  Buckets do
  PointSamples  $\leftarrow$  PointSamples + Sort( $b$ )
end for

```

---

### 4.3.2 Octree Construction ( $k = 1$ )

At index  $i$ , we read in the subset of points  $S_i \subset S$ . For each  $s \in S_i$  and every depth  $d$ , we refine the in-core octree so that the node  $o^d(s) \in \mathcal{O}^d$  containing  $s$  and its one-ring neighbors are all present in  $\mathcal{O}_{i,1}$ , adding new nodes as necessary. We also update the density estimator ( $W_d$ ) coefficients  $\{k_o\}$  by having each sample  $s$  splat a unit value into the one-ring neighborhood of  $o^d(s)$ .

### 4.3.3 Vector Field Construction ( $k = 1$ )

At index  $i$  we iterate over all samples  $s \in S_i$ . For each  $s$ , we evaluate the density estimators  $W_d$  to determine the corresponding depth  $D_{splat}$  and splat the sample's (weighted) normal into the one-ring neighborhoods  $o^{D_{splat}}(s)$  and  $o^{D_{splat}+1}(s)$  to

---

**Algorithm 4.2** Constructing the tree for slice  $i$ 


---

```

for all  $s \in \text{PointSamples}[i]$  do
   $o \leftarrow \text{OctreeRoot}$ 
  for  $d = 0$  to  $\text{MaxDepth}$  do
     $i \leftarrow \text{OctantIndex}(s.\text{Position})$ 
     $o \leftarrow \text{GetOrCreateChild}(o, i)$ 
     $\text{RefineNeighbors}(o)$ 
     $N \leftarrow \text{GetNeighbors}(o, d)$ 
    for all  $o' \in N$  do
       $\alpha \leftarrow \text{GetSplattingWeight}(o, o', s.\text{Position})$ 
       $o'.k \leftarrow o'.k + \alpha$ 
    end for
  end for
end for

```

---

update the vector field coefficients  $\{\vec{v}_o\}$ .

Because  $F_o$  is supported in a one-ring neighborhood of  $o$ ,  $W_d(s.p)$  can be evaluated without access to  $k_{o'}$  for  $o' \notin \mathcal{O}_{i,1}$ .

### 4.3.4 Divergence Computation ( $k = 2$ )

In streaming through a  $k$ -neighborhood octree, it is guaranteed that the neighbors of a node and the neighbors of its ancestors will be in-core. However, there is no guarantee that the neighbors of its descendants will be within the working window. As a result, we decompose the divergence computation into two steps. Following Equation 3.9, at sweep index  $i$ :

1. We *distribute* divergence constraints to nodes at depth  $d' \leq d$  by iterating over  $o' \in \mathcal{N}_{d'}^2(o)$  and adding  $\langle \nabla \cdot (\vec{v}_o F_o), F_{o'} \rangle$  to  $b_{o'}$ .

---

**Algorithm 4.3** Constructing the vector field for slice  $i$ 


---

```

for all  $s \in \text{PointSamples}[i]$  do
   $o \leftarrow \text{OctreeRoot}$ 
  for  $d = 0$  to  $\text{MaxDepth}$  do
     $N \leftarrow \text{GetNeighbors}(o, d)$ 
     $\text{Weight}[d] \leftarrow 0$ 
    for all  $oo \in N$  do
       $\alpha \leftarrow \text{GetSamplingWeight}(o, oo, s.\text{Position})$ 
       $\text{Weight}[d] \leftarrow \text{Weight}[d] + oo.k \times \alpha$ 
    end for
     $i \leftarrow \text{OctantIndex}(s.\text{Position})$ 
     $o \leftarrow \text{GetChild}(o, i)$ 
  end for
   $d \leftarrow 0$ 
  while  $\text{Weight}[d + 1] > \text{SamplesPerNode}$  and  $d \leq \text{MaxDepth}$  do
     $d \leftarrow d + 1$ 
  end while
   $dd \leftarrow d + \log(\text{Weight}[d] / \text{SamplesPerNode}) / \log(\text{Weight}[d] / \text{Weight}[d + 1])$ 
   $\delta \leftarrow \text{clamp}(dd - d, 0, 1)$ 
   $\text{NormalWeight} = \text{pow}(4.0, -dd + (d + 1) \times 1.5)$ 
   $N \leftarrow \text{GetNeighbors}(o, d + 1)$ 
  for all  $oo \in N$  do
     $\text{SplatNormal}(oo, s.\text{Normal} \times \text{NormalWeight} \times \delta)$ 
  end for
   $\text{NormalWeight} = \text{pow}(4.0, -dd + d \times 1.5)$ 
   $N \leftarrow \text{GetNeighbors}(o, d)$ 
  for all  $oo \in N$  do
     $\text{SplatNormal}(oo, s.\text{Normal} \times \text{NormalWeight} \times (1 - \delta))$ 
  end for
end for

```

---



CHAPTER 4. STREAMING SURFACE RECONSTRUCTION

2. We *accumulate* divergence constraints from nodes at depths  $d' < d$  by

iterating over  $o' \in \mathcal{N}_{d'}^2(o)$  and adding  $\langle \nabla \cdot (\vec{v}_{o'} F_{o'}), F_o \rangle$  to  $b_o$ .

Because  $F_o$  is supported in a one-ring neighborhood of  $o$ ,  $\langle \nabla \cdot (\vec{v}_{o'} F_{o'}), F_o \rangle \neq 0$

only if  $o \in \mathcal{N}_{d'}^2(o)$ , so both  $b_o$  and  $b_{o'}$  can be incremented without access to  $v_{o'}$  for

$o' \notin \mathcal{O}_{i,2}$ .

---

**Algorithm 4.4** Computing the divergence for slice  $i$  at depth  $d$

---

```

O ← OctreeNode[d][i]
for all o ∈ O do
  Fo ← GetNodeFunction(o)
  {Distribute}
  for dd = 0 to d do
    N ← GetNeighbors(o, dd)
    for all oo ∈ N do
      Foo ← GetNodeFunction(oo)
      bx ← o.vx × dx(Fo)
      by ← o.vy × dy(Fo)
      bz ← o.vz × dz(Fo)
      oo.b ← oo.b + dot(bx + by + bz, Foo)
    end for
  end for
  {Accumulate}
  for dd = 0 to d − 1 do
    N ← GetNeighbors(o, dd)
    for all oo ∈ N do
      Foo ← GetNodeFunction(oo)
      bx ← oo.vx × dx(Foo)
      by ← oo.vy × dy(Foo)
      bz ← oo.vz × dz(Foo)
      o.b ← o.b + dot(bx + by + bz, Foo)
    end for
  end for
end for

```

---

### 4.3.5 Poisson System Solution ( $k = 2$ )

The most straightforward implementation of the cascadic multigrid algorithm performs two streaming passes for each depth  $0 \leq d \leq D$  (from coarsest to finest), first updating  $b^d$  in the linear system  $L^d x^d = b^d$  using the solution at depths  $d' < d$ , and then solving the system. We switch from using a conjugate gradient solver to using a Gauss-Seidel solver because the Gauss-Seidel method supports local updates (which the conjugate gradients method does not). We describe this approach in Section 4.4 and show that it is possible to perform *all*  $2 \times D$  passes in a *single* multilevel streaming pass.

1. We *update* the divergence coefficients  $b_o$  for  $o \in \mathcal{S}_i^d$  by iterating over  $o' \in \mathcal{N}_2^{d'}(o)$  for all  $d' < d$  and subtracting the value  $x_{o'} L_{o,o'}$  from  $b_o$  (following Equation 3.12).
2. We *solve* for the values  $x_o$  with  $o \in \mathcal{S}_i^d$  by performing several iterations over the nodes in  $\mathcal{S}_i^d$  and, for each node  $o$ , performing the Gauss-Seidel update:

$$x_o \leftarrow \frac{b_o - \sum_{o' \in \mathcal{O}^d} L_{o,o'} x_{o'}}{L_{o,o}}. \quad (4.3)$$

Because  $F_o$  is supported in a one-ring neighborhood of  $o$ ,  $L_{o,o'} \neq 0$  only if  $o' \in \mathcal{N}_2^{d'}(o)$ . Updating  $b_o$  and solving for  $x_o$  can therefore be done without access to  $x_{o'}$  for  $o' \notin \mathcal{O}_{i,2}$ .

Note that this is not a traditional implementation of a Gauss-Seidel solver since we perform multiple relaxations of the nodes in  $\mathcal{S}_i^d$  before proceeding on to the nodes in  $\mathcal{S}_{i+1}^d$ . Nonetheless, as we will discuss later in this chapter, we have found that the reconstruction results remain accurate.

### 4.3.6 Computing the Iso-Value ( $k = 1$ )

As with the computation of the divergence, we decompose the iso-value computation into multiple steps. Following Equation 3.13, at sweep index  $i$ :

1. We *distribute* the iso-value contribution to nodes at depths  $d' < d$  by iterating over  $o' \in N_2^{d'}(o)$  and adding  $|\vec{v}_{o'}|F_{o'}(o.\text{center})$  to  $\gamma_{o'}$ .
2. We *accumulate* the iso-value contribution from nodes at depths  $d' \leq d$  by iterating over  $o' \in N_2^{d'}(o)$  and adding  $|\vec{v}_o|F_o(o'.\text{center})$  to  $\gamma_o$ .
3. We *compute* the iso-value by adding  $x_o\gamma_o$  to the numerator of  $\gamma$  and adding  $|\vec{v}_o|$  to the denominator.

### 4.3.7 Extracting the Iso-Surface ( $k = 2$ )

We extract the iso-surface by iterating over the leaf nodes, computing the value of  $\chi$  at the eight cell corners, solving for the positions of  $\gamma$ -crossings along the edges, and extracting the triangulation.

---

**Algorithm 4.5** Solving the Poisson system for slice  $i$  at depth  $d$ 


---

```

 $O \leftarrow \text{OctreeNode}s[d][i]$ 
 $L \leftarrow \text{EmptySparseMatrix}$ 
 $b \leftarrow \text{EmptyVector}$ 
 $j \leftarrow 0$ 
{Update divergence, build matrix}
for all  $o \in O$  do
   $F_o \leftarrow \text{GetNodeFunction}(o)$ 
  for  $dd = 0$  to  $d$  do
     $N \leftarrow \text{GetNeighbours}(o, dd)$ 
     $k \leftarrow 0$ 
    for all  $oo \in N$  do
       $F_{oo} \leftarrow \text{GetNodeFunction}(oo)$ 
       $L_x \leftarrow \text{dot}(d2x(F_{oo}), F_o)$ 
       $L_y \leftarrow \text{dot}(d2y(F_{oo}), F_o)$ 
       $L_z \leftarrow \text{dot}(d2z(F_{oo}), F_o)$ 
       $L \leftarrow L_x + L_y + L_z$ 
      if  $d = dd$  then
         $L[j][k] \leftarrow L$ 
         $k \leftarrow k + 1$ 
      else
         $o.b \leftarrow o.b - oo.x \times L$ 
      end if
    end for
  end for
   $b[j] \leftarrow o.b$ 
   $j \leftarrow j + 1$ 
end for
{Solve}
 $x \leftarrow \text{Solve}(L, b)$ 
{Write back solution to nodes}
 $j \leftarrow 0$ 
for all  $o \in O$  do
   $o.x \leftarrow x[j]$ 
   $i \leftarrow j + 1$ 
end for

```

---

---

**Algorithm 4.6** Computing the iso-value for slice  $i$  at depth  $d$ 


---

```

 $O \leftarrow \text{OctreeNodeNodes}[d][i]$ 
for all  $o \in O$  do
     $F_o \leftarrow \text{GetNodeFunction}(o)$ 
    {Accumulate}
    for  $dd = 0$  to  $d - 1$  do
         $N \leftarrow \text{GetNeighbors}(o, dd)$ 
        for all  $oo \in N$  do
             $o.\gamma \leftarrow o.\gamma + |o.v| \times F_o(oo.Center)$ 
        end for
    end for
    {Distribute}
    for  $dd = 0$  to  $d$  do
         $N \leftarrow \text{GetNeighbors}(o, dd)$ 
        for all  $oo \in N$  do
             $F_{oo} \leftarrow \text{GetNodeFunction}(oo)$ 
             $oo.\gamma \leftarrow oo.\gamma + |oo.v| \times F_{oo}(o.Center)$ 
        end for
    end for
end for

```

---

The challenge in implementing the iso-surface extraction is the evaluation of  $\chi$  at the corners of a leaf node  $o \in \mathcal{S}_i^d$ . Since the value at a corner can be determined by the values of  $x_{o'} \in \mathcal{O}^{d'}$  with  $d' > d$ , we are not guaranteed to have the necessary information in-core when processing the node  $o$ .

To address this challenge, we observe that because the functions  $F_{o'}$  are supported in the one-ring neighborhood of  $o'$ , for a corner  $c \in o$  we have  $F_{o'}(c) \neq 0$  only if either  $d' \leq d$  and  $o' \in N_1^{d'}(o)$ , or  $d' > d$  and  $c$  is also a corner of  $o'$ . Thus, when  $o$  is the finest node adjacent to corner  $c$ ,  $\chi(c)$  can be computed using only values  $x_{o'}$  for  $o' \in N^{d'}(o)$  and  $d' \leq d$ .

This observation motivates an algorithm for iso-surface extraction that iterates

## CHAPTER 4. STREAMING SURFACE RECONSTRUCTION

over the leaf nodes, from the finest to the coarsest, and stores the evaluation of  $\chi$  at the corners in a temporary hash table. For a given corner  $c$  of a leaf node  $o \in \mathcal{O}^d$ , we check if there is an entry in the hash table corresponding to  $c$ . If there is not, this implies that there are no nodes at depth  $d' > d$  containing  $c$  as a corner and that the value  $\chi(c)$  can be computed using only information associated to nodes in the one-ring neighborhood of the ancestors of node  $o$ .

In practice, separate hash tables are associated with the corners of the front and back of the leaf nodes at each depth. As the sweep plane is advanced, the front hash table is updated by evaluating the front corners of leaf nodes intersecting the sweep plane and the back corners of leaf nodes immediately in front of the sweep plane. For a corner  $c \in o$  that is also a corner of a node  $o' \in \mathcal{O}^{d-1}$ , we add the value  $\chi(c)$  to the front hash table at depth  $d - 1$ . Finally, after extracting the iso-surface in the current sweep index, we swap the front and back hash tables and clear the front one. It is also at this point that vertices are finalized [27].

To allow for efficient out-of-core rendering of our mesh, we write to a block-based streaming mesh format. Unlike the approach of Isenburg *et al.* [27] we separate the vertex data and triangle indices into two separate streams, which store data in blocks of size  $b$ . To facilitate the efficient loading and unloading of data, we also write an index structure that, for each block of triangles, references the earliest and latest blocks of vertex data that are needed to be able to follow all vertex indices in the block. The earliest and latest vertex block indices are then

optimized for streaming by making them monotonically increasing, making the sequence of required vertex data blocks contiguous and always streaming forward through the data. This index structure makes the process of streaming the mesh for rendering or post-processing highly efficient. All loading and unloading of vertex data is controlled by the index, alleviating the need to scan each triangle as it is processed and maintain fine-grained book-keeping information.

## 4.4 An Optimized Implementation

In the previous section, we showed that the locality of the Poisson reconstruction steps allows for stream processing. In this section, we show how the different streaming passes can be merged into three multilevel streaming passes. Our approach is motivated by two observations. First, we can merge streaming steps when there are no conflicting data dependencies. Second, even when there are dependencies, we may be able to pipeline the steps, resolving the dependencies with only a small increase in the size of the working set. Due to the data dependencies, three passes are a lower-bound for our reconstruction algorithm:

- **First Pass:** We construct the octree, sample the weighting function, and the vector field, and perform the distributive half of the divergence and iso-value weighting calculations.

- **Second Pass** We perform the accumulative half of the divergence and iso-value weighting calculations. Then, for each depth, we perform the divergence update, construct and solve the Poisson system solution. Finally, we compute the iso-value.
- **Third Pass:** We extract the iso-surface.

Because the values of  $\{b_o\}$  for coarse nodes are not finalized until late in the first pass, and because the linear systems at coarser depths need to be solved before the systems at finer depths, the solving of the Poisson equation cannot begin until the first pass has completed. This reflects the global nature of the Poisson system, which requires all the data to have been seen before the solving can commence. Similarly, the iso-surface extraction cannot begin until the iso-value has been computed, which is not complete until the solution has been completely solved.

#### 4.4.1 First Pass ( $k = 6$ )

To merge the processing steps in the first pass, we must resolve the data dependencies between different steps. We do this by pipelining the steps, delaying execution of later steps to allow earlier steps to finalize the dependent data.

Using the sizes of the read/write neighborhoods described in Table 4.1, we can resolve the data dependencies in the first pass by iterating over the sweep indices, for each  $i$ :



## CHAPTER 4. STREAMING SURFACE RECONSTRUCTION

- Constructing the octree for  $\mathcal{S}^{D-1}[i + 5]$

and for each  $d \in D_i$

- Constructing the vector field for  $\mathcal{S}^d[\phi_d(i)]$
- Distributing the divergence for  $\mathcal{S}^d[\phi_d(i) - 3]$
- Distributing the iso-value contribution for  $\mathcal{S}^d[\phi_d(i) - 3]$

Taking into account the size of the write neighborhoods for octree construction and divergence distribution, the first pass of streaming reconstruction can be implemented by maintaining the octree  $\mathcal{O}_{i,6}$  in the working set at sweep index  $i$ .

### 4.4.1.1 Buffering Samples

In addition to maintaining a small working octree, our method must also address the fact that, to implement the vector field construction for block  $\mathcal{S}_i^d$ , the processing step needs access to each sample which lies in the span of  $\mathcal{S}_i^d$  and has failed the density test at greater depths.

The exhaustive testing of all samples which lie in the span of  $\mathcal{S}_i^d$  can be a computational bottleneck for our system since it requires  $D$  passes through the ordered point set. This is unnecessarily expensive since we expect a sample's density estimate to increase by a factor of four as the depth is decremented. The number of samples processed at depth  $d$ , but failing the density test, should drop by a factor of four, while the number of samples that lie in the span of  $\mathcal{S}_i^{d-1}$  should only increase by a factor of two.

We address this concern by associating a sample buffer to each depth and processing the blocks in decreasing depth order. Samples are added into the buffer at depth  $D$  during the octree construction step, and are promoted to the buffer at depth  $d - 1$  if they fail the density test at depth  $d$  in the vector field construction step. (Points in the depth- $d$  buffer that lie in the span of  $\mathcal{S}^d[\phi_d(i)]$  are removed from the buffer at the end of the vector field construction step.)

#### 4.4.2 Second Pass ( $k = 8$ )

As in the first pass, we merge the steps in the second pass by pipelining them to resolve data dependencies. However, since the consolidation of these steps into a single pass forces us to iterate over the depths before iterating over the sweep indices, the merging of the divergence update with the Poisson system solution poses a challenge. For a fixed sweep index, we can no longer treat the individual steps as atomic because this would result in a circular data dependency: the modification of  $\{b_o\}$  in the divergence update requires access to  $\{x_o\}$  set in the Poisson system solver which, in turn, requires access to  $\{b_o\}$ .

We resolve this problem by separately considering the pipelining that needs to be performed to resolve the data dependencies due to sweep index and due to depth.

### 4.4.2.1 Index Dependencies

Fixing a depth  $d$  and assuming no cross-depth data dependencies, we define the scheduling as we did in the first pass. Iterating over the (depth-relative) sweep index  $i^d$ , with  $0 \leq i^d < 2^d$ , we:

- Accumulate the iso-value contribution for  $\mathcal{S}^d[i^d]$
- Accumulate the divergence for  $\mathcal{S}^d[i^d]$
- Update the divergence for  $\mathcal{S}^d[i^d]$
- Solve the Poisson system for  $\mathcal{S}^d[i^d - 3]$
- Compute the iso-value for  $\mathcal{S}^d[i^d - 4]$

### 4.4.2.2 Depth Dependencies

To resolve the depth-related dependencies, we offset the values of  $i^d$  so that values required at finer depths are guaranteed to have been set at coarser ones.

Analyzing the size of the read/write neighborhoods shows that the dependencies can be resolved if the indices satisfy the property  $i^{d-1} \geq \lfloor i^d/2 \rfloor + 6$ . Expressing  $i^d$  as an offset from the finest index,  $i^d = \phi_d(i^{h-1}) + \delta^d$ , and initializing with  $\delta^{h-1} = 0$ , we obtain a recursive expression for the offsets:  $\vec{\delta}^d = \{11, \dots, 11, 10, 9, 6, 0\}$ . Thus, setting  $i^{h-1} = i - 3$ , the second reconstruction pass can be implemented by maintaining the octree  $\mathcal{O}_{i,8}$  in the working set at sweep index  $i$ .

In practice, we can further reduce the memory requirements by observing that

processing at the finest depths requires a narrower window size. This allows us to maintain a working octree with fewer stream blocks at the finest depths.

Figure 4.1 shows an example of the three streaming passes for the reconstruction of a 2D point set, showing the state of the reconstruction at different sweep indices (indicated by the arrows). As can be seen, the offsetting of the pipeline steps in the second pass forces coarser nodes to be solved ahead of the sweep line, resulting in a lower resolution reconstruction emerging to the right of the sweep index.

## 4.5 Results

### 4.5.1 Large Datasets

To evaluate our method, we have reconstructed highly detailed surfaces from large scanned datasets, as summarized in Table 4.2. All results use a target of  $\kappa = 2$  samples per octree node. Figure 4.6 shows a surface reconstruction of Michelangelo’s David statue from an input of 216M oriented points from raw scan data. The output surface of 210M triangles was generated at depth 13, and required only 780 MB of memory. In contrast, the in-core algorithm presented in Chapter 3 only produced a 20M triangle approximation of this same model (at depth 11), and required 4.4 GB of memory. Figure 4.5 shows a close-up visual comparison.

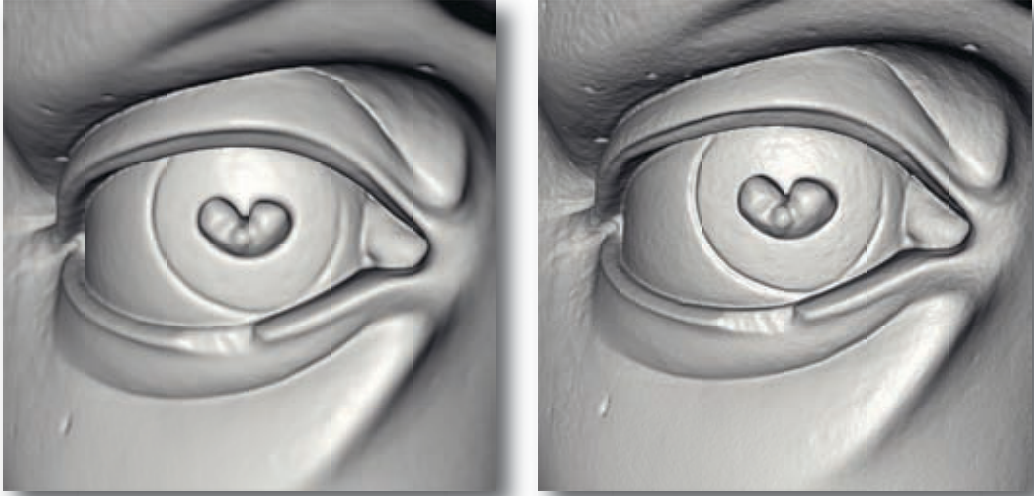


Figure 4.5: Comparing the results of the in-core algorithm (left; depth 11; 4,442 MB peak memory) and streaming algorithm (right; depth 13; 780 MB peak memory).

As another example of our algorithm’s ability to reconstruct large models, Figure 4.7 presents a reconstruction of Michelangelo’s Awakening statue from 391M points from raw scan data. At a maximum depth of 14, our streaming solution produced a mesh of 431M triangles in 82 hours. Although the storage required for the out-of-core data structure was 104 GB, our reconstruction algorithm never required more than 2.1 GB of working memory. Reconstructions

Model	Points	$D + 1$	Triangles	Time (h)	Mem (MB)	Disk (MB)
Lucy Statue	95M	12	26.2M	3.1	138	5,135
David Head	216M	13	210M	32.3	780	62,464
Awakening	391M	13	149M	26.6	990	35,840
Awakening	391M	14	431M	82.4	2120	106,496

Table 4.2: Quantitative results for multilevel streaming reconstructions, showing input points, octree height  $D + 1$ , output mesh triangles, total execution time (hours), memory use (MB), and total octree stream size (MB).

at this resolution allow us to clearly see fine detail such as chisel markings that could not be seen at lower resolutions.

## 4.5.2 Scalable Memory Use

Each of our three multilevel streaming passes only maintains a small window on the entire data structure at any one time. Figure 4.8 shows how the maximum size of these windows varies with output resolution. By comparison, the curve for the in-core algorithm grows so quickly that it exits the graph on the upper left.

Table 4.3 shows the octree size and peak memory use as a function of the resolution ( $r = 2^D$ ) of the octree. As expected, the total octree size has complexity  $O(r^2)$  since the surface has co-dimension 1. However, using the streaming reconstruction, the size of the in-core window only scales as  $O(r)$ , allowing the streaming algorithm to process datasets that far exceed a system’s main memory capacity.

The unexpectedly large memory use for the coarser resolutions is due to the buffering of points that occurs during octree construction. When the tree is artificially restricted to a small depth, many more points fall into the bins  $S_i$  traversed at each sweep step. However, this is an atypical scenario.

Memory use is further highlighted in Figure 4.9, which plots memory use over time through each of the three multilevel streaming passes during the reconstruction of the Lucy statue. The two different plot curves show how the

CHAPTER 4. STREAMING SURFACE RECONSTRUCTION

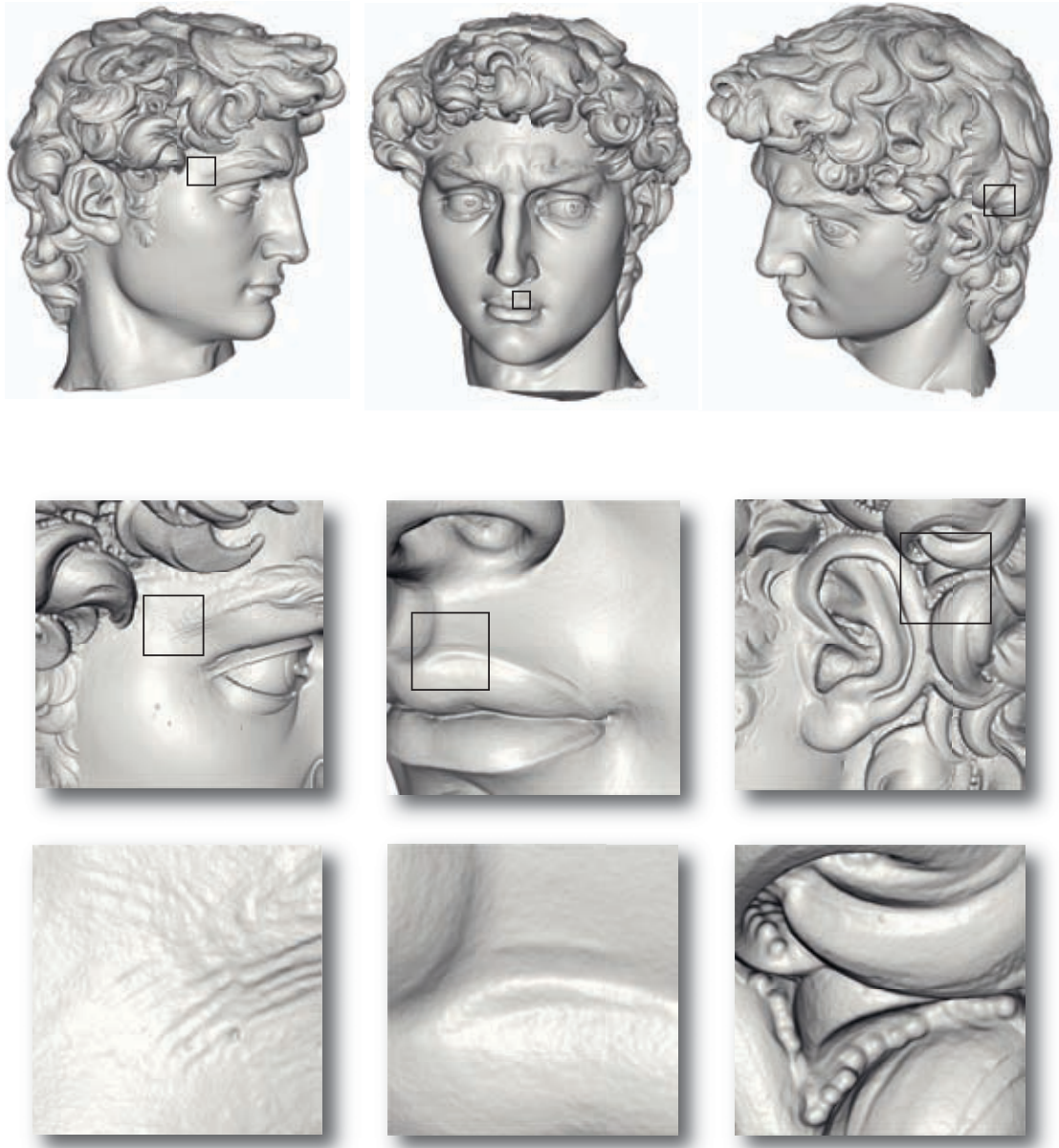


Figure 4.6: Views of our reconstruction of the head of Michelangelo's David. Maximum tree depth was 13, with a target of 2 samples per node.

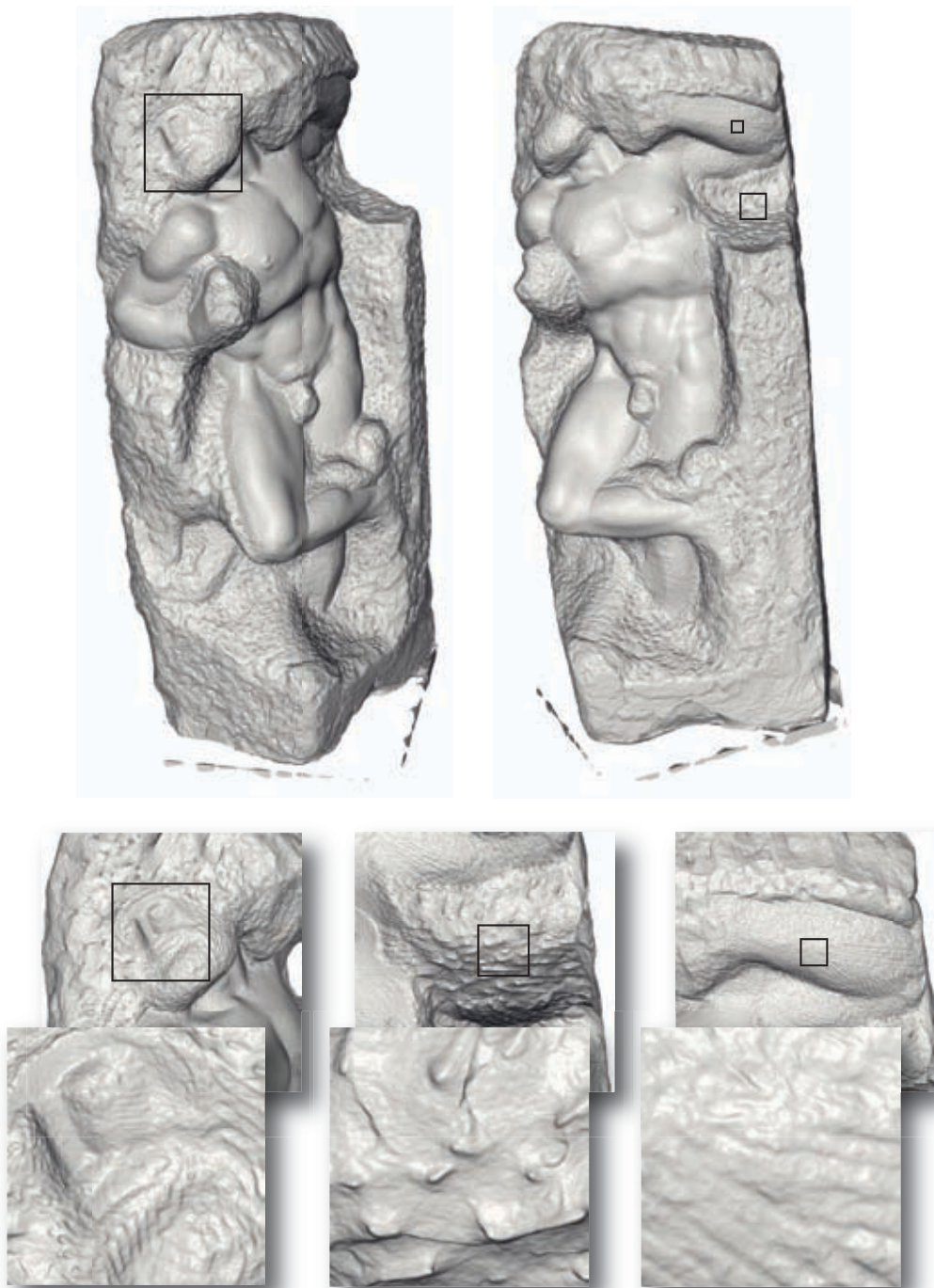


Figure 4.7: Views of our reconstruction of Michelangelo's Awakening statue. The maximum tree depth was 14 with a target of 2 samples per node.



## CHAPTER 4. STREAMING SURFACE RECONSTRUCTION

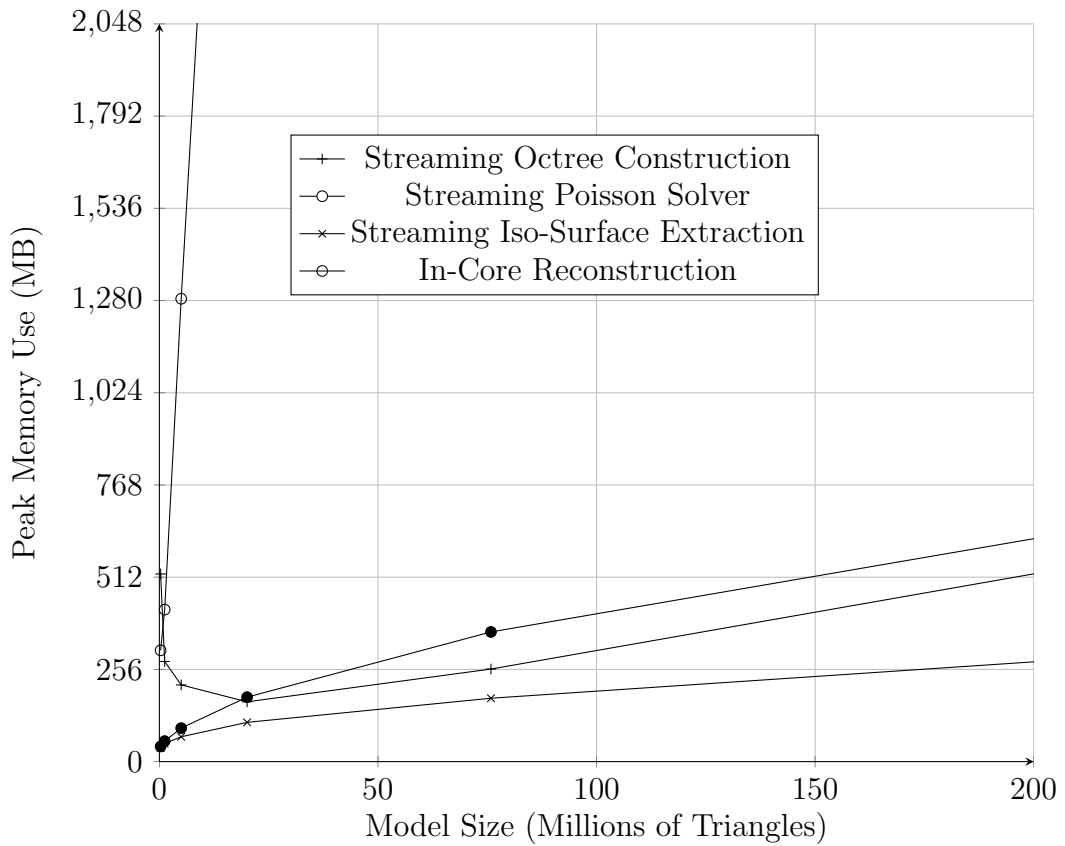
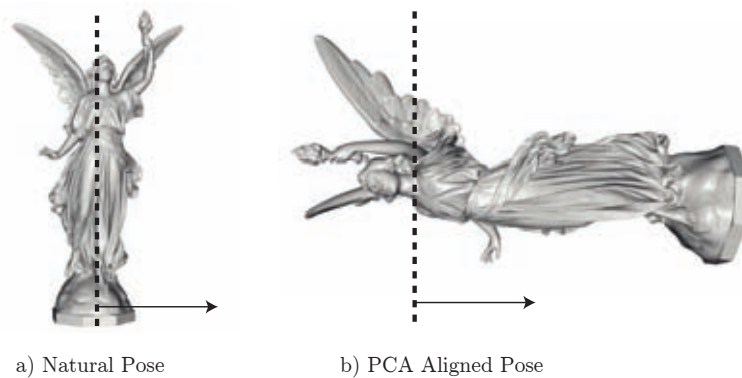


Figure 4.8: The peak working set in our 3 multilevel streaming passes, and in the in-core algorithm (far left), for a range of reconstructions of the head of Michelangelo’s David.



## CHAPTER 4. STREAMING SURFACE RECONSTRUCTION

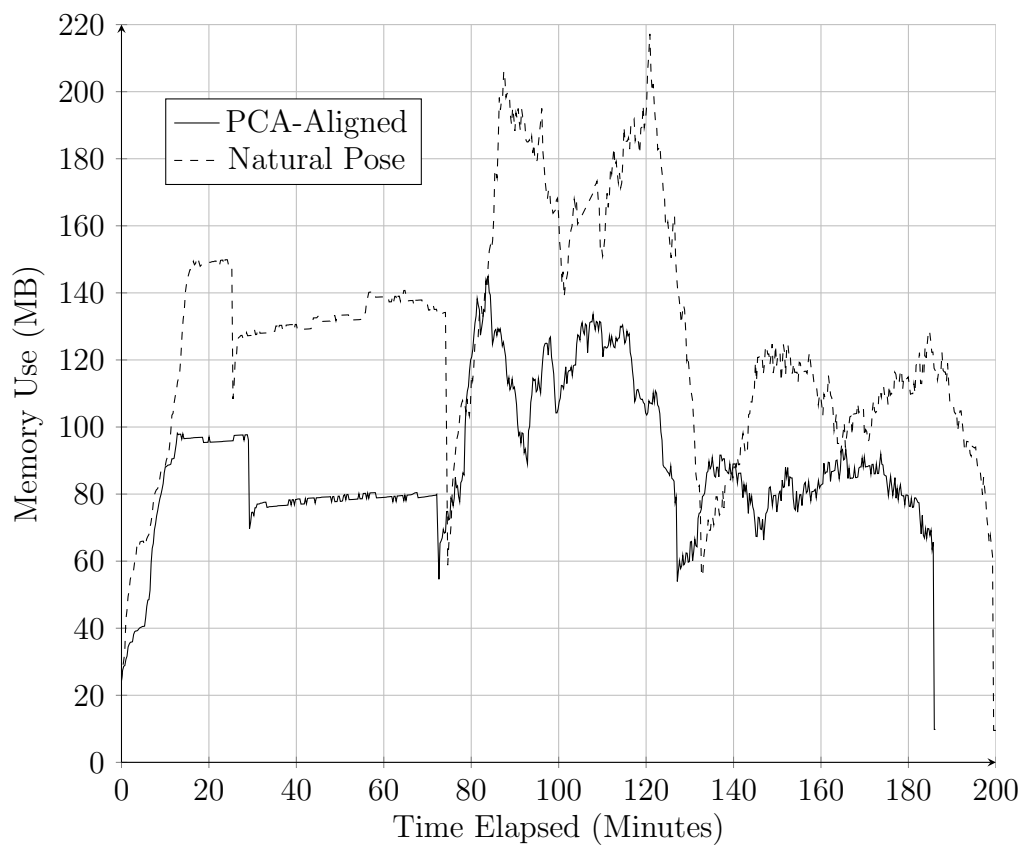


Figure 4.9: Memory use over time for a depth 12 reconstruction of the “Lucy” statue using two different poses of the model.

## CHAPTER 4. STREAMING SURFACE RECONSTRUCTION

sweep plane orientation can affect performance. The dashed curve corresponds to using the  $x$ -axis as the sweep direction, with the statue oriented in its original vertical pose (Figure 4.9a); in this orientation, the intersection of the surface with the sweep plane can be large, resulting in a peak memory use of 223 MB. The solid curve corresponds to using the dominant principal direction of the point set as the sweep direction (Figure 4.9b): this orientation reduces the intersection of the sweep plane with the surface, resulting in a peak memory use of only 138 MB.

The graph also shows that the three multilevel streaming passes have similar memory requirements and running times. The graphs do not include the pre-processing operations for orienting, scaling, and binning the points. However, this pre-processing is negligible as it requires only about 1% of the total execution time and uses less memory than the multilevel streaming passes.

### 4.5.3 Computation Times

Table 4.3 reveals that our streaming algorithm is time-competitive with the in-core algorithm despite the large amount of I/O. The streaming overhead is small because the overall process is compute-bound and the stream read-ahead prevents stalls in computation.

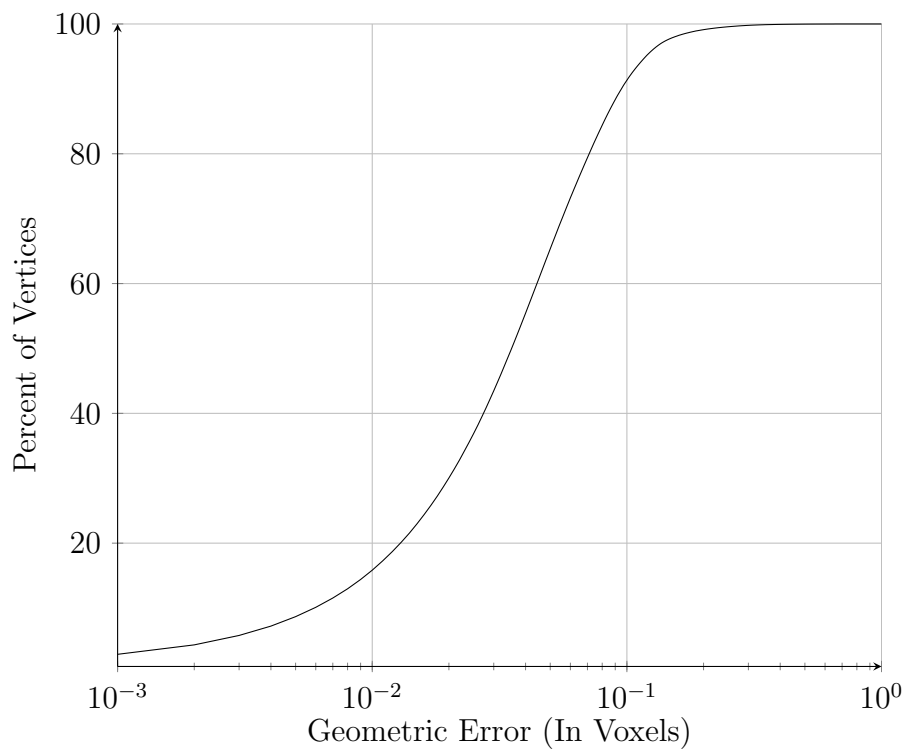


Figure 4.10: The cumulative distribution of geometric error for a depth 12 reconstruction of the “Lucy” statue when compared to the in-core algorithm of Chapter 3.

### 4.5.4 Streaming Solver Accuracy

Because our streaming solver computes an iterative solution to the Poisson equation, the numerical accuracy of the solution could impact the geometric accuracy of the resulting surface mesh. (This topic is discussed further in Section 4.6.) To test geometric accuracy, we compare the surface mesh generated by our streaming algorithm to that generated by the in-core algorithm presented in Chapter 3. Figure 4.10 graphs the cumulative distribution of reconstruction error, measured as the distance in voxel units from vertices on the reconstructed surface to the nearest points on the reference surface. Despite the fact that our streaming cascadic multigrid performs only a single sweep at each level, the resulting surface mesh is still very accurate – only 8% of the vertices have an error greater than 0.1 voxels, and the maximum error is 0.651 voxels.

## 4.6 Discussion

Solving the Poisson system in streaming fashion is a challenging task since it involves a global linear system in which Laplacian values at one point affect the solution at points faraway. The key ingredient that enables an effective streaming solution is the use of a cascading multigrid approach.

To demonstrate the importance of a multi-grid solver, Figure 4.11 shows the quality of solutions to a 2D Poisson problem using three different techniques. The

## CHAPTER 4. STREAMING SURFACE RECONSTRUCTION

first row shows the reconstructions obtained with 1, 4, 16, and 64 iterations of a Gauss-Seidel solver that streams through the column blocks of the image, much like one of the *single-level* streaming passes described in Section 4.4. As shown in the second row, even if we replace the Gauss-Seidel solver with the more efficient (but non-streaming) conjugate-gradient solver, the convergence is still too slow, requiring at least 64 passes through the data to obtain an approximate solution. In contrast, a cascadic multigrid solver (bottom row) quickly converges to the indicator function.

For general problems, a multigrid solver typically requires V-cycles, which could involve more streaming passes, but remarkably, for our reconstruction problem, a single cascadic pass is usually sufficient. The intuition is that, in the context of surface reconstruction, the Poisson solution  $\chi$  approximates an indicator function, and is thus only used to identify the boundary between the interior and exterior of an object.

Because the indicator function is a binary function whose value is either 0 or 1, and the iso-value is approximately 0.5, the reconstruction is sufficiently accurate if it never differs by more than 0.5 from the indicator function. As shown in the bottom left reconstruction of Figure 4.11 (and also earlier in Figure 4.10), this relaxed error condition can be met with just one iteration per level of the cascadic multigrid solver, allowing us to perform a single streaming pass at each level. And, one of our key algorithmic contributions is to show that all such passes can be

## CHAPTER 4. STREAMING SURFACE RECONSTRUCTION

combined into a single multilevel streaming pass.

CHAPTER 4. STREAMING SURFACE RECONSTRUCTION

$2^D$	Octree (MB)		Working Set (MB)		Time (h)	
	In-Core	Streaming	In-Core	Streaming	In-Core	Streaming
256	49	48	309	521	0.50	0.53
512	188	168	442	278	0.65	0.68
1024	818	702	1285	213	1.05	1.20
2048	3,695	3,070	4,442	212	2.65	3.33
4096	-	13,367	-	427	-	12.6
8192	-	39,452	-	780	-	32.3

Table 4.3: Comparison of the data structure size (MB), peak working set (MB), and running time (hours) for the in-core and streaming reconstruction algorithms over a range of resolutions for the David Head model. Running the in-core algorithm beyond a resolution of 2048 was impossible due to its high memory requirements.



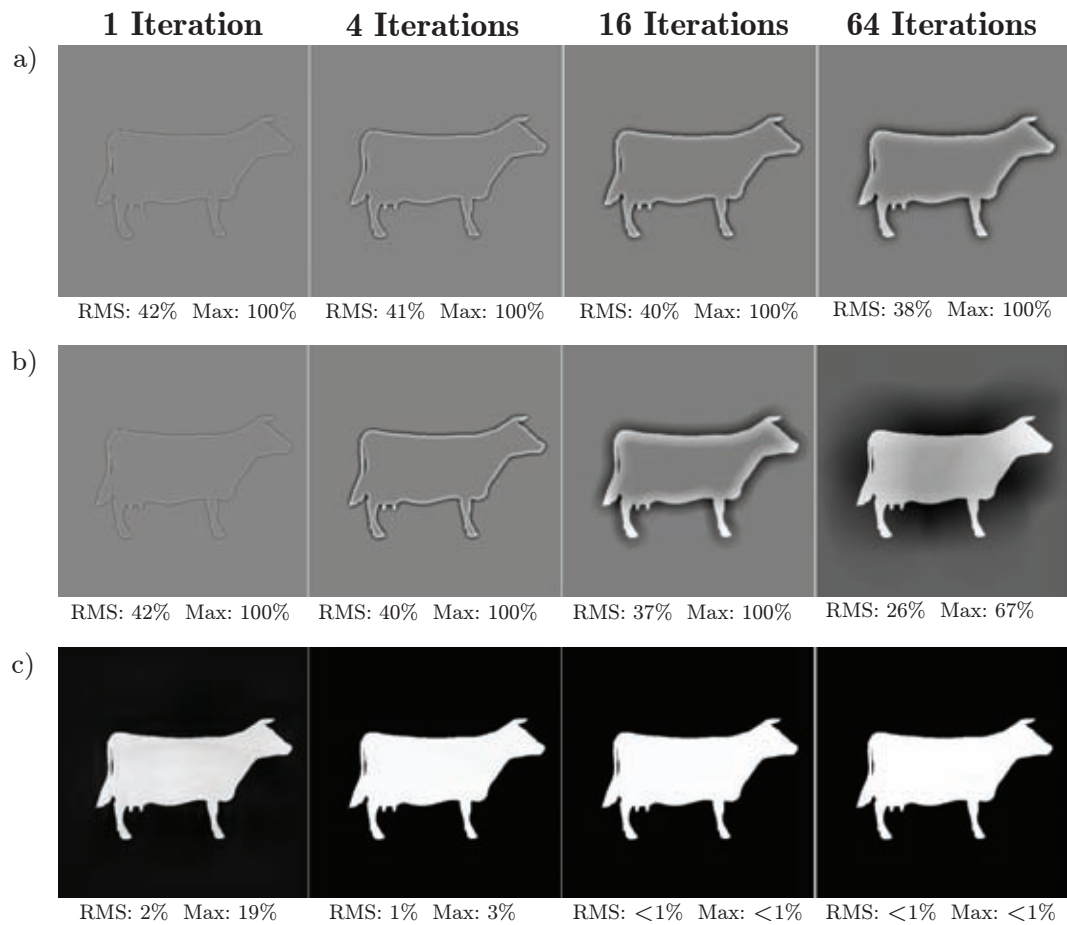


Figure 4.11: Comparison of reconstructing the indicator function of a cow silhouette from its Laplacian using a single-resolution streaming solver (a), a traditional conjugate-gradient solver (b), and a cascadic multigrid solver using multilevel streaming (c).

# Chapter 5

## Parallel Surface Reconstruction

In Chapter 4, we were able to express all the computation steps of the Poisson Surface Reconstruction algorithm as local updates. This locality of data reference permitted the reconstruction to be performed as a set of streaming operations, significantly reducing the main memory required to reconstruct extremely large datasets: the reconstruction of Michelangelo's *Awakening* from 391 million data points only required 2120 megabytes of working memory. Although the streaming technique makes it possible to reconstruct large models on a commodity computer, the processing time is still significant: the reconstruction of *Awakening* required 82 hours of processor time. As datasets increase in size, the processing time could grow to weeks or months.

To address these practical limitations, we take advantage of the recent trend in microprocessor evolution toward parallelism. Multi-core processors are

## CHAPTER 5. PARALLEL SURFACE RECONSTRUCTION

now commonplace among commodity computers, and highly parallel graphics hardware provides even higher performance per watt. Traditional single-threaded algorithms will no longer benefit from Moore's law, introducing a new age in computer science in which efficient parallel implementations are required.

This chapter presents an efficient, scalable, parallel implementation of the Poisson Surface Reconstruction algorithm. The system is designed to run on modern parallel computer systems, allowing the reconstruction of some of the largest available datasets in significantly less time than previously possible. We begin by describing a parallel implementation designed for multi-core systems with shared memory (i.e. processors sharing a common main memory). We show that, although simple to implement and effective on dual-core processors, this model ultimately lacks the scalability required for large problems. Analyzing the shared-memory implementation provides valuable insight regarding the key properties a parallel solver must satisfy to demonstrate good speed-up when parallelized across numerous processors. We then describe a design based on a distributed memory model. The elimination of frequent data sharing and synchronization allows the distributed system to scale to twelve processors across multiple machines.

## 5.1 Related Work

Despite the increasing presence of commodity parallel computing systems, there has been comparatively little work on parallel surface reconstruction. Some surface reconstruction algorithms naturally lend themselves to efficient parallel implementations.

Many local implicit function fitting methods can be at least partially parallelized by virtue of the locality of most data dependencies. For example, the VRIP [17] method can partition the voxel grid across a number of processors. With an appropriate padding region, all data dependencies become local and each processor is able to independently construct the distance function and extract the triangles for a portion of surface. Surface patches can then be zippered together to form a complete model.

Global implicit function fitting methods often have complex data dependencies that inhibit parallelism. One notable exception to this is the FFT method [31], which can be efficiently computed in parallel by virtue of extensive use of Fast Fourier Transforms, which have well known parallel implementations on a variety of platforms [1, 40].

Computational geometry approaches can leverage parallel processing by computing structures such as the Delaunay triangulation in parallel (e.g. [24]).

The work of [59] implements our Poisson method on the GPU, achieving significant speedups for small datasets. A limitation of the implementation is that

it requires the entire octree, dataset and supplemental lookup tables to reside in GPU memory, limiting the maximum size of reconstructions possible. To simplify the lookup of neighbor nodes in the octree and reduce the total number of node computations required, the implementation also only uses first-order elements.

## 5.2 Parallel Reconstruction

When designing the streaming implementation, one of the primary concerns was minimizing the effect of the I/O required for out-of-core processing. In particular, this motivated the streaming approach (since streaming I/O is highly efficient) and the minimization of the number of passes required through the data (minimizing the total amount of I/O performed). When considering a parallel implementation, a different set of design concerns prevail: minimizing data sharing and synchronization.

## 5.3 Shared Memory

The most straightforward parallelization of the serial streaming implementation executes node kernel functions in parallel. Almost all of the total computation time is spent executing node functions across the octree, and the restrictions placed on node function data dependencies for efficient streaming allow the functions within a slice to be executed in any order. With slices in large

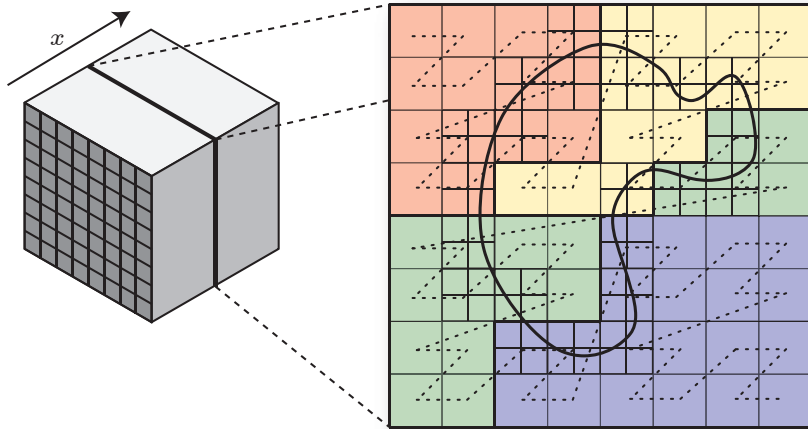


Figure 5.1: An illustration of the way data partitions are formed from the tree using the shared memory approach. Each slice of nodes at each depth in the tree is partitioned into a regular grid. Data partitions contain approximately the same amount of the curve (by length) and are shaded according to which processor they are allocated to. Each allocation forms a contiguous block in Morton (Z-curve) order.

reconstructions typically containing tens- or hundreds of thousands of nodes, there appears to be ample exploitable parallelism.

### 5.3.1 Data Partitioning

To allocate work to each of the processors, a data decomposition approach is used: each processing slice in the octree is partitioned into a coarse  $m \times m$  grid. The data partition  $\mathcal{O}_{i,j}^{s,d}$  contains all nodes  $o \in \mathcal{O}$  from a given slice ( $o.d = d, o.x = s$ ) and partition within a slice  $i \leq 2^{-m} \times o.y < i + 1$  and  $j \leq 2^{-m} \times o.z < j + 1$ .

Figure 5.1 summarizes the decomposition of an octree slice into partitions. Since the data dependencies of a node function are compact, the only shared data

between partitions within the same level of the tree resides around the perimeter of each partition.

### 5.3.2 Work Distribution

To maximize the scalability of the algorithm, we have three main objectives when allocating data partitions to processors:

- **Minimize Skew:** The work across all processors should be as evenly balanced as possible. This ensures that processors are not left unnecessarily idle whilst waiting for work on other processors to complete.
- **Minimize Sharing:** The number of boundaries between data partitions that are assigned to different processors should be minimized. Data sharing and synchronization needs to be performed whenever two spatially adjacent partitions are processed on different processors. The cost of data sharing is minimized when the number of shared boundaries are minimized.
- **Maximize Reuse:** The assignment of a data partition to a processor should be consistent from one slice to the next. Attempting to maintain the locality of a processor's working set can have caching benefits from the reuse of data.

The allocation of data partitions to processors is performed dynamically at runtime. To minimize skew, each processor should have approximately the

## CHAPTER 5. PARALLEL SURFACE RECONSTRUCTION

same amount of work to perform per slice. One of the challenges in balancing the workload is due to the way in which the octree is partitioned. Although the decomposition of the octree space is regular, the distribution of the octree nodes within the tree is not (since the tree is adaptive). This means that the simple approach of allocating one data partition to one processor will lead to a highly skewed and inefficient workload. To avoid this problem, we use a “virtual processors” approach: we create many more data partitions than processors and assign a variable number of partitions to each processor, trying to best balance the workload. The granularity at which the octree is partitioned is a performance trade-off: a finer decomposition can more evenly balance the workload at the cost of increasing the amount of shared data as a proportion of the total data. In practice, we found that a decomposition with at least 16 times the number of partitions as processors provides the best trade off.

To minimize data sharing and maximize the potential for data reuse, we place constraints upon the processor to which a given data partition can be assigned. First, we sort the data partitions using a Morton-order space filling curve (Z-curve) [41]. Then, we allocate data partitions such that each processor is given a block of data partitions that are consecutive in Morton-order. This ordering, illustrated in Figure 5.1, tends to preserve spatial locality for each processor and reduce the number of partition boundaries shared across processors. Additionally, since there is typically coherence in the distribution of octree nodes from one slice



to the next, this allocation technique also preserves coherence across slices, offering the potential for data reuse.

### 5.3.3 Data Sharing

The most challenging aspects of parallelizing the execution of node kernel functions is managing the concurrent update of data. Because our algorithm is based around a *global* solution to the reconstruction problem, there is no way to decompose the problem space into a set of smaller, completely separable problems that can be trivially merged back together to reach the same solution.

The majority of the updates performed by node functions are an accumulations of the form:  $o.x \leftarrow o.x + v$  where  $o \in \mathcal{O}$  is some node in the tree,  $x$  is a data element of  $o$  (for example, a weight function coefficient) and  $v$  is a scalar value; or  $\mathcal{G}.x \leftarrow \mathcal{G}.x + v$  where  $\mathcal{G}.x$  is a global accumulator (such as the iso-value). The parallel evaluation of *accumulative* kernels is straightforward, since only a single processor updates  $o.x$ , and all shared data are read-only. During the execution of *distributive* kernels, however, a node  $o$  near the boundary of partitions, or a global value  $\mathcal{G}.x$ , can be concurrently updated – along the edges of partitions, updates from two processors are possible; in the corners of partitions, updates from four processors are possible. Similarly, global values may receive updates from all processors. To ensure the correctness of the result of the computation, access to the shared data must be controlled to ensure that updates from all processors

## CHAPTER 5. PARALLEL SURFACE RECONSTRUCTION

are reflected in the final result. Three different techniques can be used to protect these updates.

Global update concurrency can be eliminated by virtue of the fact that the accumulation is a linear operator: each processor can maintain a private copy of a global value, and all private copies can be merged once at the end of the computation pass. Care must be taken to avoid placing the private copies too near each other in memory: the hidden cost of false sharing of cache lines may occur if two processors update two independent memory locations that fall in the same cache line.

Updates to node data cannot be handled in the same manner as global data due to the high storage cost of maintaining multiple copies of all node data. Instead, we tried two different strategies for managing concurrency.

The first approach is to use a traditional mutual exclusion locking scheme. When a processor needs to update a value  $o.x$ , it first acquires a lock, performs the necessary update, and then releases the lock: only one processor holds the lock at any one time, so no conflicting updates can occur. Because only updates that occur near shared partition boundaries can potentially conflict with other processors, we use a spatially based locking scheme to increase the possible level of concurrency: locking is performed on the granularity of data partitions. The update of a node  $o$  is protected by a lock corresponding to the data partition the node resides in. This scheme has the advantage that it allows values in data partitions that are

## CHAPTER 5. PARALLEL SURFACE RECONSTRUCTION

spatially separate from each other to be updated without interference. A further optimization can be made for data partitions that are “interior” to a processor’s work block: if a data partition does not share an edge or corner with a data partition assigned to another processor, then no locking need occur since it is not possible for another processor to need to update its values.

The second approach is to utilize the atomic compare and swap (CAS) instruction found in many modern microprocessor architectures. Given a memory address  $A$ , a comparison value  $c$  and a replacement value  $x$ , the processor then performs the update  $A \leftarrow x$  if and only if  $A = c$ , atomically (i.e. the comparison and the assignment are performed as a single, uninterruptable sequence). This instruction can be used to construct a lightweight, optimistic, floating-point atomic accumulation function that can be used in our algorithm. The algorithm is presented in Algorithm 5.1. The method works by recording the existing value of  $c \leftarrow A$  and optimistically updating  $A' \leftarrow c + x$ . The CAS primitive is then used to atomically test the current value of  $A$  and then attempt to update  $A \leftarrow A'$  if the value of  $A$  is unchanged (i.e. no other update has occurred from another processor). If the CAS operation fails, the procedure is repeated. The number of update attempts will be proportional to the level of contention on the shared data. Although this technique is vulnerable to the so-called “ABA” problem, such a situation does not affect the correctness in our situation.

We implemented both of these approaches and present the results in Section 5.3.4.

---

**Algorithm 5.1** The lock-free accumulate operation for floating-point numbers
 

---

```

repeat
   $c \leftarrow A$ 
   $A' \leftarrow c + x$ 
until  $CAS(A, c, A') \neq c$ 

```

---

In addition to the most common case of accumulating data in tree nodes or global variables, there are two other types of concurrent updates in our method that are worthy of further detail.

### 5.3.3.1 Tree Construction

In Section 4.3.2, we described the way in which tree nodes are created in an in-core octree before the nodes are written to the out-of-core node streams. When implementing this in a parallel setting, we partition the point set using the same data partitioning scheme that is used for node data: for each slice of points, we partition the slice into an  $m \times m$  grid and partition the points according to the block they fall into. Using this scheme, we can construct the in-core tree in parallel by simultaneously constructing independent branches of the in-core tree on different processors. One complication, however, is that to facilitate the splatting of a point into the tree to create the approximation to the gradient of the indicator function, we require the one-ring neighborhood of nodes around any node which contains a point sample to exist in the tree. When points fall near a partition boundary, this refinement step requires nodes to be created that fall into a branch of the tree being constructed simultaneously on another processor.

## CHAPTER 5. PARALLEL SURFACE RECONSTRUCTION

To prevent race conditions during the allocation and attachment of nodes to the tree, we again use the atomic compare and swap instruction. The steps to create a new tree node are presented in Algorithm 5.2. The technique uses the compare and swap operation to set the child pointer of a tree node to a newly initialized brood of nodes only if the child pointer is null.

---

**Algorithm 5.2** The lock-free atomic operation for creating in-core tree nodes

---

```
if n.children = 0 then  
     $n' \leftarrow \text{CreateNode}$   
     $n.children = \text{CAS}(n.children, 0, n')$   
    if  $n.children \neq n'$  then  
         $\text{DeleteNode}(n')$   
    end if  
end if
```

---

### 5.3.3.2 Solving the Laplacian

Although the process of solving the linear system can be performed using our concurrent update scheme from Section 5.3.3, we leverage some unique properties of the solver to eliminate the need to perform synchronization and locking. In the streaming implementation from Chapter 4, to solve the Laplacian at a given slice and depth we construct a single linear system  $L\vec{x} = \vec{b}$  and solve for  $\vec{x}$ , the vector of solution coefficients, using several iterations of Gauss-Siedel updates.

To solve this same problem in parallel, we construct separate linear systems per processor and solve them *independently*. Each processor solves for (i.e. updates) the portion of  $\vec{x}$  whose nodes fall within its data partitions. To ensure that

the solution propagates correctly across data partition boundaries, all processors share a common  $\vec{x}$  so that updates to solution values during solver iterations are immediately visible to other processors. Note that although this causes unsynchronized access to shared data, there are two characteristics of our Gauss-Seidel solver that ensure the accuracy of the solution is maintained. First, the write of a single solution value (i.e. a single 32-bit word of memory) is an atomic operation: when other processors read the value, they will either see an old value, or a new value, not a combination of the two. Second, the solver we are using is resilient to reading older solution values, mixed with newer values. While this could lead to a situation in which the subsequent relaxations of previously relaxed coefficients near the partition boundary read un-relaxed values from their neighbors, we have found that in practice this is not a problem.

### 5.3.4 Scalability Issues

Figure 5.2 presents the scalability of the shared memory implementation, reconstructing the Lucy model at depth 12 from one to eight cores. The processor cores were arranged in a 2x2x2 configuration: 2 cores per die, 2 dies per package, with 2 sockets in the machine. Each core has a private 32KB L1 data cache and each die shares a 6MB L2 data cache. Although the shared memory approach provides a straightforward implementation, in practice it was found to have two significant scalability issues.

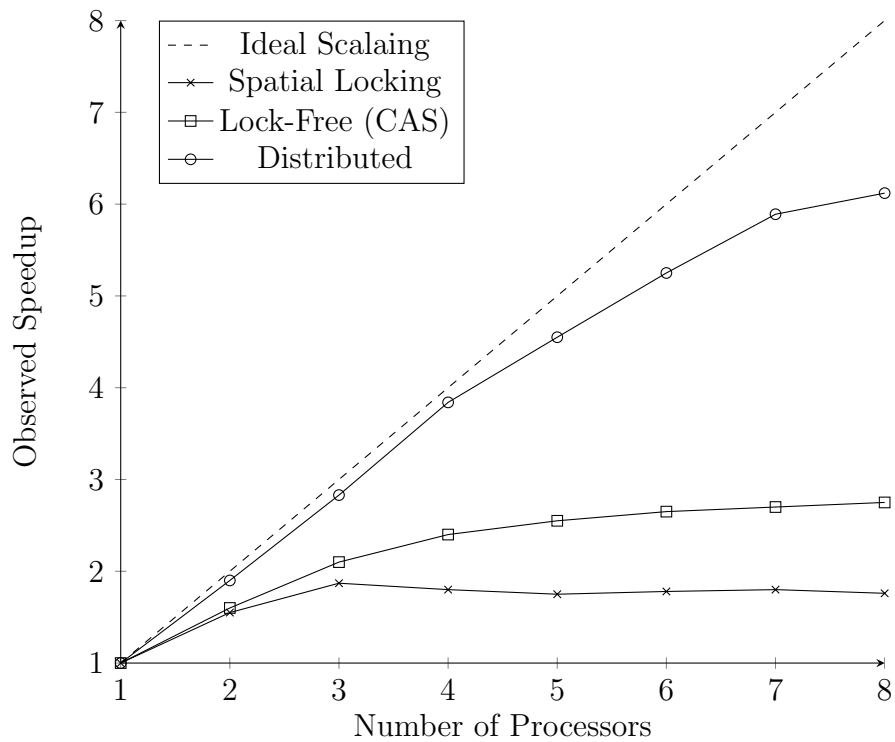


Figure 5.2: The speedup of the shared memory parallel approach for the “Lucy” dataset at depth 12 running on one through eight processors. The spatial locking and lock-free methods are compared. The distributed method from section 5.4 is included for later comparison.

## CHAPTER 5. PARALLEL SURFACE RECONSTRUCTION

First, for distributive functions, data are shared not only within a level of the tree, but across all depths of the tree. At the finest levels, the contention for shared data is very low: since a very small portion of each partition is shared, the probability of two processors needing concurrent access to a datum are low. At the coarser levels of the tree, however, the rate of contention becomes very high and the data associated with the coarsest levels of the tree are updated by each processor for every computation. Although particularly noticeable when using a spatial locking scheme, we found that this problem persisted even when we used an optimistic, lock-free technique that implemented an atomic floating-point accumulation.

Second, scalability is limited by the large number of global synchronization barriers that are required to evaluate multiple functions correctly. Each streaming pass,  $P$ , across the octree is a pipeline of functions  $P = \{N_1, N_2, \dots, N_n\}$  that are executed in sequence. Although the data dependencies are such that the evaluation of  $N_i(o)$  cannot depend on the result of  $N_i(o')$ , it is possible that  $N_i$  may depend on  $N_j$  if  $i > j$ . The implication of this in a parallel setting is that function  $N_i$  cannot be evaluated for a particular slice until  $N_j$  has completed processing in dependent slices *on all processors*, requiring a global synchronization barrier to be introduced between *each function*, for *each processing slice*. For all but the very largest reconstructions, the overhead of this is prohibitive. Although this synchronization frequency can be reduced by processing functions over slabs



of data formed from multiple octree slices, the associated increase in in-core memory usage results in an undesirable practical limitation on the reconstruction resolution.

## 5.4 Distributed Memory

To address the scalability issues that arise from using a shared memory, multi-threaded, architecture we re-evaluated the initial design and opted instead to use a distributed memory model. In this approach, each processor shares data explicitly through message passing, rather than implicitly through shared memory. The advantages of this model over the shared memory approach are as follows:

- **Explicit data sharing:** One of the major limitations of the shared memory approach was that data was frequently, and implicitly shared. In the distributed approach, each processor maintains a private copy of all data it needs. Thus, data writes during computation can be performed without the need for synchronization, and data modified on more than one processor can be easily and efficiently reconciled at the end of each computation pass.
- **Scalable I/O and Memory Bandwidth:** Without the need for shared memory space, the system can be run on computing clusters, offering the potential for greater scalability, due to the increased memory and I/O bandwidth, and number of processors.

To implement our distributed model, we revert to the simple streaming implementation from Section 4.3 in which each function is implemented as a separate streaming pass through the data. While this increases the amount of I/O performed, it alleviates the need for global, inter-slice, synchronization barriers that are required to allow multiple functions to be evaluated correctly.

### 5.4.1 Data Partitioning

Instead of fine-grained, slice-level parallelism, the distributed system uses a coarse-grained approach: the reconstruction domain is partitioned into  $p$  slabs (where  $p$  is the number of processors) along the x-axis given by the x-coordinates  $X = \{x_0, x_1, x_2, \dots, x_p\}$ . The nodes from depth  $d$  in the octree are split into partitions  $\mathcal{O}^d = \{\mathcal{O}_1^d, \mathcal{O}_2^d, \dots, \mathcal{O}_p^d\}$  where  $\mathcal{O}_p^d$  are all nodes  $o \in \mathcal{O}$  such that  $x_p \leq o.x < x_{p+1}$  and  $o.d = d$ .

Since the coarse nodes in the tree are frequently shared across all processors, we designate the first  $d_{full}$  levels in the tree to be part of its own data partition  $\mathcal{O}^{full}$ , which is not owned by a particular process, and whose processing is carried out in duplicate by all processors. Since the total data size of  $\mathcal{O}^{full}$  is small, the added expense of duplicating this computation is significantly smaller than the cost of managing consistent replication of the data.

Figure 5.3 summarizes the decomposition of the octree into partitions. A processor  $P_i$  is assigned to own and process the nodes in  $\mathcal{O}_i^*$  in a streaming manner.

CHAPTER 5. PARALLEL SURFACE RECONSTRUCTION

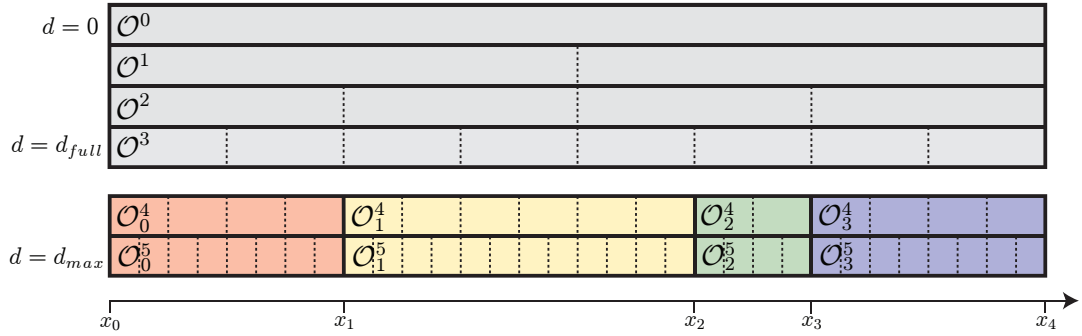


Figure 5.3: An illustration of the way data partitions are formed from the tree with  $p = 4$  processors. All nodes in  $\mathcal{O}^0$ ,  $\mathcal{O}^1$  and  $\mathcal{O}^2$  are shared among all processors and form the data partition  $\mathcal{O}^{full}$ . The nodes in remaining depths are split into spatial regions defined by the x-coordinates  $\{x_0, x_1, x_2, x_3, x_4\}$  forming the partitions  $\mathcal{O}_i^d$ . Note that the finer level partitions do not have to be equal in size, but do need to be allocated on the granularity of the width of nodes at depth  $d = d_{full}$ .

To allow for data sharing across slabs, processor  $i$  has a copy of (some of the) data in partitions  $\mathcal{O}_{i-1}^*$  and  $\mathcal{O}_{i+1}^*$  from the result of the previous pass through the data, as well its own copy of  $\mathcal{O}^{full}$ .

Since each function is implemented in a separate streaming pass, the execution of a function  $N_i$  in one data partition can no longer depend on the execution of a function  $N_j$  in another partition, and a global synchronization is only required between the different streaming passes. In practice, we have found that the arithmetic density of most functions means the I/O bandwidth required to perform a streaming pass is more than an order of magnitude smaller than the bandwidth that modern disk drives can deliver, so processing only a single function per pass does not noticeably affect performance.

## 5.4.2 Load Balancing

Because the octree is an adaptive structure, its nodes are non-uniformly distributed over space. This presents a challenge when choosing the partition bounds  $X$  in order to most optimally allocate work across all processors. To minimize workload skew, each partition  $\mathcal{O}_i^d$  should be approximately the same size (assuming that the processing time of each node is, on average, constant).

Because we wish to perform the allocation of nodes to partitions before the tree has been created, we use the input point-set to estimate the density of nodes in the tree. Since an octree node may not straddle two data partitions, the partition bounds  $X$  must be chosen such that each  $x_i$  is a multiple of  $2^{-d_{full}}$  (i.e. the width of the coarsest nodes in the high resolution tree). We use a simple greedy algorithm to allocate  $X$ : given an ideal partition size of  $N_{ideal} = \frac{N}{p}$ , we grow a partition starting at  $x = 0$  until the partition size would exceed  $N_{ideal}$ . We then over-allocate or under-allocate the partition depending on which minimizes  $|N_i - N_{ideal}|$ . The procedure is continued along the x-axis until all partition sizes have been determined.

## 5.4.3 Replication and Merging of Shared Data

Once data have been modified by a processor, the changes need to be reconciled and replicated between processors. As discussed previously, the majority of the

## CHAPTER 5. PARALLEL SURFACE RECONSTRUCTION

shared updates performed by the reconstructor are of the form  $o.v = o.v + v$ ; that is, accumulating some floating-point scalar or vector quantity into tree nodes. The merge process for a process  $P_i$  is as follows:

1. If  $P_i$  has written to  $\mathcal{O}_{i-1}$  and  $\mathcal{O}_{i+1}$ , send data to  $P_{i-1}$  and  $P_{i+1}$  respectively.
2. If  $P_{i-1}$  and  $P_{i+1}$  have modified data in  $\mathcal{O}_i$ , wait for all data to be received.
3. Merge the received data blocks with the data in  $\mathcal{O}_i$  (an efficient vector addition operation).

Once data has been reconciled, the updated data can then be redistributed to other processes as follows:

1. If  $\mathcal{O}_i$  has been updated and is needed by  $P_{i-1}$  or  $P_{i+1}$  in the next pass, send  $\mathcal{O}_i$  to the neighboring processors.
2. If  $\mathcal{O}_{i-1}$  and  $\mathcal{O}_{i+1}$  have modified data needed for the next pass, wait for all updated data blocks.

In practice, there are a number of optimizations that are made to the merge process. First, because the streams underlying the data partitions are managed in memory as blocks for disk streaming purposes, only modified blocks need be sent between processors, not the entire data partition. In fact, only a very small portion of data in  $\mathcal{O}_{i-1}$  and  $\mathcal{O}_{i+1}$  are ever read from or written to  $P_i$  (only the data in slices immediately adjacent to  $\mathcal{O}_i$ ), so the neighboring data streams are

sparsely populated during replication. Second, because each processor streams through the data partitions, changes made to data can be sent asynchronously to other processing nodes as each block in the stream is finalized, rather than after the pass is complete, hiding the latency involved in many message passing operations.

As in the shared-memory model, the tree construction and the solution of the Laplacian cannot be merged and replicated as efficiently.

#### 5.4.4 Tree Construction

To maximize the parallel processing capability of our system, the construction of the octree itself is performed in parallel. The input point-set  $P$  is partitioned during pre-processing into segments  $\mathcal{P} = \{\mathcal{P}_1, \dots, \mathcal{P}_p\}$  where  $\mathcal{P}_i$  contains all points  $x_i \leq p.x < x_{i+1}$  (where  $x_i$  is the partitioning bounds separating the domain of process  $P_{i-1}$  from process  $P_i$ ).

The first challenge presented in the construction of the tree is the different topological structure created in  $\mathcal{O}^{full}$  by each processor. To facilitate the efficient merging of data in later steps, it is desirable to have a consistent coarse resolution tree. Although it is possible to merge each of the coarse resolution trees after the first pass, we take a simpler approach: because the coarse resolution tree is small, we pre-construct it as a fully refined octree of depth  $d_{full} + 1$ .

The second challenge is that in the initial phases of the reconstruction, a point

in partition  $P_i$  may affect the creation of nodes outside of  $\mathcal{O}_i$  (since the normals are splatted into neighboring nodes). Although this problem could be resolved by allowing processors to generate nodes outside their partition and then merging the nodes at the end of the streaming pass, we have opted for a simpler solution. Recognizing that the points that can create nodes and update data in  $\mathcal{O}_i$  are in the bounds  $x_i - \delta_x \leq p.x < x_{i+1} + \delta_x$ , (where  $\delta_x = 2^{-d_{full}}$  is the width of the finest-level nodes in the full octree  $\mathcal{O}^{full}$ ), we have processor  $P_i$  process this extended subset of points and only perform the associated updates of nodes in  $\mathcal{O}_i$ . In practice, this adds a small computational cost by processing overlapping point data partitions, but greatly simplifies the creation of the tree.

### 5.4.5 Solving the Laplacian

To solve the Poisson equation correctly in a parallel setting, we use an approach inspired by domain decomposition methods [49]. In the serial implementation, the linear system is solved in a streaming manner using a block Gauss-Siedel solver (performing Gauss-Siedel relaxations within each block), making a single pass through the data. Although we can still leverage this technique within each data partition, the regions of the linear system that fall near the boundaries need special treatment to ensure that the solution across partitions is consistent and correct. To avoid the need for the solver in  $\mathcal{O}_i$  to depend on a solution being computed in  $\mathcal{O}_{i-1}$ , each processor  $P_i$  solves a linear system that extends beyond the bounds

$p$	Vertex Count	Triangle Count	Max $\delta$	Average $\delta$
1	320,944	641,884	-	-
2	321,309	641,892	0.73	0.09
4	321,286	641,903	0.44	0.06
8	321,330	641,894	0.98	0.12

Table 5.1: A summary of the the size of each output model, and the maximum and average vertex distance from the serial output of several different reconstructions of the Bunny dataset at depth 9 created with the distributed implementation.

of  $\mathcal{O}_i$  by a small region of padding and, once solutions have been computed by all processors, the solution coefficients in overlapping regions are linearly blended together to give a solution which is consistent across partition boundaries.

## 5.5 Results

To evaluate our method, we designed three types of experiments. In the first, we validate the equivalence of our parallel reconstruction algorithm to the serial implementation, and demonstrate that neither correctness nor quality is sacrificed in the process of parallelization. In the second, we examine the effectiveness and costs of our load balancing method. In the third, we evaluate the scalability of our parallel implementation.



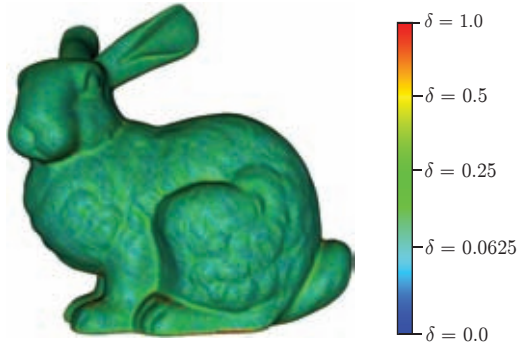


Figure 5.4: The distribution of error across the  $p = 8$  model, when compared to the serial model. The color is used to show  $\delta$  values over the surface with  $\delta = 0.0$  colored blue and  $\delta = 1.0$  colored red. The scale is non-linear to highlight small values of  $\delta$ .

### 5.5.1 Correctness

We wish to ensure that the surface generated by the parallel implementation is equivalent in quality to the serial implementation. In particular, we want to ensure that the model does not significantly change as the number of processors increases, and that any differences that do exist do not accumulate near partition boundaries.

To test this, we ran an experiment using the distributed implementation, reconstructing the Stanford Bunny model at depth 9 using 1, 2, 4, and 8 processors. We then compared the model generated with only one processor  $M_{serial}$ , to the models generated with multiple processors  $M_i$  by computing an error value  $\delta$  at each vertex of  $M_i$  measured as the Euclidean distance to the nearest point on the triangle mesh of  $M_{serial}$ . The units of  $\delta$  are scaled to represent the resolution of the reconstruction so that  $1.0\delta = 2^{-d}$  (the width of the finest

nodes in the tree).

Table 5.1 presents the results of this experiment. Some differences in the output are expected between different numbers of processors because of the lack of commutativity of floating-point arithmetic. The results show that, in all cases, the average error is low and the maximum error is bounded within the size of the finest tree nodes. They also show that error does not significantly change as the number of processors increases. The image in Figure 5.4 shows the distribution of error across the mesh for  $p = 8$ , and is typical of our multiple processor results. The image highlights that error is evenly distributed across the mesh, and that the only significant error occurs along the shape crease along the bottom of the bunny’s back leg. These errors are the result of a different choice in triangulation along the sharper edges of the model (e.g. around the bottom of the Bunny).

### 5.5.2 Skew

To evaluate the efficiency and cost of our load balancing method we ran the algorithm on the head of the David for a range of different values for  $d_{full}$ , and different numbers of processors. The results are presented in Figure 5.5, which plots  $|\max p_i - \frac{\sum p_i}{p}|$  for 2, 4, 8 and 16 processors, where  $p_i$  represents the amount of work allocated to processor  $i$ . From these results, we can make a number of observations.

For this particular dataset, when  $d_{full} \geq 7$ , the workload is very well balanced,

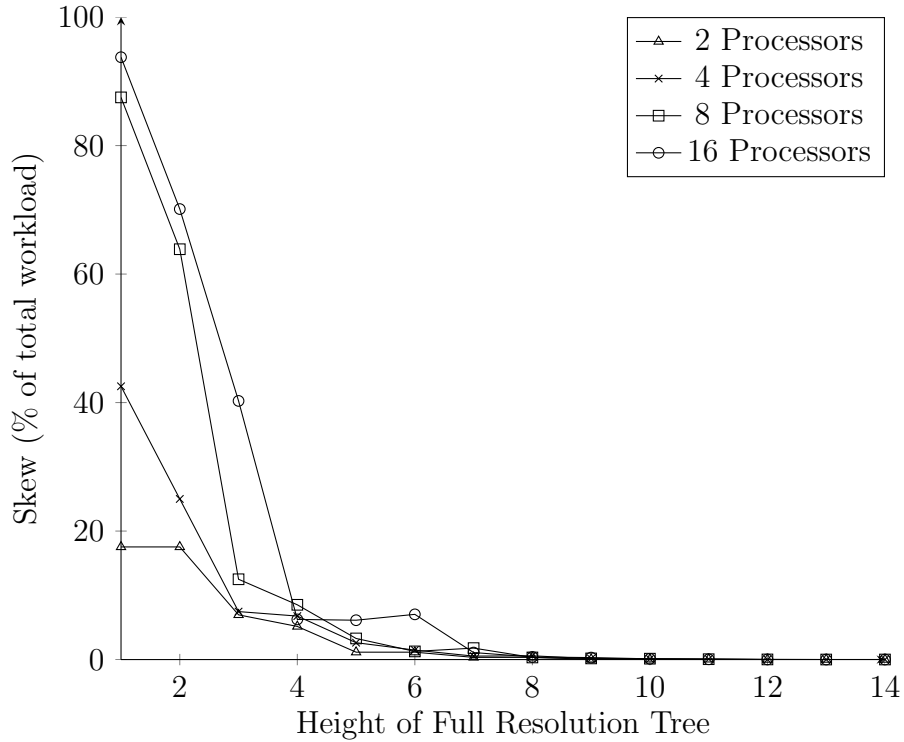


Figure 5.5: The absolute value of the difference between the work allocated to the processor with most work and the average, expressed as a function of the height of the full resolution tree ( $d_{full}$ ) and the number of processors.

even for 16 processors. The total skew in these cases is less than 0.5% of the total workload. In general, as  $d_{full}$  increases, the skew in the allocation of work to processors decreases. This is because as  $d_{full}$  increases, the allocation of work can be performed at finer granularity, offering more opportunity to distribute work evenly.

There is, however, a cost to choosing a larger value for  $d_{full}$ . Table 5.2 presents some performance characteristics of a variety of real-world datasets, with different choices for  $d_{full}$ . Because of the replication of data across processors, the disk use grows as the number of processors increases. A majority of the extra data storage

$p$	Shared Memory			Distributed Memory					
	Lucy		Time	Lucy		David			
Time	Lock	Free		Disk	Memory	Time	Disk	Memory	
1	183	164	149	5,310	163	1,970	78,433	894	
2	118	102	78	5,329	163	985	79,603	888	
4	101	68	38	5,368	164	505	81,947	901	
6	102	61	26	5,406	162	340	84,274	889	
8	103	58	20	5,441	166	259	86,658	903	
10	-	-	18	5,481	163	229	88,997	893	
12	-	-	17	5,522	164	221	91,395	897	

Table 5.2: The running time (in minutes), aggregate disk use (in MB), and peak memory use (in MB) of the shared memory and distributed memory implementations of the Parallel Poisson Surface Reconstruction algorithms for the Lucy dataset at depth 12, with  $d_{full} = 6$  and the David dataset at depth 14 with  $d_{full} = 8$ , running on one through twelve processors. It was not possible to run the shared memory implementation on more than eight processors.

is from  $\mathcal{O}^{full}$ , whose size grows as  $d_{full}$  is increased. For the Lucy model, with  $d_{full} = 6$ , the size of  $\mathcal{O}^{full}$  is only 18MB. For the David model, with  $d_{full} = 8$ , it is 1160MB. The best choice for  $d_{full}$  is a value that minimizes workload skew without unnecessarily increasing the aggregate storage requirements.

### 5.5.3 Scalability

One of the most desirable properties of a parallel algorithm is scalability. Scalability is a direct measure of the ability of the algorithm to run efficiently as the number of processors increases. Table 5.2 shows the running times and Figure 5.6 shows the speedup of the distributed memory implementations on up to 12 processors when reconstructing the Lucy dataset (94 million points), and

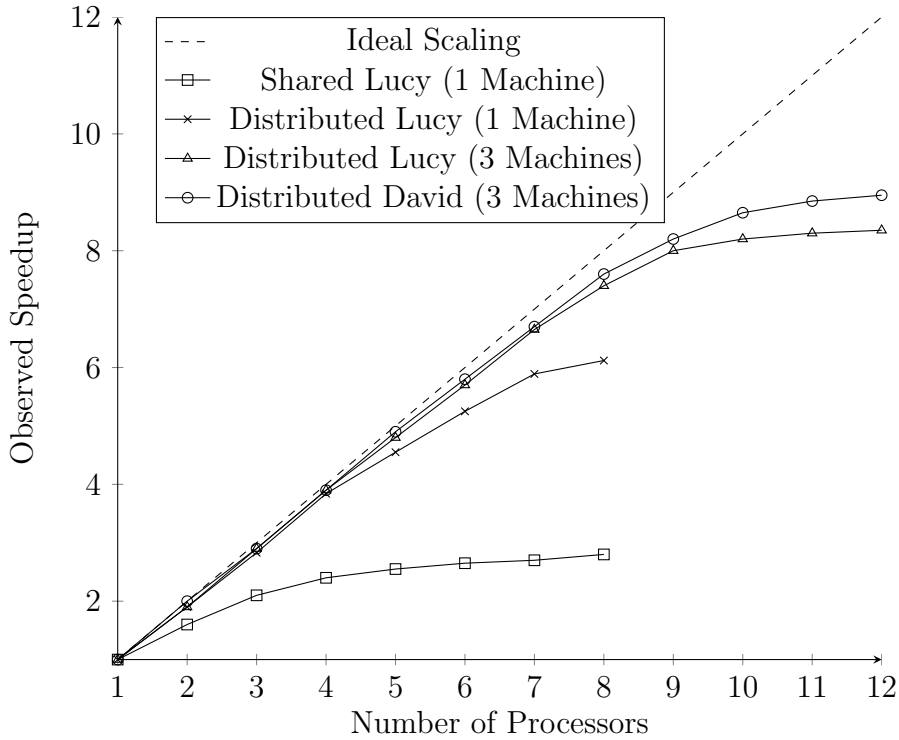


Figure 5.6: The speedup of the distributed implementation for the Lucy dataset at depth 12 and the David dataset at depth 14 running on one through twelve processors. The shared memory approach from Section 5.3 is included for comparative purposes.

the David dataset (1 billion points). The best shared memory implementation from Section 5.3 is included for comparison.

The shared memory implementation was run on a dual quad core workstation where processor cores were arranged in a 2x2x2 configuration: 2 cores per die, 2 dies per package, with 2 sockets in the machine. Each core has a private 32KB L1 data cache and each die shares a 6MB L2 data cache. The distributed memory implementation was run on a three machine cluster with quad core processors and a gigabit Ethernet interconnect. The processor cores in each machine were

## CHAPTER 5. PARALLEL SURFACE RECONSTRUCTION

arranged in a 1x2x2 configuration: 2 cores per die, 2 dies per package, with 1 socket per machine. The cache layout is the same as the shared memory machine.

When we examine the scalability of the shared memory implementation, which uses atomic instructions to manage concurrent updates, we see that the scalability is severely limited compared to the distributed implementation. One significant factor affecting the performance is the way in which shared memory data updates interact with architectural elements of the underlying hardware. When locking shared data between processors, data that were kept primarily in fast on-chip memory caches have to be flushed and shared through main memory each time it is modified to keep separate caches coherent. This forces frequently shared data to be extremely inefficient to access, with no cache to hide high latency memory access. Because the distributed implementation does not need to coordinate writes to the same data, the computation is far more efficient, and cleanly scales with increasing numbers of processors. The reduced scalability as the number of processors increases is due to the complete occupancy of all processors on each machine, causing the algorithm to become memory bandwidth bound.

To highlight the advantages of using *multiple* machines to run the distributed implementation, we also ran the distributed implementation on the shared memory machine. The results of this experiment are shown in Figure 5.6 on the data series labelled “Distributed Lucy (1 machine)”. Although the distributed implementation performs significantly better than the shared memory

implementation on the same hardware, the scalability is still limited when compared to running the distributed method on multiple machines. This is because the multiple machine configuration offers far greater total disk and memory bandwidth. When running our algorithm on all 8 processors of a single machine, some passes through the data streams become I/O bound, and the main memory bandwidth is insufficient to supply the data necessary to perform compute bound tasks concurrently.

Table 5.2 also lists the peak in-core memory use and aggregate disk use of the distributed algorithm. Since the in-core memory use is related to the size of the largest slices and each data partition is streamed independently, peak memory use is consistent across all degrees of parallelism.

### 5.5.4 David

As a final example of the ability of our method to accurately and efficiently reconstruct the largest datasets available, we reconstructed Michelangelo’s *David* from 1,034 million points using a maximum tree depth of 15. Figure 5.7 shows the reconstructed model, which consists of 1,031 million triangles. The close-up views of David’s foot (a) and hand (b) emphasize the fine details present. On 12 processors, the reconstruction took 886 minutes and required a maximum of 2,067 MB of main memory. The octree was partitioned with  $d_{full} = 8$  and required 242 GB of total storage across all nodes. Across all passes of the reconstruction, a

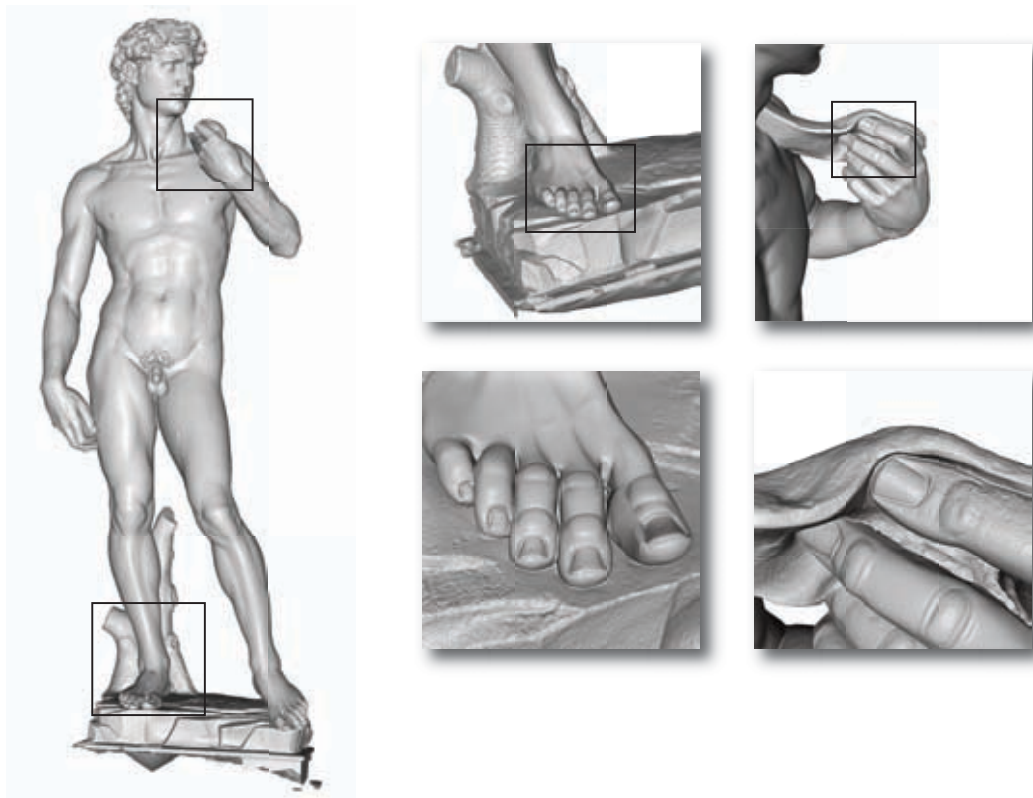


Figure 5.7: A reconstruction of the David model at depth 15.



## CHAPTER 5. PARALLEL SURFACE RECONSTRUCTION

total of 2,178 GB of disk I/O was performed. Of the 28 GB of total network I/O, 51 MB was performed synchronously at the end of the data passes.

# Chapter 6

## Conclusion

In this dissertation we have described a new technique for surface reconstruction that is designed to meet the demands of modern reconstruction datasets.

In Chapter 3, we described the *Poisson Surface Reconstruction* technique which takes a global implicit function fitting approach to solving the surface reconstruction problem by constructing an approximation to the indicator function ( $\chi$ ) of the unknown surface. Using an oriented pointset, we construct an approximation to the gradient of the indicator function ( $\vec{V} \approx \nabla\chi$ ), compute the divergence ( $\nabla \cdot \nabla\chi$ ) and solve the Poisson problem  $\nabla^2\chi = \nabla \cdot \vec{V}$  for the unknown  $\chi$ . The reconstructed surface is then extracted as a level-set of  $\chi$ .

We exploit the fact that the indicator function is constant almost everywhere (and thus, the gradient is zero almost everywhere), and represent both the

## CHAPTER 6. CONCLUSION

indicator function and its gradient within an adaptive, hierarchical function space defined over an octree. This adaptive representation makes the algorithm output-sensitive and have a spatial complexity of  $O(n^2)$  and temporal complexity of  $O(n^2 \log n)$ .

Because we use a *global* approach to the problem, our method is highly robust to noise and other anomalies found in real-world scan data. Through experiments, we have shown this method to be competitive in terms of running time and often superior in quality to a wide range of existing methods. One of the practical limitations of our method is that the octree-based representation of the indicator function was required to be in main memory at all times. This limited the maximum size of reconstructions we could perform.

In Chapter 4, we addressed the challenge of reconstructing extremely large datasets by introducing a streaming framework to the problem. Using the knowledge that each computation involved in the Poisson reconstruction method only requires a small portion of the octree data at any one time, the octree can be stored on disk and data can be loaded into main memory only when required. To make the transfer of data to and from disk as efficient as possible, we use a *streaming* approach: a given piece of data is read from disk into memory once when it is first needed for a computation and is written back to disk (thus freeing memory) after it is no longer needed for further computation. Because data at different depths of the octree have significantly varying lifetimes, we use a *multi-*

## CHAPTER 6. CONCLUSION

*level* approach to streaming: each level of the tree is managed and streamed independently. This allows the portion of the octree data in memory at any one time to be as small as possible. Through pipelining and the use of a cascadic multigrid solver, the entire reconstruction process is implemented in just three passes across the octree data.

We demonstrated that our streaming approach removes the limitations on memory size by reconstructing several large models including Michelangelo's Awakening from 431 million data points. For this model, the reconstruction created an octree containing 106GB of data, while using only 2.1GB of main memory. Despite needing to stream large amounts of data to and from disk, the running time was only approximately 20 percent slower than the in-core implementation.

Finally, in Chapter 5, we extended the streaming technique to run in parallel on multi-core CPUs and CPU-based computing clusters. We used the knowledge of data dependencies gained from the streaming work to partition the octree data and evaluate a given computation across all nodes in a partition in parallel. Using a distributed memory model, we resolved the need for frequent data synchronization by replicating commonly updated data across all processors and merging results together at the end of a computation pass. We have shown that our distributed implementation is effective when running on a single computer with multi-core CPUs or on a computing cluster. On a multi-core, multi-processor workstation

with 8 cores, we can reconstruct surfaces 6 times faster than the non-parallel approach, and on a 12 processor cluster, we can reconstruct surfaces 9.3 times faster.

## 6.1 Future Work

There are a number of avenues for future work, including extending our parallel method to run on graphics processing units (GPUs) and developing a rigorous way for evaluating and comparing surface reconstruction techniques. We now discuss these ideas in more detail.

### 6.1.1 A GPU Implementation

Modern graphics processing units (GPUs) are among the most powerful processing chips that exist today. State of the art GPUs are capable of over 2.5 teraflops of single precision floating-point arithmetic and have in excess of 250 GB/s of memory bandwidth – orders of magnitude more than current multi-core CPUs. The hardware-based scheduler in a GPU is capable of scheduling tens of thousands of active, lightweight, hardware threads onto hundreds of processing cores. Although originally designed and used specifically as specialized hardware to accelerate the rendering of complex 3D scenes, the GPU has been repositioned as a high performance general purpose co-processor.

## CHAPTER 6. CONCLUSION

The work of Zhou *et. al.* [59] implemented the in-core algorithm that we presented in Chapter 3 on the GPU. This implementation has shown that the Poisson Surface Reconstruction method has sufficient inherent data parallelism to perform well on the GPU, with performance speed-ups sufficient to reconstruct small models in real-time. A significant limitation of their approach, however, is that it relies on the entire dataset and octree residing entirely within GPU memory.

In the future, we would like to explore a GPU implementation that is a hybrid of the shared-memory and distributed memory approaches from Chapter 5. A distributed system is required to run a computation across multiple GPUs (even when they are in the same host) because GPU memory space is private and is not shared with other GPUs or the host systems. For the computations within a single GPU a shared memory approach is more appropriate.

### 6.1.2 A Surface Reconstruction Benchmark

Standardized benchmarks have been used in a variety of disciplines to measure the relative performance and correctness of algorithms, ranging from measuring the performance of numerical algorithms as in the LINPACK linear algebra benchmark [19], to comparing shape-matching [48] and segmentation [14] methods in computer graphics.

Unfortunately, there has been no standard benchmark established for

## CHAPTER 6. CONCLUSION

evaluating reconstruction algorithms. The lack of consistency in testing methodology makes it difficult to make direct comparisons between methods, and synthetic data experiments often fail to capture the subtle characteristics of real scanned data, making the test ineffective in measuring real-world reconstruction ability. Experiments run with real-world data do present a more realistic view, but error is often hard to measure and quantify, since no ground truth surface is available, making direct, objective, comparisons between methods difficult. Part of the challenge is that surface reconstruction is used in numerous applications, each of which have their own unique requirements.

In the future, we would like to develop a benchmark that would consist of a battery of carefully designed experiments that, though synthetically generated, would accurately model *individual* sources of error found in real-world data. For example, one test could model non-uniform data by overlaying a set of artificially generated scans of an object. Because these scans are artificially generated (e.g. via ray tracing), the influence of other aspects of real data, such as noise and misalignment can be excluded. The results of each of these experiments would be measured by a collection of error metrics which would include geometry based methods that measure the distance between surfaces, as well as image based methods which could capture perceptual error by comparing renderings of a ground truth and reconstructed model from different viewpoints under a variety of lighting conditions.

## CHAPTER 6. CONCLUSION

We expect such a benchmark to have two main practical uses: First, it would allow different reconstruction methods to be compared in an objective way while capturing key aspects of what makes surface reconstruction from real data a difficult problem. Second, such a benchmark can be used to drive future development of better surface reconstruction methods by helping identify the limitations of existing techniques.



# Bibliography

- [1] AGARWAL, R. C., GUSTAVSON, F. G., AND ZUBAIR, M. A high performance parallel algorithm for 1-d FFT. In *Proceedings of the 1994 Conference on Supercomputing* (1994), pp. 34–40.
- [2] AHN, M., GUSKOV, I., AND LEE, S. Out-of-core remeshing of large polygonal meshes. In *Proceedings on the Conference on Visualization* (2006), vol. 12, pp. 1221–1228.
- [3] ALEXA, M., BEHR, J., COHEN-OR, D., FLEISHMAN, S., LEVIN, D., AND SILVA, C. T. Point set surfaces. In *IEEE VIS* (2001), pp. 21–28.
- [4] AMENTA, N., CHOI, S., AND KOLLURI, R. Power crust. *Sixth ACM Symposium on Solid Modeling and Applications* (2001), 249–260.
- [5] AMENTA, N., CHOI, S., AND KOLLURI, R. K. The power crust, unions of balls, and the medial axis transform. *Computational Geometry: Theory and Applications 19* (2000), 127–153.

## BIBLIOGRAPHY

- [6] ATTALI, D., COHEN-STEINER, D., AND EDELSBRUNNER, H. Extraction and simplification of iso-surfaces in tandem. In *Symposium on Geometry Processing* (2005).
- [7] BARNARD, S. T., AND FISCHLER, M. A. Computational stereo. *ACM Computing Surveys* 14, 4 (1982), 553–572.
- [8] BERNARDINI, F., MITTLEMAN, J., RUSHMEIER, H., SILVA, C., AND TAUBIN, G. The ball-pivoting algorithm for surface reconstruction. *IEEE Transactions on Visualization and Computer Graphics* 5, 4 (1999), 349–359.
- [9] BERNARDINI, F., RUSHMEIER, H., MARTIN, I. M., MITTLEMAN, J., AND TAUBIN, G. Building a digital model of Michelangelo’s Florentine Pietà. *IEEE Computer Graphics and Applications* 22 (2002), 59–67.
- [10] BLINN, J. F. A generalization of algebraic surface drawing. *ACM Transactions on Graphics* 1, 3 (1982), 235–256.
- [11] BORNEMANN, F., AND KRAUSE, R. Classical and cascadic multigrid – a methodological comparison. In *Proceedings of the 9th International Conference on Domain Decomposition Methods* (1996), pp. 64–71.
- [12] BROWN, B. J., AND RUSINKIEWICZ, S. Global non-rigid alignment of 3D scans. *ACM Transactions on Graphics* 26, 3 (July 2007), 21.

## BIBLIOGRAPHY

- [13] CARR, J. C., BEATSON, R. K., CHERRIE, J. B., MITCHELL, T. J., FRIGHT, W. R., MCCALLUM, B. C., AND EVANS, T. R. Reconstruction and representation of 3d objects with radial basis functions. In *ACM Transactions on Graphics, Proceedings of ACM SIGGRAPH* (2001), pp. 67–76.
- [14] CHEN, X., GOLOVINSKIY, A., AND FUNKHOUSER, T. A Benchmark for 3D Mesh Segmentation. *ACM Transactions on Graphics, Proceedings of ACM SIGGRAPH* 28, 3 (8 2009).
- [15] CHEN, Y., AND MEDIONI, G. Description of complex objects from multiple range images using an inflating balloon model. *Computer Vision Image Understanding* 61, 3 (1995), 325–334.
- [16] CIGNONI, P., MONTANI, C., ROCCHINI, C., AND SCOPIGNO, R. External memory management and simplification of huge meshes. *IEEE Transactions on Visualization and Computer Graphics* 9 (2003).
- [17] CURLESS, B., AND LEVOY, M. A volumetric method for building complex models from range images. In *ACM Transactions on Graphics, Proceedings of ACM SIGGRAPH* (1996), pp. 303–312.
- [18] DEY, T., AND GOSWAMI, S. Provable surface reconstruction from noisy samples. In *Annual Symposium on Computational Geometry* (2004), pp. 330–339.

## BIBLIOGRAPHY

- [19] DONGARRA, J. The LINPACK Benchmark: An explanation. *Proceedings of the 1st International Conference on Supercomputing* (1988), 456–474.
- [20] EDELSBRUNNER, H., AND MÜCKE, E. P. Three-dimensional alpha shapes. *ACM Transactions on Graphics* 13, 1 (1994), 43–72.
- [21] FRANKE, R. Scattered data interpolation: Tests of some methods. *Mathematics of Computation* 38, 157 (1982), 181–200.
- [22] GEORGE, A., AND RASHWAN, H. Auxiliary storage methods for solving finite element systems. *SIAM Journal on Scientific and Statistical Computing* 6 (1985).
- [23] GRINSPUN, E., KRYSL, P., AND SCHRÖDER, P. CHARMS: a simple framework for adaptive simulation. In *ACM Transactions on Graphics, Proceedings of ACM SIGGRAPH* (2002), pp. 281–290.
- [24] HARDWICK, J. C. Implementation and evaluation of an efficient parallel Delaunay triangulation algorithm. In *Proceedings of the 9th Annual ACM Symposium on Parallel Algorithms and Architectures* (1997), pp. 23–25.
- [25] HOPPE, H., DEROSE, T., DUCHAMP, T., McDONALD, J., AND STUETZLE, W. Surface reconstruction from unorganized points. *Computer Graphics* 26 (1992), 71–78.

## BIBLIOGRAPHY

- [26] HORN, B. K. P. *Shape from shading: A method for obtaining the shape of a smooth opaque object from one view*. PhD thesis, Department of Electrical Engineering, Massachusetts Institute of Technology, 1970.
- [27] ISENBURG, M., AND LINDSTROM, P. Streaming meshes. In *Proceedings of the Conference on Visualization* (2005).
- [28] ISENBURG, M., LINDSTROM, P., GUMHOLD, S., AND SHEWCHUK, J. Streaming compression of tetrahedral volume meshes. In *Proceedings of Graphics Interface 2006* (2006).
- [29] ISENBURG, M., LINDSTROM, P., GUMHOLD, S., AND SNOEYINK, J. Large mesh simplification using processing sequences. In *Proceedings of the Conference on Visualization* (2003).
- [30] ISENBURG, M., LIU, Y., SHEWCHUK, J., AND SNOEYINK, J. Streaming computation of Delaunay triangulations. *ACM Transactions on Graphics* 25 (2006).
- [31] KAZHDAN, M. Reconstruction of solid models from oriented point sets. In *Eurographics Symposium on Geometry Processing* (2005), p. 73.
- [32] KAZHDAN, M., KLEIN, A., DALAL, K., AND HOPPE, H. Unconstrained isosurface extraction on arbitrary octrees. In *Eurographics Symposium on Geometry Processing 2007* (2007), pp. 125–133.

## BIBLIOGRAPHY

- [33] LEVIN, D. The approximation power of moving least-squares. *Mathematics of Computation* 67 (1998), 1517–1531.
- [34] LEVOY, M., PULLI, K., CURLESS, B., RUSINKIEWICZ, S., KOLLER, D., PEREIRA, L., GINZTON, M., ANDERSON, S., DAVIS, J., GINSBERG, J., SHADE, J., AND FULK, D. The digital Michelangelo project: 3D scanning of large statues. In *ACM Transactions on Graphics, Proceedings of ACM SIGGRAPH* (July 2000).
- [35] LEVOY, M., AND WHITTED, T. The use of points as a display primitive. Tech. Rep. 22, The University of North Carolina at Chapel Hill, 1985.
- [36] LINDSTROM, P., AND SILVA, C. A memory insensitive technique for large model simplification. In *Proceedings of the Conference on Visualization* (2001).
- [37] LORENSEN, W., AND CLINE, H. Marching cubes: A high resolution 3D surface reconstruction algorithm. *ACM Transactions on Graphics, Proceedings of ACM SIGGRAPH* (1987), 163–169.
- [38] LOSASSO, F., GIBOU, F., AND FEDKIW, R. Simulating water and smoke with an octree data structure. *ACM Transactions on Graphics, Proceedings of ACM SIGGRAPH* 23 (2004), 457–462.

## BIBLIOGRAPHY

- [39] MANSON, J., PETROVA, G., AND SCHAEFER, S. Streaming surface reconstruction using wavelets. *Computer Graphics Forum* 27, 5 (2008), 1411–1420.
- [40] MORELAND, K., AND ANGEL, E. The FFT on a GPU. In *HWWS '03: Proceedings of the ACM SIGGRAPH/EUROGRAPHICS conference on Graphics Hardware* (2003), pp. 112–119.
- [41] MORTON, G. A computer oriented geodetic data base; and a new technique in file sequencing. Tech. rep., IBM, 1966.
- [42] MURAKI, S. Volumetric shape description of range data using “blobby model”. In *ACM Transactions on Graphics, Proceedings of ACM SIGGRAPH* (1991), pp. 227–235.
- [43] OHTAKE, Y., BELYAEV, A., ALEXA, M., TURK, G., AND SEIDEL, H.-P. Multi-level partition of unity implicits. *ACM Transactions on Graphics* 22, 3 (2003), 463–470.
- [44] PAJAROLA, R. Stream-processing points. In *Proceedings of the Conference on Visualization* (2005).
- [45] PARZEN, E. On estimation of a probability density function and mode. *The Annals of Mathematical Statistics* 33 (1962), 1065–1076.

## BIBLIOGRAPHY

- [46] SCHALL, O., BELYAEV, A., AND SEIDEL, H.-P. Error-guided adaptive Fourier-based surface reconstruction. *Computer Aided Design* 39, 5 (2007), 421–426.
- [47] SHEKHAR, R., FAYYAD, E., YAGEL, R., AND CORNHILL, J. Octree-based decimation of marching cubes surfaces. In *IEEE Visualization* (1996), pp. 335–342.
- [48] SHILANE, P., MIN, P., KAZHDAN, M., AND FUNKHOUSER, T. The Princeton Shape Benchmark. In *SMI04: Proceedings of the Shape Modeling International 2004* (2004), pp. 167–178.
- [49] SMITH, B., BJORSTAD, P., AND GROPP, W. *Domain Decomposition: Parallel Multilevel Methods for Elliptic Partial Differential Equations*. Cambridge University Press, 2004.
- [50] SNAVELY, N., SEITZ, S. M., AND SZELISKI, R. Modeling the world from internet photo collections. *International Journal of Computer Vision* 80, 2 (2008), 189–210.
- [51] TAUBIN, G. Estimation of planar curves, surfaces, and nonplanar space curves defined by implicit equations with applications to edge and range image segmentation. *IEEE Transactions Pattern Analysis and Machine Intelligence* 13, 11 (1991), 1115–1138.



## BIBLIOGRAPHY

- [52] TOLEDO, S. A survey of out-of-core algorithms in numerical linear algebra. In *External Memory Algorithms and Visualization*, J. Abello and J. Vitter, Eds. American Mathematical Society Press, 1999.
- [53] VO, H., CALLAHAN, S., LINDSTROM, P., PASCUCCI, V., AND SILVA, C. Streaming simplification of tetrahedral meshes. *IEEE Transactions on Visualization and Computer Graphics* 13 (2007).
- [54] WESTERMANN, R., KOBBELT, L., AND ERTL, T. Real-time exploration of regular volume data by adaptive reconstruction of iso-surfaces. *The Visual Computer* 15 (1999), 100–111.
- [55] WILHELMS, J., AND GELDER, A. V. Octrees for faster isosurface generation. *ACM Transactions on Graphics* 11 (1992), 201–227.
- [56] WU, J., AND KOBBELT, L. A stream algorithm for the decimation of massive meshes. In *Proceedings of the Conference on Graphics Interface* (2003).
- [57] ZHANG, Z. Iterative point matching for registration of free-form curves and surfaces. *International Journal of Computer Vision* 13, 2 (1994), 119–152.
- [58] ZHAO, H.-K., OSHER, S., AND FEDKIW, R. Fast surface reconstruction using the level set method. In *VLSM '01: Proceedings of the IEEE Workshop on Variational and Level Set Methods (VLSM'01)* (Washington, DC, USA, 2001), IEEE Computer Society, p. 194.

## BIBLIOGRAPHY

- [59] ZHOU, K., GONG, M., HUANG, X., AND GUO, B. Highly parallel surface reconstruction. Tech. Rep. 53, Microsoft Research, 2008.

# Vita

Matthew Grant Bolitho was born on July 11, 1982 in Nelson, New Zealand. He earned a Bachelor of Science (B.Sc.) degree from the University of Auckland (Auckland, New Zealand) in 2003 and a Bachelor of Science, Honours degree (B.Sc., Hons) with First-Class Honours in Computer Science from the University of Auckland in 2004. Matthew then earned his Masters of Science in Engineering (M.S.E.) from the Johns Hopkins University (Baltimore, Maryland) in 2007 before entering Ph.D. candidacy. His research interests include parallel computing and the construction, processing, and visualization of large geometric datasets.